

**Bangor University**

**DOCTOR OF PHILOSOPHY**

**Optical Effects on the Dynamical Properties of Semiconductor Laser Devices and Their Applications**

Ji, Songkun

*Award date:*  
2019

*Awarding institution:*  
Bangor University

[Link to publication](#)

#### **General rights**

Copyright and moral rights for the publications made accessible in the public portal are retained by the authors and/or other copyright owners and it is a condition of accessing publications that users recognise and abide by the legal requirements associated with these rights.

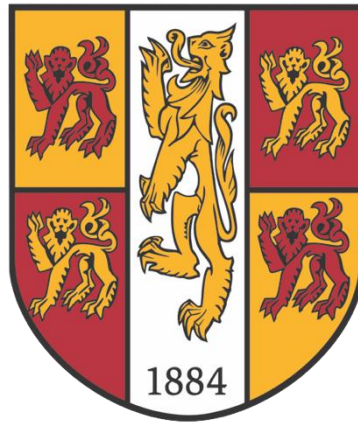
- Users may download and print one copy of any publication from the public portal for the purpose of private study or research.
- You may not further distribute the material or use it for any profit-making activity or commercial gain
- You may freely distribute the URL identifying the publication in the public portal ?

#### **Take down policy**

If you believe that this document breaches copyright please contact us providing details, and we will remove access to the work immediately and investigate your claim.

Download date: 13. Mar. 2024

# **Optical Effects on the Dynamical Properties of Semiconductor Laser Devices and Their Applications**



**Songkun Ji**

**School of Computer Science and Electronic Engineering**

**Bangor University**

**This dissertation is submitted for the degree of Doctor of  
Philosophy**

**February 2019**



## Declaration

I hereby declare that this thesis is the results of my own investigations, except where otherwise stated. All other sources are acknowledged by bibliographic references. This work has not previously been accepted in substance for any degree and is not being concurrently submitted in candidature for any degree unless, as agreed by the University, for approved dual awards.

Songkun Ji

---

----- Yr wyf drwy hyn yn datgan mai canlyniad fy ymchwil fy hun yw'r thesis hwn, ac eithrio lle nodir yn wahanol. Caiff ffynonellau eraill eu cydnabod gan droednodiadau yn rhoi cyfeiriadau eglur. Nid yw sylwedd y gwaith hwn wedi cael ei dderbyn o'r blaen ar gyfer unrhyw radd, ac nid yw'n cael ei gyflwyno ar yr un pryd mewn ymgeisiaeth am unrhyw radd oni bai ei fod, fel y cytunwyd gan y Brifysgol, am gymwysterau deuol cymeradwy.

## Acknowledgements

The completion of this thesis would not be possible without the support of the support I received from many people through my academical and personal life.

I am foremost thankful to my supervisor, Dr. Yanhua Hong, whose enthusiastic and patience help. Her insightful knowledgeable guidance inspired me to overcome the challenges through out my dissertation and the entire course of this study. As being my personal tutor, I would also like to express my gratitude to Dr. Yanhua Hong for her warm care, helping me through my foreign study life.

My deepest gratitude goes to Prof. Jianming Tang, not only he accepted to be my viva internal examiner, but also being one of my mentors, giving many priceless professional advices through my entire PhD study.

I would to thank Prof. K Alan Shore Prof. Paul Spencer, Dr. Zengbo Wang, Dr. Roger Giddings, Dr. Paul Sayers for the development on my professional skills.

I would also like to thank Dr. Iestyn Pierce, Mr. David Edward Jones, Mrs Anwen Williams, Mrs Wendy Halstead for helping me with the administrative matters of my study.

My gratitude also goes to my groupmate, Mr. Chenpeng Xue for his helpful discussions and contributions. I would also like to thank all my other friends and colleagues at the School of Electronic Engineering for making my graduate study and experience memorable.

I am truly grateful and indebted to my parents and family for their endless love and support.

## Abstract

Nonlinear dynamical properties of semiconductor lasers have attracted considerable attention, and their rich behaviors enable many popular research topics. The research effort of this thesis has emphasized on two areas - one is photonic microwave generation based on period one dynamic of semiconductor lasers; the other is laser's chaotic dynamic.

Microwave photonics has attracted considerable attention recently because of its practical applications in radio-over-fiber (RoF) communications links. A stable photonic microwave allows it to convey, in a cost-effective manner, wideband signals over optical fibers with low loss, large bandwidth and immunity of electromagnetic interference. Microwave photonics technologies consist of photonic microwave generation, processing, control and distribution. Many photonic microwave generation techniques have been proposed, which includes direct modulation, optical heterodyne technique, external modulation, mode-locked semiconductor lasers, optoelectronic oscillator (OEO) and period one (P1) dynamic of semiconductor lasers. Among these techniques, photonic microwave generation based on P1 oscillation dynamic has gained special attention due to its many advantages, such as: widely tunable oscillation frequency, and nearly single sideband (SSB) spectrum. The aim of this thesis in the photonic microwave generation area is to produce photonic microwaves based on P1 dynamic using low-cost vertical-cavity surface-emitting lasers (VCSELs). The technical contents in this area cover two parts.

The first part is to generate broadly tunable photonic microwaves. Continuous tuning of the microwave frequency from 4GHz to up to an instrumentation limited 15GHz is experimental achieved through the adjustment of the injection power and the frequency detuning between the master laser and the VCSEL. Numerical simulations using a common spin flip model are also carried out, which agree qualitatively with the experimental results.

The second part of the photonic microwave generation in this thesis is to explore effective approaches to not only reduce the linewidth but also improve the stability of the generated microwave. Due to spontaneous emission noise in the semiconductor laser, P1 dynamic inherently imposes phase noise, which increases the microwave linewidth of the generated microwave. This considerably affect the signal transmission performance of the modulated microwave signal in RoF applications. To address this challenge, single optical feedback and double optical feedback are applied in the experiments. The experimental results demonstrate that both single feedback and double feedback can reduce the linewidth of the generated microwave to about one tenth of linewidth without the optical feedback. However, single optical feedback may induce many side peaks due to external cavity frequency from the feedback cavity, the feedback phase needs to be carefully adjusted to suppress the side peaks. The side peaks can be suppressed by introducing the second optical feedback. The double optical feedback can also significantly enhance the stability of the generated microwave. The results of the numerical simulations are in good agreement with the experimental results.

The other important dynamic of semiconductor lasers is chaos, which has attracted considerable research interest due to its many potential applications in secure communications, chaotic optical time-domain reflectors, chaotic lidars and physical random number generators. Optical feedback is the simplest method to generate chaos in semiconductor lasers, but a typical chaos generated by optical feedback has unwanted recurrence features termed time delay (TD) signature because of the optical round trip in the external cavity. The complexity, bandwidth and TD signature of chaos are the three main parameters for evaluating its applicability in abovementioned application scenarios. In order to find the correct operating parameters to achieve low TD signature and high complexity of chaos simultaneously, in this thesis, the influence of bias current and the feedback strength on the complexity and time-delay signature of chaotic signals in semiconductor lasers with optical feedback is investigated experimentally and theoretically. In the experiment, the effect of the data acquisition method on quantification of complexity is also examined. The experimental results show that the TD signature is approximately in an inverse relationship with the complexity of chaos when the semiconductor laser is subject to low or strong optical feedback. However, the inverse relationship disappears when the laser operates at higher bias currents with

Songkun Ji

intermediate feedback strength. Numerical simulation based on Lang Kobayashi laser equations show qualitative agreements with the experimental results.





# Contents

<b>1 INTRODUCTION .....</b>	<b>12</b>
<b>2 LITERATURE REVIEW.....</b>	<b>15</b>
2.1 Semiconductor Lasers with Optical Injection .....	15
2.2 Semiconductor Lasers with Optical Feedback .....	23
2.2.1 Dynamics of Semiconductor Lasers under Optical Feedback.....	23
2.2.2 Chaos in Laser Systems .....	27
2.3 Photonic Microwave Generation .....	34
2.3.1 Microwave Generation Techniques .....	35
2.3.2 Period-one Oscillation for Photonic Microwave Generations.....	37
<b>3 PHOTONIC MICROWAVE GENERATION IN AN OPTICALLY INJECTED VCSEL .....</b>	<b>40</b>
3.1 Chapter Introduction .....	40
3.2 Experimental Setup and Data Acquisition .....	40
3.2.1 Experimental Setup for Laser Characterization .....	41
3.2.2 Experimental Setup for Photonic Microwave Generation .....	44
3.3 Experimental Result .....	47
3.3.1 Characterization .....	47
3.3.2 Fundamental Frequency of the generated Photonic Microwave.....	49
3.3.3 Microwave Power Measurement .....	54
3.4 Simulation Model.....	56
3.5 Numerical Results .....	58
3.5.1 L-I curve .....	58
3.5.2 Dynamic state evolution .....	59
3.5.3 Bifurcation in VCSEL Subject to Parallel Injection .....	61
3.5.4 Dynamical States Mapping of the Parallel Optical Injection VCSEL .....	63
3.5.5 Microwave Frequency.....	64
3.5.6 Microwave Power .....	65
3.5.7 Effect of Linear Dichroism on Microwave Frequency and Power .....	68
3.5.8 Effect of Linear Birefringence on Microwave Frequency and Power .....	71
3.6 Chapter Summary .....	72
<b>4 STABILIZATION ON VCSEL BASED PHOTONIC MICROWAVE GENERATION.....</b>	<b>73</b>
4.1 Chapter Introduction .....	73
4.2 Experimental Setup and Data Acquisition .....	73
4.3 Experimental Result .....	75
4.3.1 Characterization .....	75
4.3.2 Single Feedback.....	76
4.3.3 Double feedback.....	79
4.4 Numerical Study .....	85
4.4.1 Simulation Model .....	85
4.4.2 Single Feedback.....	87

4.4.3 <i>Double feedback</i> .....	92
4.5 Chapter Summary .....	98
<b>5 EFFECT OF BIAS CURRENT ON COMPLEXITY AND TIME DELAY</b>	
<b>SIGNATURE OF CHAOS .....</b>	<b>99</b>
5.1 Chapter Introduction .....	99
5.2 Experimental Setup and Data Acquisition .....	99
5.3 Digital Acquisition Methods Discussion.....	101
5.3.1 <i>Experimental method</i> .....	101
5.3.2 <i>Simulation Method</i> .....	104
5.4 Experimental Result .....	109
5.5 Simulation Result .....	112
5.6 Chapter Summary .....	117
<b>6 CONCLUSION .....</b>	<b>118</b>
6.1 Summary .....	118
6.2 Future Work.....	119
<b>7 REFERENCE .....</b>	<b>121</b>
<b>8 APPENDICES.....</b>	<b>142</b>
8.1 List of Publications .....	142
8.2 Conference Attendant / Paper Accepted .....	144

## List of Tables

Table 2.1 Comparison of Photonic Microwave Techniques.....	37
Table 3.1 Values used for simulation .....	58
Table 4.1 Values used for simulation .....	87

## List of Figures

Figure 2.1 Injection Locking System .....	16
Figure 2.2 Locking and unlocking regions in phase space of frequency detuning and injection field. This figure is taken from Ref.[3]......	17
Figure 2.3 (i) Optical spectra, (ii) intensity time series, and (iii) phase portraits in the complex plane of the electric field for the laser in (a) stable locking, (b) P1 oscillation, (c) P2 oscillation, and (d) chaotic states. The optical spectra are offset to the optical frequency of the free-running laser. The phase portraits are extracted by reference to the rotating frame of the injection field. This figure is taken from Ref. [58]. .....	18
Figure 2.4 Experimentally obtained dynamic map from measured optical spectra of a single mode DFB laser under optical injection. This figure is taken from [3]. ....	19
Figure 2.5 Schematic layer structure of VCSEL. (R. Michalzik 2013).....	20
Figure 2.6 Experimental stability map of the 1550nm-VCSEL subject to parallel polarized injection; Different regions are observed: SIL (stable injection locking), P1 (Period 1), P2 (period 2) and CH (chaos); This figure is taken from Ref. [19]. .....	22
Figure 2.7 Experimental observation different regimes of operation for lasers under external feedback. This figure is taken from Ref.[70] .....	24
Figure 2.8 Optical spectra in regime IV. (a) periodic state with -40db feedback. (b) quasi-periodic oscillation with -30db feedback. (c) chaotic state with -20db feedback. This figure is taken from Ref.[3] .....	25
Figure 2.9 Numerical simulation of the dynamics of a semiconductor laser under optical feedback. Time series (first column), attractors (second column), and power spectra (third column). Feedback ratio of (a) 0.5%, (b)1.0% and (c)2.0%.....	27
Figure 2.10 Schematic of laser diode subject to optical feedback from an external reflector. ....	29

Figure 2.11 the numerically calculated bifurcation diagrams with bias current equals 1.3 times of the threshold current. This figure is taken from [89].	31
Figure 2.12 Auto-correlation function of a chaotic time series. This figure is taken from [54].	32
Figure 2.13 Schematic of a simple microwave photonic link	35
Figure 3.1 IEEE-488 (GPIB) Cable/Connector Characteristics (Photo credit: Infinite Electronics International)	41
Figure 3.2 Experimental setup for laser characterization in fiber setup. PC: Polarization Controller, PBS: polarization beam splitter, OSA: optical spectrum analyzer, PM: power meter.	42
Figure 3.3 Laser characterization workflow utilizing LabVIEW. OSA: Optical Spectrum Analyzer. PM: Power Meter.	43
Figure 3.4 LabVIEW interface for the laser characterize experiment.	44
Figure 3.5 The experimental setup. ML: Master laser, SL: Slave laser, PC: polarization controller, Atten: digital attenuator Cir: Optical circulator. ISO: optical isolator, 3dB: 2 by 2 3dB fiber coupler, Dec: photodetector, RF: radio frequency spectrum analyzer. FPI: Fabry-Perot interferometer.	45
Figure 3.6 Automatic data acquisition workflow for photonic microwave generation utilizing LabVIEW. ESA: Electrical Spectrum Analyzer. OSC: Digital Oscilloscope.	46
Figure 3.7 LabVIEW interface for the photonic microwave generation experiment.	47
Figure 3.8 Characterization of the VCSEL used in Chapter 3. Red line is representing the total optical power, blue line and yellow line represent the optical power of Y-polarisation and X-polarisation, respectively	48
Figure 3.9 Optical Spectrum Information at different bias current.	49

Figure 3.10 Power spectra of the VCSEL output at injection condition $(f_i, P_i)$ of (a) $(-2.9GHz, 0.37mW)$ , (b) $(-2.9GHz, 0.74mW)$ , (c) $(4.1 GHz, 0.28 mW)$ , (d) $(8.17 GHz, 0.28mW)$ . .....	51
Figure 3.11 Generated microwave frequency as function of (a) frequency detuning and (b) injection power. ....	53
Figure 3.12 Mapping of the fundamental frequency $f_0$ . ....	54
Figure 3.13 Mapping of the fundamental microwave frequency power $Pf_0$ . ....	55
Figure 3.14 Second harmonic distortion as a function of (a) the frequency detuning, (b) the injection power. ....	56
Figure 3.15 Simulated L-I curve of the VCSEL using the parameter listed in Table 3.1. ....	59
Figure 3.16 Optical spectrum with the frequency offset of the free-running slave laser frequency. The injection frequency detuning is kept constant at $\nu_{inj} = 6GHz$ which is highlighted by the arrows. The injection strength $\eta\gamma$ is varied to obtain different states: (a) stable locking; (b) DSB period-one; and (c) SSB period-one. ....	61
Figure 3.17 (a)Bifurcation diagram of the intensity extrema versus the injection strength. (b) The same diagram zoomed in at Zone#2. ....	62
Figure 3.18 Non-linear dynamical states mapping of optically injected VCSEL under varied injection conditions. ....	63
Figure 3.19 Mapping of the fundamental frequency. ....	64
Figure 3.20 Mapping of the normalized microwave power. ....	66
Figure 3.21 the power spectrum under the injection condition of $\eta\gamma, \nu_{inj} = 10GHz, +6GHz$ . ....	67
Figure 3.22 SHD mapping of the electrical signal. ....	68

Figure 3.23 Fundamental frequency(a) and microwave power versus the linear dichroism. ....	69
Figure 3.24(a) fundamental frequency increasing with the increase of the injection strength at three different linear dichroism ( $\Gamma_a$ ). (b) Microwave power versus the increasing injection strength. ....	70
Figure 3.25 Fundamental frequency(a) and microwave power versus the linear dichroism. ....	71
Figure 4.1 The experimental setup. ML: Master laser, ISO: Optical isolator, Mir.: Mirror, $\lambda/2$ : Half-wave plate, BS: Beam splitter, Atten: Optical attenuator, PM: Power meter, Dec: Photodetector, RF: Radio frequency spectrum analyzer, PZT: Piezo stage. ....	74
Figure 4.2 Power spectra of the VCSEL. (a) without optical feedback, (b) with optical feedback from cavity 1, (c) with optical feedback from cavity 2. ....	77
Figure 4.3 (a1-c1) Power spectra of the VCSEL under injection condition of $(\Delta f, P_{inj}) = (10.43 \text{ GHz}, 0.703 \text{ mW})$ with different PZT distance, (d1) SPS phase condition and SP phase condition states as a function of the PZT moving distance. ....	78
Figure 4.4 (a2-c2) Power spectra of the VCSEL under injection condition of $(\Delta f, P_{inj}) = (10.73 \text{ GHz}, 0.689 \text{ mW})$ with different PZT distance, (d2) SPS phase condition and SP phase condition states as a function of the PZT moving distance. ....	79
Figure 4.5 Power spectra of the VCSEL with (a) single feedback, (b) double feedback. ....	80
Figure 4.6 Power spectra of the VCSEL. (a) Without optical feedback, (b-d) with double feedback and the total feedback power is (b) $3 \mu W$ , (c) $6 \mu W$ , (d) $9 \mu W$ . ....	81
Figure 4.7 (a) Linewidth and (b) fundamental frequency of the generated microwave as a function of the feedback power. ....	82



- Figure 4.8 Power spectra of the VCSEL when the sweep time of the RF spectrum analyzer is set at 30 seconds. (a) Without feedback, (b-d) with double feedback and the total feedback powers are (b)  $3\mu W$ , (c)  $6\mu W$ , (d)  $9\mu W$ . .....83
- Figure 4.9 The power spectra of the VCSEL with the different feedback configurations. The left and right columns are for the sweep time of the RF spectrum analyzer of 50 millisecond and 30 seconds, respectively. (a1), (a2) single feedback with SPS phase condition, (b1), (b2) double feedback with SPS phase condition, (c1), (c2) double feedback with SP phase condition. ....84
- Figure 4.10 Power spectra under feedback strength of (a) zero, (b)  $0.6GHz$ , (c)  $1.4GHz$  and (d)  $2.0GHz$ . ....88
- Figure 4.11 Linewidth and MSPR versus feedback strength. (a) Under the injection condition of  $\eta y, v_{inj} = 25GHz, +6GHz$ , (b)  $\eta y, v_{inj} = 20GHz, +10GHz$  .....89
- Figure 4.12 Fundamental frequency and its power influenced by the feedback phase variation in the step of  $0.2\pi$ . Under the injection condition of  $\eta y, v_{inj} = 20GHz, +10GHz$  for (a)(b) and  $\eta y, v_{inj} = 23GHz, +8GHz$  for (c)(d). ....90
- Figure 4.13 MSPR influenced by the feedback phase variation in step of  $0.2\pi$ . Under the injection condition of  $\eta y, v_{inj} = 20GHz, +10GHz$  for (a) and  $\eta y, v_{inj} = 23GHz, +8GHz$  for (b). ....91
- Figure 4.14 Map of the P1 microwave linewidth under injection condition of  $\eta y, v_{inj} = 20GHz, +10GHz$  and feedback strength from 0 to  $0.8GHz$  for each feedback path. ....92
- Figure 4.15 Numerical simulation of RF spectra of the VCSEL with single feedback (black curve) and double feedback (red curve). Feedback phase  $\varphi$  from the short cavity (a)  $0\pi$ ; (b)  $0.2\pi$ ; (c)  $0.8\pi$ ; (d)  $1.6\pi$ . ....94
- Figure 4.16 Numerical simulation of RF spectra of the VCSEL with the single feedback (black curve) and the double feedback (red curve). For the long cavity feedback strength equals to (a)  $0.2GHz$ , (b)  $0.5GHz$ , (c)  $0.8GHz$  and (d)  $1.0GHz$ . while maintaining the short feedback strength at  $0.6GHz$ . ....95

Figure 4.17 Mapping of the side peak suppression behaviors. ....	96
Figure 4.18 Mapping of the “good” P1 microwave by double optical feedback setup. .....	97
Figure 5.1 (a) Free space experimental setup, (b) all-fiber experimental setup. L: Lens; BS: beam splitter; M- mirror; ND: neutral density filter; ISO: optical isolator; D: detector; OSC: oscilloscope; RF: radio frequency spectrum analyzer; Cir: optical circulator; 3dB: 3dB optical coupler; PC: polarization controller. Grey (Red in color) lines represent the laser beam travel in free space. Black lines represent the laser beams travel in the optical fiber. ....	100
Figure 5.2 (a) The time trace of the laser output and (b) the normalized PE as a function of embedding delay time. The inset in (a) is the time series in a shorter time interval.....	102
Figure 5.3 The complexity of the chaotic signal as a function of bias current. ....	103
Figure 5.4 The complexity of the chaotic signal as a function of bias current under a fixed vertical scale of the oscilloscope. (a) No optical attenuator before the detector, (b) with optical attenuator before the detector. ....	104
Figure 5.5 Numerical simulation of the complexity as a function of bias current. ....	106
Figure 5.6 The normalized PE calculated from (a) the time series calculated from the rate equations; (b) the time series being digitized to 255 levels; (c) the time series being digitized to 127 levels; (d) the time series whose amplitude has been reduced by half and digitized to 255 levels. ....	108
Figure 5.7 Numerical simulation effect of the digitized levels on the average normalized PE (circles), the normalized PE at $\tau_{ext}$ (squares) and the depth of the trough at $\tau_{ext}$ (triangles) as a function of digitized levels. ....	109
Figure 5.8 The time traces (first column), RF power spectra (second column autocorrelation coefficient curves (third column) and permutation entropy curves (fourth column)) of the chaotic signal. The top, middle and bottom rows represent bias currents of 50mA, 60mA and 70mA, respectively. ....	110

Figure 5.9 The TD signature and complexity of chaos as a function of the normalized bias currents in (a) the free space experimental setup, (b) the all-fiber experimental setup. ....	111
Figure 5.10 Numerical results of the TD signature and complexity as a function of the normalized bias currents with a feedback strength of (a) $60ns - 1$ , (b) $30ns - 1$ , (c) $9.32ns - 1$ . ....	114
Figure 5.11 Maps of (a) TD signature, (b) complexity of chaos with varying bias current and feedback strength.....	116

## List of Abbreviations and Acronyms

RoF	Radio-over-fiber
DFB	Distributed Feedback Lasers
VCSEL	Vertical-cavity Surface-emitting Lasers
QD	Quantum Dot Lasers
TD	Time Delay
P1	Period-one Oscillation
P2	Period-two Oscillation
P4	Period-four Oscillation
DBR	Distributed Bragg Reflector
IL	Injection Locking
OPPLs	Optical Phase-lock Loops
OEO	Optoelectronic Oscillator
GPIB	General Purpose Interface Bus
AC	Autocorrelation
PE	Permutation Entropy
E/O	Electrical-to-optical
EMI	Electromagnetic Interference
CW	Continuous Wave
IEEE	Institute of Electrical and Electronics Engineers
ML	Master Laser
SL	Slave Laser
PC	Polarization Controller
FPI	Fabry-Perot Interferometer
OSA	Optical Spectrum Analyzer
ESA/RF	Electrical Spectrum Analyzer or Radio-Frequency Analyzer
OSC/DPO	Digital Phosphor Oscilloscope

# 1 Introduction

Semiconductor lasers, as one of the most commonly used types of lasers, play an important part in our everyday gadgets, such as mobile phone, barcode readers, laser pointers, CD/DVD/Blu-ray disc reading/recording, laser printing, laser scanning and so on. The semiconductor laser was first developed in 1962 [1] with a very high threshold current and at a very low temperature. Only until 1970s, semiconductor lasers with continuous wave operations under room temperatures were succeeded [2]. The operation dynamics of semiconductor lasers are very sensitive to external interventions. Semiconductor lasers show rich nonlinear dynamics when they are subject to optical injection, feedback or modulation. These nonlinear dynamics underpin a wide range of applications including photon microwave generation, encrypted communication, fast random bit sequence generators, biological heuristic information processing, etc. In this thesis, the research topics are focused on the detailed explorations of optical effects on the nonlinear dynamical properties of semiconductor lasers with emphases on photonic microwave generation based on period one dynamic of semiconductor lasers and lasers' chaotic dynamic.

Photonic microwave generation is an important research topic in microwave research areas. Because microwave frequencies of up to  $100\text{GHz}$  are expected to be implemented in imminent arrival  $5\text{G}$  networks, the traditional method of using electronic circuits to generate such high frequency microwave signals is, however, impractical. Photonic microwave generation, which uses photonics to assist microwave generation, is a cost-effective promising alternative approach. The primary application of photonic microwave generation is radio-over-fiber (RoF) transmission systems, where light is modulated by a radio frequency signal and the modulated optical signal is transmitted over the optical fiber link. The technical advantages of RoF include low transmission loss, large bandwidth, potentially high cost-effectiveness and immunity to electromagnetic interference. The RoF technique may enable the convergence of separately developed and operated legacy optical and wireless networks, which is widely regarded as a significant milestone towards practically realizing  $5\text{G}$  networks.

As such from the system/network design point of view, it is highly desirable if microwave signals are directly generated in the optical domain without utilizing expensive, bulky and low-speed electrical-to-optical conversion. Many photonic microwave generation techniques have been proposed and demonstrated. Among these techniques, photonic microwave generation based on period one (P1) dynamic exhibits many advantages. The details photonic microwave generation techniques will be explained in chapter 2.

Photonic microwave generation based on P1 dynamic associated with DFB lasers has been studied extensively; this method shows many promising features. Vertical-cavity surface-emitting lasers (VCSELs), as a special type of semiconductor lasers, offer extra unique advantages over the DFB lasers, such as low production cost, low threshold current, low power consumption, circular beam profile, single-longitudinal-mode operation and longevity. Thus, special effort of this thesis is made to investigate broad tunable photonic microwave generation based on P1 dynamic of off-the-shelf VCSELs. Such study is valuable for providing effective means to further reduce the installation and operation cost of the RoF transmission systems.

Due to spontaneous emission noise in the semiconductor laser, P1 dynamic inherently imposes phase noise, which increases the microwave linewidth of the generated microwave. This also considerably affect the transmission performance of the modulated microwave signal over the RoF systems. To address this challenge, in this dissertation work extensive investigations are undertaken to explore cutting-edge techniques capable of not only reducing the linewidth of the generated microwave but also improving its stability.

The other important dynamic of semiconductor lasers is chaos. Ohtsubo Junji [3] describes that chaos is a phenomenon of irregular variations of system outputs that are governed by a set of deterministic equations. A chaotic system is that the current state of the system depends on the previous state in a rigidly deterministic way, however, the systems' outcome shows random variations. Chaos is always companied by nonlinearity. Since lasers themselves are nonlinear systems, thus chaos can often occur in laser systems. Chaos has many potential applications including secure communications [4], chaotic logic gates [5], chaotic optical time-domain reflectors [6]–[8], chaotic lidars [9], and physical random number generators [10], [11]. Optical

feedback is the simplest method of generating chaos in semiconductor lasers, but a typical chaos generated by optical feedback has unwanted recurrence features termed time delay (TD) signature because of the optical round trip in the external cavity. From the practical application point of view, high complexity and low TD signature of chaos are always preferred. Simultaneous implementations of low TD signature and high complexity chaos is thus the second main goal of this thesis.

The thesis involves six chapters. Chapter 2 is the literature review, which presents rich nonlinear dynamics of semiconductor lasers induced by optical injection or optical feedback and photonic microwave generation techniques.

In chapter 3, photonic microwave generation based of period one dynamic in an optically injected VCSEL is experimentally and theoretically explored. The effects of the injection strength and frequency detuning on frequency and power of generated microwave are investigated in detail. Furthermore, the effects of the VCSEL parameters of linear dichroism and linear birefringence on the generated microwave are also analyzed numerically using a common spin flip model.

To further enhance the performance of the generated microwave, Chapter 4 extends the study of chapter 3 by implementing the optical feedback technique. Both experimental and theoretical studies on reducing the linewidth of the generated microwave are presented. Additionally, the stabilization of microwave frequency is also investigated experimentally.

In Chapter 5, the relationship between time-delay signature and complexity of chaos generated in a semiconductor laser with optical feedback is experimentally and theoretically studied. The impact of the data acquisition method on the quantification of chaos complexity is also discussed.

Chapter 6 summarizes the main results of this thesis and suggests future research work.

During this study, I have published 3 journal papers as the first author, 4 journal papers as the second author and 5 conference papers .

## 2 Literature Review

The dynamics of the semiconductor laser are well known and quite sensitive to external influences, such as optical feedback, modulation or optical injection [12], [13]. More specifically, the optical injection has reported providing enhanced modulation bandwidth [14] and also induces a variety of nonlinear dynamics including periodic oscillations and chaotic behavior [15], [16]. The complex nonlinear dynamical states from optical injection have been investigated in Fabry Perot laser [15], distributed feedback laser [17], multisection semiconductor laser [18] and vertical-cavity surface-emitting laser [17]–[29]. This chapter starts with an introduction and explanation of semiconductor laser's rich non-linear dynamics by reviewing the optical injected semiconductor laser's output, including its optical spectra, the intensity of the time series, and phase portraits in the complex plane of the electric field under different dynamical states. Then we look into the VCSEL's dynamics in brief due to VCSEL's nonlinear dynamics are highly comparable to the DFB lasers but also VCSEL has its unique polarization properties. The dynamics of a semiconductor laser with optical feedback are explained in later sections. The commonly used microwave generation techniques, with emphases on the techniques using optically injected lasers are also discussed since a large effort of this thesis is focused on utilizing VCSEL's P1 oscillation to generate broad tunable photonic microwave.

### 2.1 Semiconductor Lasers with Optical Injection

Semiconductor lasers feature high gain, low facet reflectivity, and amplitude-phase coupling through the  $\alpha$  parameter. It is sensitive to the optical injection from a different laser. Injection locking and unlocking behavior has been extensively studied [30]–[35]. The injection locking can be a useful tool for controlling and stabilizing the laser's oscillation. In the past years, the research topics has been more focused on the locking condition. Recent years, increasing numbers of studies have moved interests into the rich varieties of dynamics such as the four-wave mixing[35]–[38], period-doubling[39]–[42] and chaos[39]–[57]. The dynamic characteristics of locking and



unlocking regimes in optically injected semiconductor lasers will be focused in this section.

The technique of injection locking is frequently used to lock the frequency and stabilize the output oscillation of a slave laser. The system of injection locking is straightforward, and it is demonstrated in Figure 2.1. For the optical injecting locking, the two lasers need to be in almost same oscillation frequency (frequency differences within a few GHz ranges). Light from a laser (master laser) is fed into the active layer of the other laser (slave laser). Then under the appropriate condition of injection strength and frequency detuning from the master laser, the slave laser will operate in synchronization in optical frequency with the master laser.

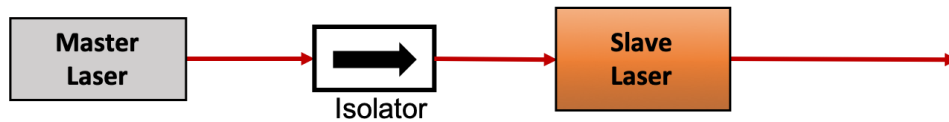


**Figure 2.1 Injection Locking System**

Optical injection technique was initially developed to stabilize the output of the slave laser's oscillation, in which, at first glance, it can seem to be controversial to realize that the slave laser can also be destabilized by the optical injection. However, the optical injection to a laser is an introduction of the extra degree of freedom of slave laser's nonlinear dynamics. Figure 2.2 is created by Junji Ohtsubo based on his numerical study [3], it shows the areas of optical injection locking in the phase space for the frequency detuning between the master and slave lasers and the injection ratio. The solid lines indicate the boundaries between optical injection locking and non-locking regions. In the non-locking region, when the frequency detuning close to zero, various dynamics such as chaotic oscillations and four-wave mixing can be found. Within the region of the optical injection locking, there are stable and unstable locking areas. The boundary of the unstable and stable injection locking areas is denoted by a dotted curve. The unstable injection locking area refers to the condition that within specific parameter ranges, the chaotic bifurcations can be found in the area. In addition,

the reason for the unsymmetrical distributed area between stable and unstable locking area is due to the non-zero  $\alpha$  parameter value.

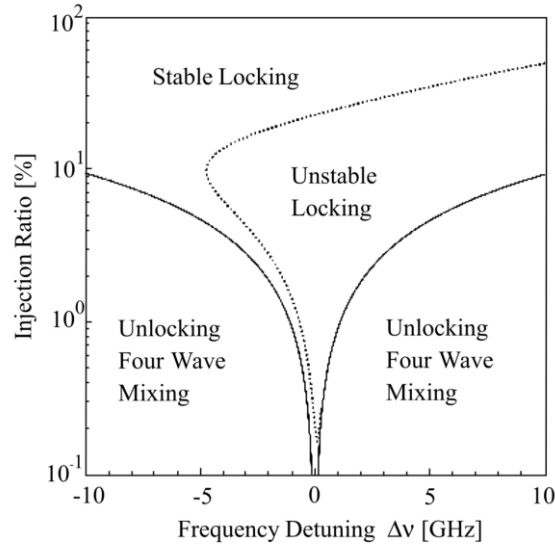


**Figure 2.2 Locking and unlocking regions in phase space of frequency detuning and injection field. This figure is taken from Ref.[3].**

Junping Zhuang in his thesis shows the simulated optical spectra, the intensity of the time series, and phase portraits in the complex plane of the electric field of an optically injected edge-emitting laser when the injection strength  $\xi_i$  is varied with a fixed frequency detuning. His results demonstrate that the different dynamical states can be excellently categorized using optical spectra, output intensity or E-field phase.

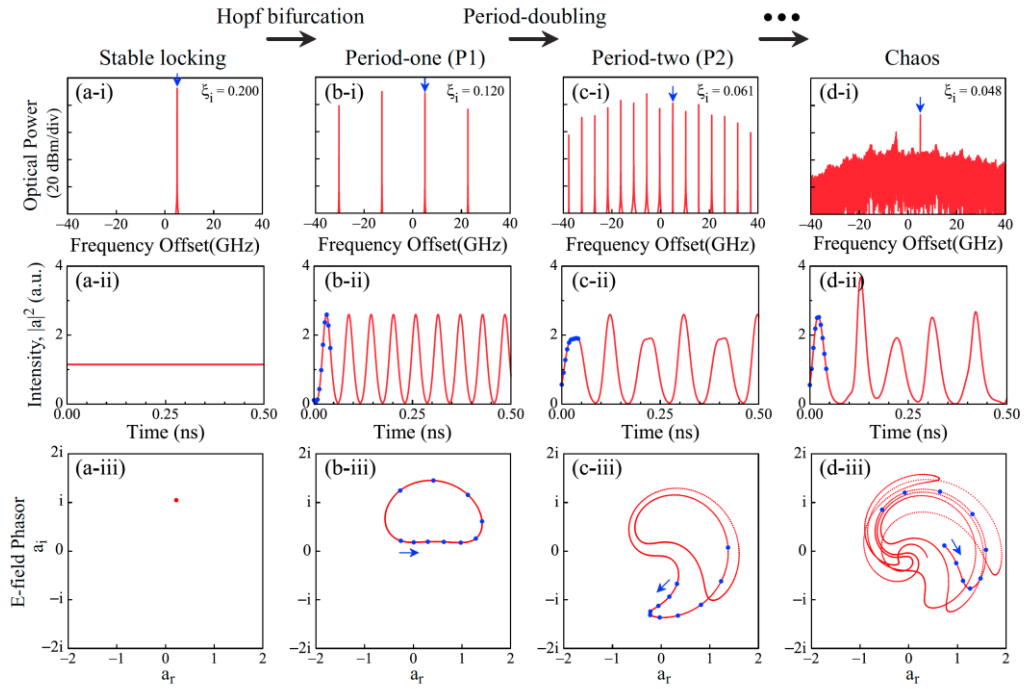


**Figure 2.3 (i) Optical spectra, (ii) intensity time series, and (iii) phase portraits in the complex plane of the electric field for the laser in (a) stable locking, (b) P1 oscillation, (c) P2 oscillation, and (d) chaotic states. The optical spectra are offset to the optical frequency of the free-running laser. The phase portraits are extracted by reference to the rotating frame of the injection field. This figure is borrowed from Junping Zhuang's Ph.D Thesis.**

In Figure 2.3(a), the injection is relatively strong, resulting in the injection locking situation, a single frequency in the optical spectrum, a constant intensity in the time series and a single dot in the phase portrait. Decrease the injection strength in Figure 2.3(b), the laser enters the P1 state, where the sidebands are separated from injection frequency (indicated by the blue arrow) with the same amount of spacing. The time series shows a periodic oscillation and the phase portraits shows a limit cycle. Keep decreasing the injection strength to enter the P2 state, in Figure 2.3(c) the optical spectrum shows subharmonics, the optical components separation is below half of the amount in P1 oscillation. The intensity of the time series shows two distinct peak values. The phase portrait in the P2 state shows the limit cycle with a double period. Finally, in Figure 2.3(d) the laser is driven into the chaotic oscillation state, where the optical

spectrum shows a broadened continuous spectrum. The chaotic time series intensity has no consistent peak values, and the phase portraits do not repeat itself.

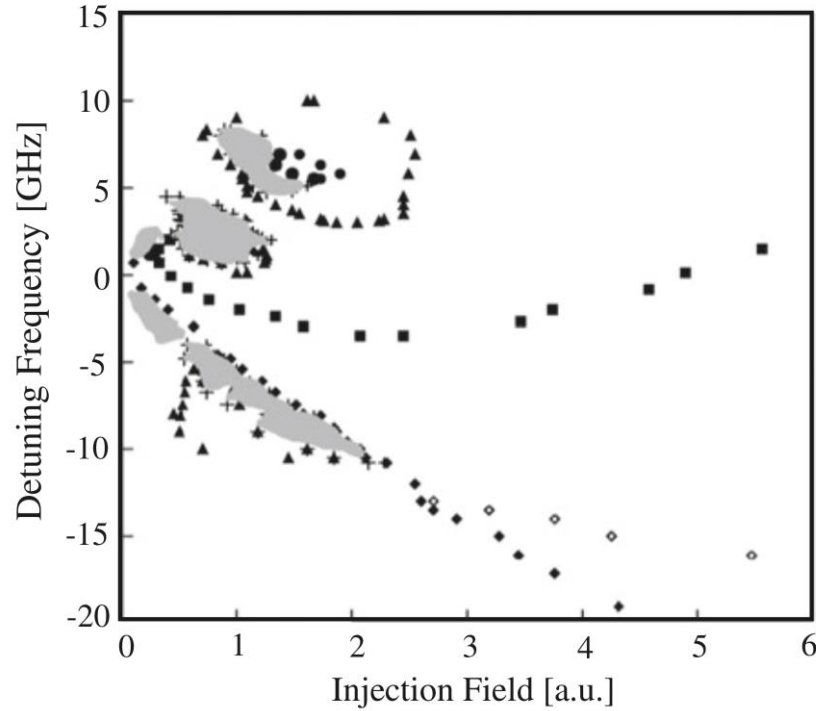


**Figure 2.4 Experimentally obtained dynamic map from measured optical spectra of a single mode DFB laser under optical injection. This figure is taken from [3].**

To better visually observe where the different dynamical state lays in the between the injection parameters, a map is often created. The mapping of the different dynamic region of a semiconductor laser subject to optical injection is presented by Junji Ohtsubo in Figure 2.4. This figure is mapped by adjusting the frequency detuning and the injection field. The detuning frequency is calculated as the master laser's frequency minus the free-running lasing frequency of the slave laser. In Figure 2.4 diamond-filled symbol in negative frequency detuning is the boundary between unstable and stable operations. This boundary corresponds to the saddle-node boundary between the stable locking and unlocking operations. The open diamonds display the unlocking and locking transitions of the bistability region. The square mark detuning is

the boundary named Hopf bifurcation, it separates the stable locking region and limit cycle dynamics. Triangle is the boundaries for period-two (P2) dynamics. Inside these regions the dynamics are complex. The circle bounded region is the period-four (P4) region. Finally, the vast region bounded by squares and above the zero-frequency detuning, exclude all other regions stated above are the period one (P1) region, which it is the leading region this thesis is focused on for the photonic microwave generation, and it is discussed in section 2.3.2 (page 37).

## VCSELs Subject to Optical Injection

Semiconductor lasers can be categorized into two classes. Edge-emitting lasers, and surface emitting lasers. Edge-emitting lasers are the laser that the light is guided and propagated in the direction along the wafer surface of the laser diode and reflected or coupled out at the cleaved edge of the semiconductor chip. Surface-emitting laser, where the laser light is guided in the direction that is perpendicular to the semiconductor chip wafer surfaces. The vertical-cavity surface-emitting laser (VCSEL) as the name suggests, falls into the surface-emitting laser category.

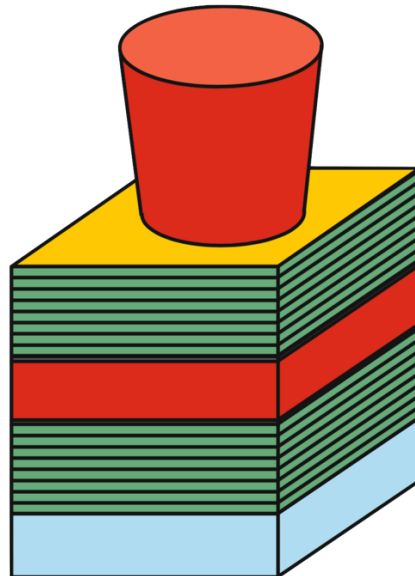


**Figure 2.5 Schematic layer structure of VCSEL. (R. Michalzik 2013).**

Figure 2.5 by R. Michalzik, represents a simply schematic structure layout for a typical vertical-cavity surface-emitting laser (VCSEL). The active layer is indicated with red color, two parallel mirrors with over 95% reflectivity (green color) are placed on the top and the bottom of the active layer. These mirrors are often called Distributed Bragg Reflector (DBR) mirrors, which have the properties of low thermal and electrical resistance and high reflectivity. VCSELs have short cavity length around  $1\mu\text{m}$ , single longitudinal mode operation is regularly expected due to this reason.

Increasing popularity in VCSELs are coming from the combination of unique properties. Compare to the DFB lasers, VCSELs offer many advantages that optical data transmission can benefit from; these are[59]

- Low threshold current of usually around 1mA as well as relatively small driving current enables low power consumption feature and easy design of the electronic driving circuit.
- Over 50% of power conversion efficiencies reduce power dissipation.
- Circular beam profiles, simplifying the design for beam-shape specific optics.
- Low production cost, about one-tenth of the price compare to DFB laser.
- High reliability and long lifespan usually rated around ten million hours at room temperature.

Due to these advantages combined with its nonlinear dynamic output enabled optical applications such as optical data communication, the increasing interests on optically injected VCSELs has raised in the past years[26], [28], [60]. The effect of orthogonally-polarized optical injection was used to generate polarization switching and polarization bi-stability in short[28], [60] and long[26], [61]–[64] wavelength VCSELs. Also variety of nonlinear dynamics subject to orthogonal injection has been reported theoretically[23], [65], [66] and experimentally[21], [67]. An experimentally measured stability map has been created for an 845nm-VCSEL subject to orthogonally-polarized injection in [21]. And the dynamics of 1550nm-VCSEL subject to parallel and orthogonal optical injection is also reported in [68].

Similar to edge-emitting lasers, the optical injection can also be used to induce the injection locking (IL) and other non-linear dynamical state in VCSELs. Reportedly in [69], this technique has proven to enhance the performance of 1550nm VCSEL, increase the modulation bandwidth and relaxation oscillation frequency. A large part of this thesis is based on the nonlinear dynamics state of VCSEL devices subject to optical injection. The term parallel injection refers to the injection light's polarization direction is the same as the free running VCSEL's lasing polarization direction due to the VCSEL's unique polarization characteristics. Figure 2.6 is the experimental results published by L. Chrostowski [22], it shows the stability map of the VCSEL subject to parallel polarized injection.

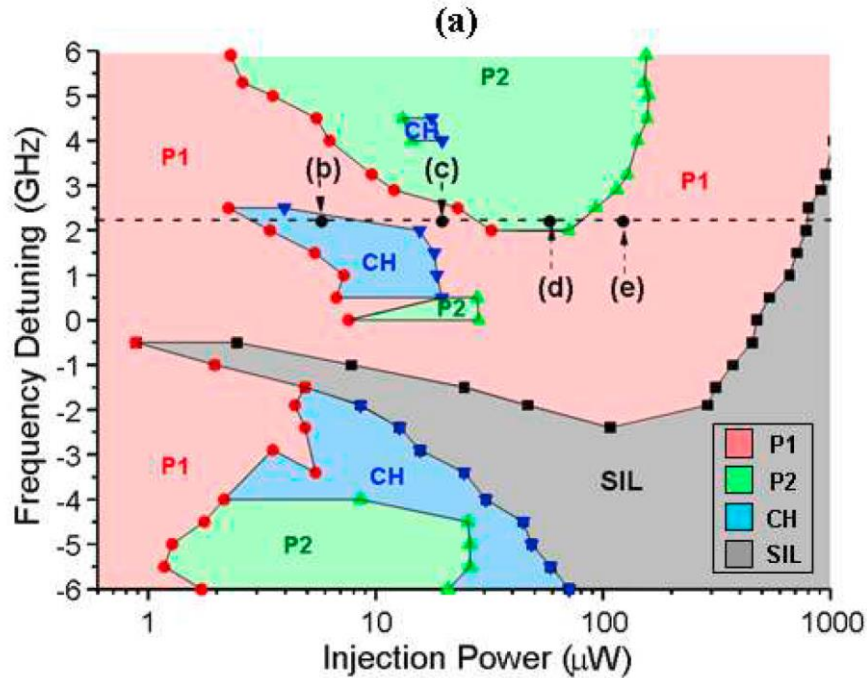


**Figure 2.6** Experimental stability map of the 1550nm-VCSEL subject to parallel polarized injection; Different regions are observed: SIL (stable injection locking), P1 (Period 1), P2 (period 2) and CH (chaos); This figure is taken from Ref. [22].

In the stability map, many regions with different behavior can be observed, including periodic dynamics such as limit cycle (period-one, P1), period doubling (period-two, P2) and non-periodical dynamic Chaos region. It is noted that the stability

map and non-linear dynamics output of an optically injected VCSEL under parallel injection exhibits strong similarities with those reported in edge-emitting lasers.

## **2.2 Semiconductor Lasers with Optical Feedback**

It is quite well known that the semiconductors are very sensitive by the external influences and external optical feedback is undoubtedly one of them. In the past two decades, the rich varieties of dynamics and its effective introduced by the semiconductor optical feedback configuration has been studied extensively. This section focuses on the observations of the semiconductor laser emission in an optical feedback situation. The chaos in semiconductor laser systems will also be discussed.

### **2.2.1 Dynamics of Semiconductor Lasers under Optical Feedback**

The dynamics of such semiconductor lasers with optical feedback can be outlined as a function of the feedback intensity levels. Usually, these levels are named from weak feedback to moderated feedback to strong feedback. The weak feedback usually refers to the laser output having local bifurcation, while the moderated feedback can observe the global bifurcations. A local bifurcation occurs when a parameter change causes the stability of an equilibrium (or fixed point) to change, Global bifurcations occur when 'larger' invariant sets, such as periodic orbits, collide with equilibria. This causes changes in the topology of the trajectories in the phase space which cannot be confined to a small neighborhood, as is the case with local bifurcations. During strong feedbacks, the transition from coherence collapse to single mode narrow-line emission can be observed. Figure 2.7 is a helpful experimental diagram summarized by Tkach, R. and Chraplyvy, A.[70].



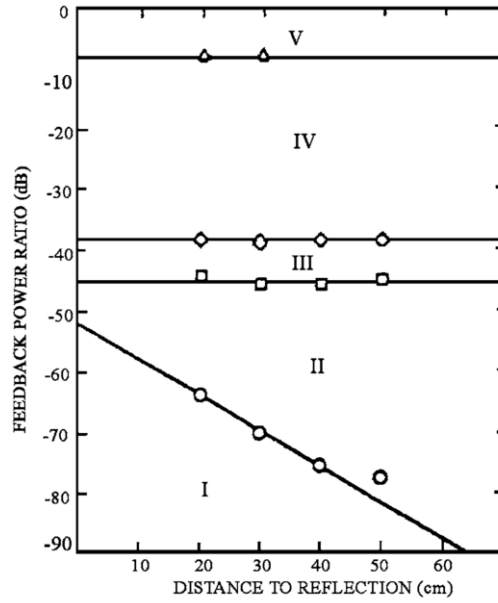


**Figure 2.7 Experimental observation different regimes of operation for lasers under external feedback. This figure is taken from Ref.[70]**

The Regime I is the lowest feedback levels; in this regime the laser is operating on a single external cavity mode that is transitioning from solitary laser mode. Depend on the feedback phase, the linewidth of the laser can either be broadened or narrowed. In Regime II and at the feedback level that depends on the external cavity length, the laser appears to split into two modes; it is caused by arising from the rapid mode hopping. The reason for the mode hopping is because of the noise. To enter the regime II, the condition is set to be  $C = 1$ . Where

$$C = \kappa\tau_c\sqrt{1 + \alpha^2} \quad (2.1)$$

In Equation (2.1) the  $\tau_c = 2L/c$  is named external cavity round trip time.  $\kappa$  is the effective feedback from the external cavity,  $L$  is the distance from the active layer to the external reflector,  $c$  is the speed of light. In Regime III, the laser enters into stable operation again. In this regime, the laser runs at the lowest linewidth external cavity mode with constant power. Keep increasing the feedback level independently from the feedback distance drives the laser to the Regime IV. The transition into the Regime IV is the transition to a chaotic state, which is also called coherence collapse. The

characteristic of this regime is that the optical spectra and noise spectra are dramatically broadened and contains many external cavity modes. R. Tkach and A. Chraplyvy [70] show us the experimental data of optical spectra when the laser is in regime IV in Figure 2.8. The laser first start to destabilize with the relaxation oscillation because of the increase of the feedback level in Figure 2.8(a), then, with the help of increasing the feedback level, the laser evolves into the quasi-periodic oscillation with observation of multiple spectral peaks in Figure 2.8(b). Finally, laser enters the chaotic oscillation and the linewidth broadening can clearly be found. This broadened linewidth can be as much as up to  $100\text{GHz}$  in some situation. The more detailed review about the chaos in laser system will be discussed in section 2.2.2 (page 27). The last Regime V is the laser operating in a steady state, which we will not be focused on due to the lack of dynamical output in this regime.

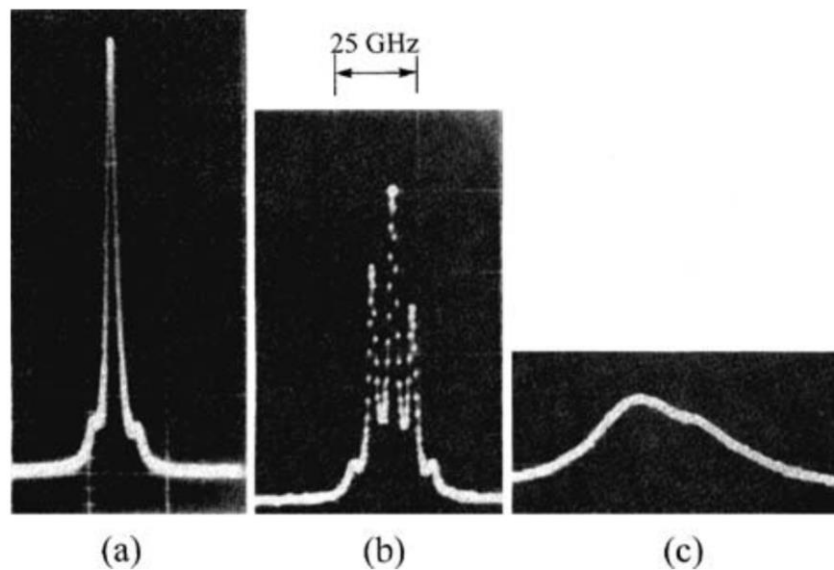


**Figure 2.8 Optical spectra in regime IV. (a) periodic state with -40db feedback. (b) quasi-periodic oscillation with -30db feedback. (c) chaotic state with -20db feedback. This figure is taken from Ref.[3]**

The dynamic behaviors of the laser output with fixed external reflection position and bias current, but the different feedback strength ratio is showed in figure

2.9, the first column is the time series. The second column shows the attractor, the attractor is a trajectory in the phase space, and it is frequently used for analyzing the chaotic oscillations. The third column is the power spectra. In Figure 2.9(a) the feedback ratio is 0.5%, similar to the optical injection situation discussed in section 2.1, the laser operates at period-one (P1) state. The stable oscillation leads to a single point in the phase space of the power and carrier density. P1 dynamic shows a single closed loop in the phase space. In the power spectrum, clear evenly spaced power peaks can be observed. When the feedback ratio is increased to 1.0%, the period-two (P2) oscillation appears as shown in Figure 2.9(b), in the P2 dynamic, the phase space displayed a double-loop. In the power spectrum, compared to the P1, more evenly spaced power peaks with smaller frequency separation situation can be found. Figure 2.9(c) shows the chaotic oscillation with feedback ratio increased to 2.0%. In this chaotic oscillation dynamic, the power spectrum is broadened around the relaxation oscillation frequency. The situation of feedback ratio equals 2.0% is the chaotic oscillation, and it will be continuously analyzed further in section 2.2.2 (page 23).

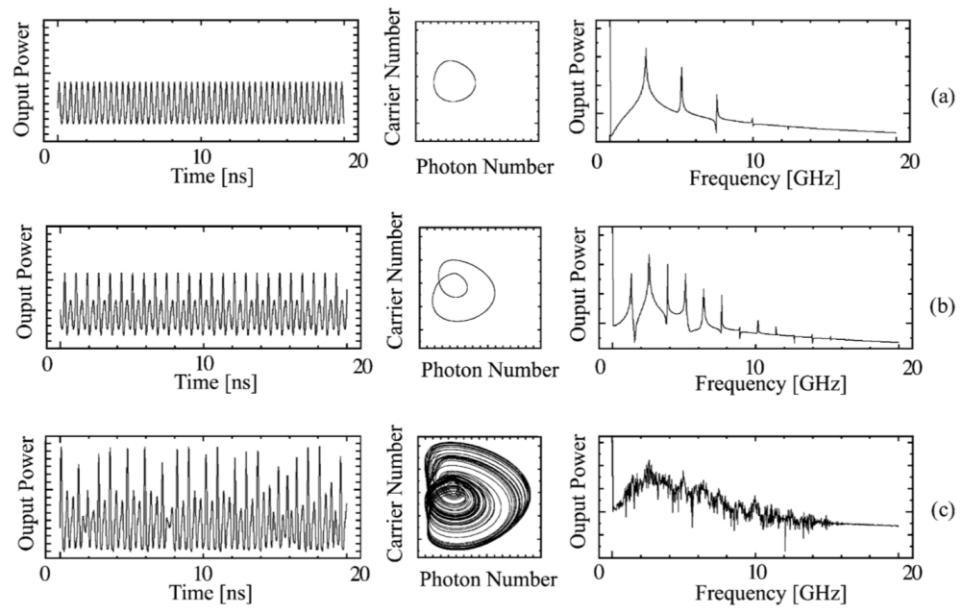


**Figure 2.9 Numerical simulation of the dynamics of a semiconductor laser under optical feedback. Time series (first column), attractors (second column), and power spectra (third column). Feedback ratio of (a) 0.5%, (b) 1.0% and (c) 2.0%. [71]**

### 2.2.2 Chaos in Laser Systems

Modern research of chaos started from the study of irregular and complex dynamics of the nonlinear system developed by Lorenz in 1963. Chaos provided not only a new perspective and viewpoint of nonlinear phenomena but also in itself a new physics. The output of chaos can be derived from models that are described by a set of deterministic equations; it is a phenomenon of irregular variations of systems' outputs. The chaos dynamic is referred to deterministic development with chaotic outcome[3]. Chaos is very much different from random events, the difference of chaos and random is clear: chaos is generated with the deterministic order in accordance, while the random system's output has no connection to the previous one. Despite the deterministic model characteristic, we cannot foresee the future output of the chaos because chaos is very sensitive to initial conditions. Even if the difference between the initial states of the two

chaotic systems is minimal, the behavior of the two chaotic systems will be completely different.

Chaos is constantly complemented by nonlinearity. The word “nonlinearity” stands for the measure properties value in the system is dependent by the earlier state in a complicated way. The nonlinear property does not promise the appearance of the chaotic dynamic, however, in another way around, some form of nonlinearity is required to perform a chaos system. Chaos behavior can occur in various fields, such as in physics, engineering, chemistry, biology, and even economics. Although these fields are drastically different from each other, some of the chaotic system in these fields can be described by the similar differential equations and same mathematical tools can be applied for the investigation of their chaotic dynamics.

The chaos theory in laser physics is developed independently until the year of 1975 when Haken discovered a strong relationship between the Lorenz equation and Maxwell Bloch equation in single mode lasers light-matter interaction modeling [72], [73]. Since lasers themselves are nonlinear system and can be usually characterized by three variables: field, the polarization of mater and population inversion, lasers are also respectable candidates for a chaotic system. Indeed, the first conclusive experimental report on laser chaotic trajectories was obtained by a  $CO_2$  laser in 1982 [74], [75]. The three variables in laser rate equations that describe the nonlinear equations are called Lorenz-Haken equation after Haken’s contribution in 1985[76]. Our focus is the class B semiconductor laser, which can be described with only two variables: the electric field and the carrier number.

### **Configurations for Achieving Chaos in Laser Systems**

Configurations for achieving laser diode chaos can be categorized as follows: external optical feedback[77], optical injection (unidirectional coupling)[47], [58], external current modulation[13], [78], loss modulation using saturable absorber[79], [80], opto-electronic feedback[81], [82], integrated on-chip chaotic laser diode[83], mode competition and nonlinear hybrid opto-electronic feedback[83]. External feedback is the most prominent configuration for laser chaos applications. It is commonly used in high-speed secure communications [47], [49], [84]–[88], chaotic logic gates [5], chaotic optical time-domain reflectors [6]–[8], chaotic lidars [9] and

physical random number generators [10], [11]. In the study, the configuration of achieving chaos is using the external optical feedback due to its simple setup. The physical setup to achieve the optical feedback is illustrated in Figure 2.10. By reflecting a small fraction of the laser emission into the laser diode cavity may result in the laser waveform and properties in a chaotic output [46]. The behavior of feedback induced chaos is very similar to the optical injection created chaos. The chaotic time series intensity has no consistent peak values, and the phase portraits do not repeat itself showed in Figure 2.3 (d). These rich dynamics is the result of competition between the laser's intrinsic relaxation oscillation frequency  $f_{RO}$  and the external cavity frequency  $f_{EC} = c/(2L)$ , where  $c$  is the speed of light and  $L$  is the distance from the laser to the external optical feedback reflector [45], [89]. However, one noticeable difference between the feedback induced chaos and the optical injection created chaos is that the chaos created by chaos has time delay signatures, this topic will be discussed in later sections.

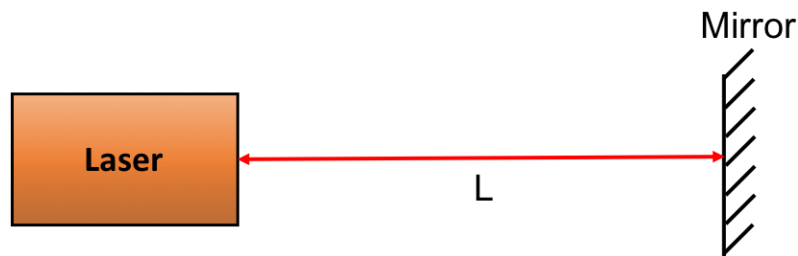


**Figure 2.10 Schematic of laser diode subject to optical feedback from an external reflector.**

### Optical Feedback Induced Chaos

As a continuous discussion at the end of section 2.2.1 (page 23), when the feedback ratio increased to 2.0%, the output of the laser can be observed as shown in Figure 2.9(c). No clear local extrema can be found in the time series in the first column. In the second column, the attractor is different from P1 or P2 situations or stable fixed state, within the closed compact space, the state goes around points, yet, it never visits

the same point. Although it looked like the trajectory crosses the previous route, it is because that the trajectory is only plotted in two-dimension space. In fact, it is reported that the trajectory goes around in a multi-dimensional space and it will never cross in such space [70]. This chaotic attractor is sometimes called a strange attractor.

Another useful tool to investigate the chaotic evolutions is the bifurcation diagram. The bifurcation diagram is created from the timeseries by taking the local peaks and valleys of the waveform for a parameter range. Atsushi Uchida has created a such bifurcation diagram in Figure 2.11. The horizontal axis is the feedback ratio  $r$ . For the region of  $r$  less than 0.35%. Increase the feedback ratio can observe two points corresponding to the peaks for the period-one oscillation. When the feedback ratio increased to 0.94%, the period-two oscillation starts and four states of peaks and valleys can be found. Keep increasing the feedback ratio, the laser enters the quasi-periodic state. For the feedback ratio over 1.36%, the laser oscillates at the mixed frequencies of relaxation oscillation mode, internal mode as well as the external modes. There is no clear line can be found in this region, laser enters the chaos state.

The above analyzation is based on the ignorance of the Langevin noise in the numerical oscillation. In the output of the laser with the presence of the noise, as long as the spontaneous emission is small, the chaotic behavior is scarcely affected. However, during the real-world experiment, the spontaneous emission of light has an important role for impacting the dynamics. Having the spontaneous emission noise, the waveform with high-frequency fluctuations is hard to obtain in bifurcation diagram resulting in the difficulty of observing the higher periodic oscillation, which means that normally P4 or higher periodic oscillation are not easily observable experimentally.

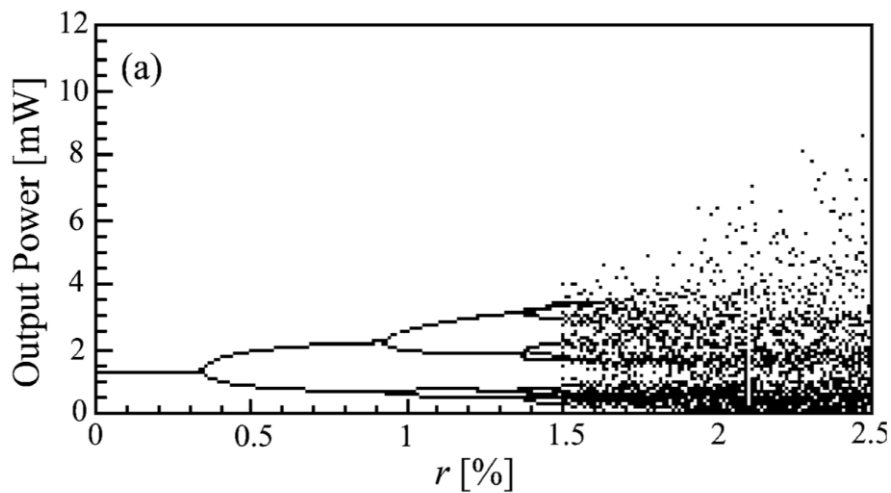


**Figure 2.11 the numerically calculated bifurcation diagrams with bias current equals 1.3 times of the threshold current. This figure is taken from [90].**

### Time Delay Signature

The previous section discussed that the semiconductor lasers with optical feedback are widely used to generate the chaotic time series. This chaotic output can be employed for cryptography, chaotic communication, and physical random bit generator, etc. In optical feedback created chaos system, it is proven that such chaos contains a signature of time delay, also known as round-trip time between the laser and the mirror[35], [91]. One common tool to study the time delay signature is to use the auto-correlation function of the chaotic waveform. It has a peak at the feedback delay, which its height is used to quantitatively estimate as the time delay signature. In Figure 2.12 the time delay signature is noted by the peak value of the auto-correlation coefficient of a chaotic time series at the delay time.



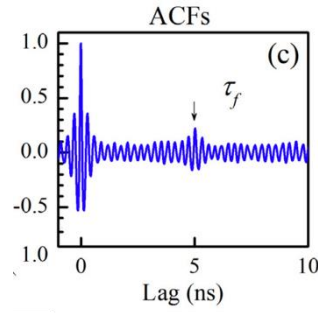


**Figure 2.12 Auto-correlation function of a chaotic time series. This figure is taken from [92]**

In a chaotic based communication secure system, the unpredictable and noisy appearance of the signals emitted by hyper-chaotic optical systems has been used to enhance security and privacy in communications. The chaotic carrier embeds and transmits the information, is decrypted by the synchronized end receiver which is a physical copy of the chaotic emitter. The security of the chaotic communication is relied on the complexity to reconstruct the high-dimensional attractor from its time series. However, the chaotic signal contains the time delay (TD) signature of the feedback loop, and as motioned earlier, the TD signature can be easily analyzed from the time correlation. The exposed time delay signature also allow the high-dimensional attractor into a reduced phase space, which leads to the vulnerable of the system by low-computational complexity identification techniques[35]. Therefore, it is essential to hide the TD signatures since these are essential keys in chaos-based secure communications.

The common methods to quantify the TD signature used are the autocorrelation (AC) function, delayed mutual information and permutation entropy [43], [54], [93]–[95]. The peak value of the AC coefficient at the feedback round trip time is used to quantify the TD signature in this paper. The autocorrelation coefficient is labelled as  $C$  and is defined as:

$$C(\Delta t) = \frac{\langle [I(t + \Delta t) - \langle I(t + \Delta t) \rangle][I(t) - \langle I(t) \rangle] \rangle}{\sqrt{\langle [I(t + \Delta t) - \langle I(t + \Delta t) \rangle]^2 \rangle \langle [I(t) - \langle I(t) \rangle]^2 \rangle}} \quad (2.2)$$

where  $\Delta t$  denotes the delay time,  $I(t)$  denotes the output intensity of the laser and  $\langle \cdot \rangle$  denotes time average. The peak value at the feedback round trip time ( $Cp$ ) can be expressed as:

$$C_p = \max |C(\Delta t)|_{\Delta t \in v_1(\tau_d)} \quad (2.3)$$

where  $\tau_d$  is the feedback round trip time. The measured TD peak value may not be located exactly at  $\tau_d$ . If a measured peak value is in the range of interval  $v_1(\tau_d) = (\tau_d - \tau_d \times r_1, \tau_d + \tau_d \times r_1)$ ; it will be considered as the peak value at the TD. According to the experimental data, 2% is selected as the value of  $r_1$ .

Nevertheless, the Chapter 5 is not on the subject of minimizing the TD signature; this chapter aimed to deliver the relationship between the bias current and TD signature and other vital characteristics in semiconductor laser's chaotic oscillation.

## Chaos Complexity and Permutation Entropy

Several techniques have been used to quantify the complexity of chaos, such as Lyapunov exponents [96], [97], strangeness of strange attractors [98] and permutation entropy (PE) [44], [99]–[101]. Permutation Entropy (PE) has a few advantages over other techniques, which includes easy implementation, faster computation and being robust to noise. This makes PE particularly attractive for using on experimental data, so PE is adopted to quantify the complexity of chaos in this thesis.

The PE method was first introduced by Bandt et al. [99]. In this method, the measured output intensity of the laser has  $N$  samples  $I_t$ , where  $t = 1, \dots, N$ . For a given time series  $\{I_t, t = 1, 2, \dots, N\}$ , let subsets  $S_q$  contain  $M$  samples ( $M > 1$ ) of the measured intensity and an embedding delay time  $\tau = nT_s$  ( $n$  is an integer number and  $T_s$  is the reciprocal of the sampling rate), the ordinal pattern of the subset is  $S_q = [I(t), I(t + \tau), \dots, I(t + (M - 1)\tau)]$ .  $S_q$  can be rearranged as  $[I(t + (r_1 - 1)\tau) \leq I(t + (r_2 - 1)\tau) \leq \dots \leq I(t + (rM - 1)\tau)]$ . Hence, any subset can be uniquely mapped into an “ordinal pattern”  $\pi = (r_1, r_2, \dots, r_M)$ , which is one of the permutations of subset  $S_q$ .

with  $M$  dimensions. For all the  $M!$  possible permutations, the probability distribution  $p(\pi)$  is defined as in [99]:

$$p(\pi) = \frac{\#\{t | \leq N - (M-1)n; S_q \text{ has type } \pi\}}{N - (M-1)n} \quad (2.4)$$

where # stands for “number”. From the probability  $p(\pi)$  the permutation entropy is defined as:

$$h(P) = - \sum p(\pi) \log(p(\pi)) \quad (2.5)$$

$H(P)$  is used to denote the normalized PE, which can be expressed as:

$$H(P) = \frac{h(P)}{\log(M!)} \quad (2.6)$$

The value of the normalized  $PE$  ( $H(P)$ ) is between 0 and 1 in [100], [102]. A value of one represents a completely stochastic process, while a value of zero indicates that the time series is completely predictable. Bandt [99] has suggested that  $M$  is chosen to be between 3 and 7 for all practical cases. In Chapter 5, the evaluation of the chaos complexity is indeed done by calculating the PE value.

## 2.3 Photonic Microwave Generation

As early as the laser was invented, the idea of applying modulation to the laser's output at microwave frequencies range was introduced in the year of 1962 [103]. Since then many of the phonic microwave generation techniques were invented and extensively invested [104]–[109]. This section will introduce some of the commonly used microwave generation techniques, with emphases on the techniques using optically injected lasers.

In Figure 2.13, a simple schematic microwave photonic link with only fundamental functional blocks are presented. An input microwave signal is modulated into an optical carrier through an electrical-to-optical (E/O) converter, the resulted signal, which is the microwave in optical form, is transmitted inside of the fiber to a

remote site, then, the electrical microwave signal is recovered by the optical-to-electrical converter.

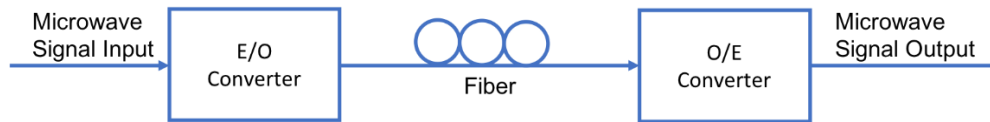


**Figure 2.13 Schematic of a simple microwave photonic link**

The microwave photonic link offers advantages over the conventional coaxial cable including low propagation loss, lightweight, electromagnetic interference (EMI) immunity, and wavelength division multiplexing capability. There are many reports on the methods microwave generation, one of the standing out technique is based on lasers period-one (P1) nonlinear dynamics, more detailed comparison between microwave generation techniques will be discussed in the sections 2.3 (page 34) below.

### 2.3.1 Microwave Generation Techniques

Many photonic microwave generations approaches can yield very low phase noise by adopting high-frequency electronic components. These commonly used techniques can be summarized as direct modulation, external modulation, optical heterodyne technique with cooperation with optical phase-lock loops (OPPLs), mode-locked semiconductor lasers, optoelectronic oscillator (OEO). The techniques that rely on electronic sources are expanded as follows:

- **Direction Modulation:** the most straightforward approach is using an electronic microwave source to apply the direct modulation on the semiconductor laser. The disadvantage of using this technique is that the modulation bandwidth is limited by the intrinsic resonance frequency of lasers and the available of high-frequency electronic microwave source. Using optical injection-locking can enhance this limit slightly [110]–[113].

- **External Modulation:** Using an external modulator to modulate the laser optical output. Those approaches introduced the electro-optic materials such as lithium niobate [114], polymers [115], [116], and the semiconductors [117].
- **Heterodyne with Optical Phase-lock Loop:** up to the sub-terahertz range frequency can be produced by heterodyning two optical components with different frequency at the detector[118]. However, to further stabilize the signal, the optical phase difference between the two optical components is tracked by using a reference frequency from a stable electronic microwave source to compare the output signal of the detector [119]. By further introducing sideband injection-locking can improve frequency stability [120], [121].

Above techniques are the ones that rely on the high-frequency electronics, which are costly and complex to implement. Thus, some of the photonic microwave generations without relying on high-frequency electronic components were also investigated. These approaches are briefly introduced as follows:

- **Self-pulsating Laser:** Self-pulsation can be invoked by exciting the relaxation resonance oscillation via the interaction between two sections in a two-section laser, the frequency is often limited to a few gigahertz [122]–[124].
- **Dual-wavelength Laser:** In a dual-wavelength laser, the two optical components are generated in the same optical cavity. Therefore, the stable microwave frequencies can be obtained by the intrinsic relation of common noise. To achieve the dual-wavelength operation, the proper seeding from independent lasers[125] or by incorporating gratings for mode-selection in fiber ring lasers can be used[61], [126].
- **Optoelectronic Oscillator:** Optoelectronic oscillator can generate very stable microwave signals using a very long fiber loop, at the same time using multiple loops to suppress the spurious noise [127], [128]. The disadvantage of using optoelectronic oscillator is that the construction requires high frequency components such as microwave filters, microwave amplifiers, photodetectors, and optical modulators. The tunability is limited by these electronics' bandwidth. Some of these electronic components can be replaced by optical components, however, by doing so, the complexity of the implementation is also increased [129]–[132].

- **Passively Mode-locked Laser:** Using passively mode-locked laser can produce monolithic photonic microwave generation with frequency over 100GHz. The limitation of this method is that the tunability is usually controlled by the fixed cavity length [133]. The microwave linewidth is typically less than 1MHz by using this method [134], [135].
- **Optically Injected Laser:** By applying an optical injection, a laser can be driven into periodic oscillation state, specifically the period-one (P1) oscillation. The laser emission intensity oscillates at a microwave frequency. Utilizing this method on VCSEL is part of the focus in this study, and it will be discussed in later chapters extensively.

Some of the photonic microwave generation techniques are excellently summaries in Ref.[136] in Table 2.1:

**Table 2.1 Comparison of Photonic Microwave Techniques**

Techniques	Electronics	Tunability	Maximum Frequency	Microwave Linewidth	Single Sideband	Modulation Type	Stability	Optical Loss
Direct Modulation	Moderate	Fair	30GHz	Source Determined	Need special design	AM	Good	None
Optical Heterodyne	Simple	Good	~THz	Broad	Yes	/	Poor	None
OPLL	Complicated	Fair	330GHz	~mHz	Yes	/	Good	None
Dual-mode Laser	Complicated	Good	42GHz	~MHz	Yes	/	Poor	None
External modulation	Moderate	Fair	40GHz	Source Determined	Need special design	AM/PM	Good	Large
Mode Locking	Moderate	Poor	30GHz	~Hz to mHz	No	/	Good	Large
OEO	Complicated	Poor	75Gz	~mHz	No	AM/PM	Good	Large
P1 Dynamics	Simple	Good	100GHz	MHz	Yes	FM	Poor	None

### 2.3.2 Period-one Oscillation for Photonic Microwave Generations

From the above discussion, it can be seen that the advantages of microwave generation based on P1 oscillation are prominent. The nonlinear dynamical P1

oscillation in optically injected semiconductor laser have been investigated for microwave generation recently [109], [137]–[148]. The P1 oscillation is one of the many nonlinear dynamics such as period-doubled, quasi-periodic, and chaotic oscillation under continuous-wave (CW) optical injection. P1 oscillation can be achieved when a stable locked laser experiences a Hopf bifurcation, which the intensity of the laser emission is oscillating at a microwave frequency [53], [139], [144]. In P1 dynamic, there are two dominant frequencies: one is generated from the optical injection while the other one is emitted near the cavity resonance frequency [141]. The frequency of photonic microwave generation based on P1 can be broadly tunable by changing the injection power or frequency detuning. The generated frequency can far exceed the relaxation oscillation frequency of the injected semiconductor laser. Photonic microwave generation based on P1 oscillation has been investigated extensively in conventional single-mode distributed feedback (DFB) laser [144], [145]. The results show that 100 GHz with a tuning range of tens of gigahertz photonic microwave signal can be achieved using P1 oscillation in DFB lasers [149]. Recently, a tunable photonic microwave with the continuous tuning of the frequency up to 20 GHz has also been achieved experimentally in a quantum dot (QD) laser based on P1 oscillation [150].

For photonic microwave generation, the nonlinear dynamical P1 oscillation offers the following advantages over other techniques:

- The microwave frequency generated from P1 oscillation can be broadly tunable, and it is far beyond the laser's relaxation resonance frequency, in some DFB lasers, the generated frequency can even be up to terahertz band [137], [145].
- The generation of the optical microwave signal can be achieved without using any electronic microwave components [136], [142].
- On optical spectra, single-sideband can be generated by adjusting the injection parameters to minimize the chromatic dispersion introduced microwave power penalty during the transmission over long optical fibers [106], [140], [147], [151].
- Maximal microwave power at a constant average optical power can be produced because of nearly 100% intensity modulation depth [138], [147].
- Can use both modulating the laser's bias current electrically or injection optically to apply the data modulation on the microwave signal [138], [152].

Due to the listed advantages above, the P1 oscillation is implemented into a number of applications such as radio-over-fiber (RoF) [138], clock frequency division[153], [154], modulation formation conversion[140], [149], uplink transmission[151], [152], long-detection-range Doppler velocimeter[149], and photonic microwave amplification[147].

Despite many of the advantages, the P1 oscillation is not without its limitations. The P1 oscillation dynamics characteristically contains phase noise due to the fluctuations in the lasers. This phase noise causes performance issues in many applications: in communication links, the reduction of signal-to-noise ratio[138], reduction on the maximal detection range in Doppler velocimeters [155], and the degradations of the noise performance in photonic microwave amplification [147]. Thus, there are some techniques developed to reduce the phase noise. In DFB lasers, locking the P1 oscillation using a stable electronic microwave source were introduced in the year 1999, the which the generated microwave signal frequency is up to  $17\text{GHz}$  and its linewidth is below  $1\text{kHz}$  [156]. Self-injection locking using optoelectronic feedback also narrowed the microwave signal linewidth to about  $10\text{kHz}$  [105], however, this approach requires high-speed microwave amplifiers for the electric feedback. Polarization rotated feedback with optoelectronic feedback were also reported, it reduced the linewidth to about  $3\text{kHz}$  for a P1 oscillation generated microwave at  $6\text{GHz}$  [142], the imperfection of this method is that the tunability is restricted by the electronic circuitries. The optical feedback were introduced to reduce the microwave linewidth, which, providing comparable linewidth reduction without adding extra electrical components and has no restrictions on the tunability [58], [157]. In Chapter 4, period-one oscillation generated microwave in VCSELs using the similar techniques is investigated and applied.



## 3 Photonic Microwave Generation in an Optically Injected VCSEL

### 3.1 Chapter Introduction

In earlier sections, it is mentioned that the photonic microwave generation based on period-one oscillation in the different type of lasers have various degrees of success. In this chapter, such method is extended in an off-the-shelf VCSEL. The photonic microwave signal generation using single-mode VCSELs in order to achieve the low cost and low power consumption of tunable photonic microwave is experimentally and theoretically investigated.

The remainder of the chapter is organized as follows: the chapter starts by showing the experimental setup and method of data acquisition in Section 3.2, the experimental results are presented in Section 3.3, then we introduced the simulation model in Section 3.4, followed by the numerical simulation results in Section 3.5. Section 3.6 summarizes the chapter.

### 3.2 Experimental Setup and Data Acquisition

During the experiment, not only many of the control variables or parameters are frequently changed, but also the large sequences of data need to be recorded. The processes to generated mapping results that can be systematically analyzed. These processes are time consuming and repetitive. Thus, we used a system-design platform software from National Instruments named LabVIEW to create a semi-automatic parameters control and data collection environment.

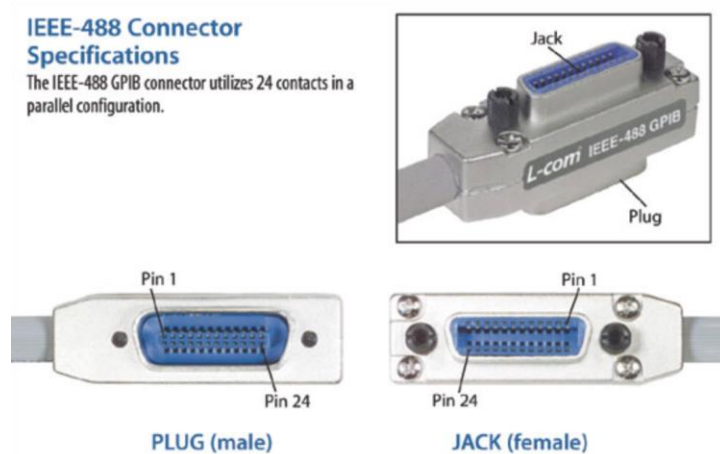


**Figure 3.1 IEEE-488 (GPIB) Cable/Connector Characteristics (Photo credit: Infinite Electronics International)**

Most of our instruments have a 25-pin General Purpose Interface Bus (GPIB also called IEEE-488) port (presented in Figure 3.1) or an Ethernet which can be connected together along with a PC in parallel multi-master connection. Some single purpose instruments such as digital optical attenuator and optical power meter accept or respond commands written in the BASIC language. Other more advanced instruments, for example, OSA, ESA, OSC, have proprietary drivers installed in order to be recognized by the LabVIEW.

### 3.2.1 Experimental Setup for Laser Characterization

In Figure 3.2 the experimental setup for laser characterization is presented. Due to having more than one polarization direction in VCSEL, the polarization controller is added with a combination of polarization beam splitter enables the ability to record the data for both polarization directions.

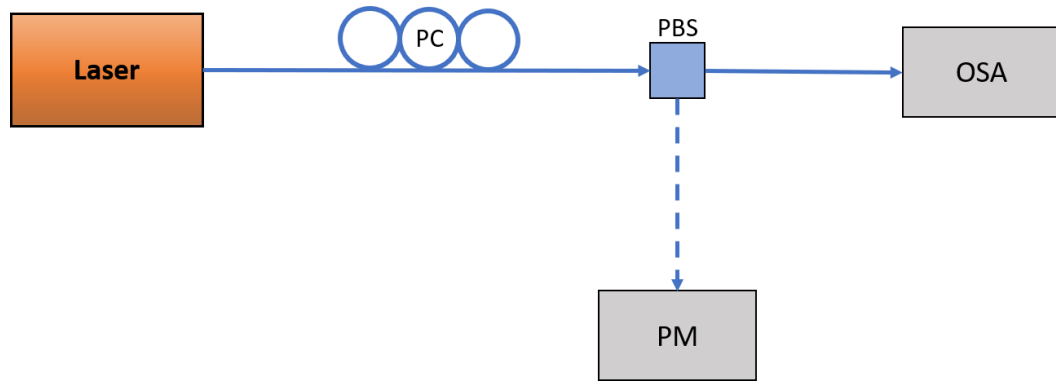
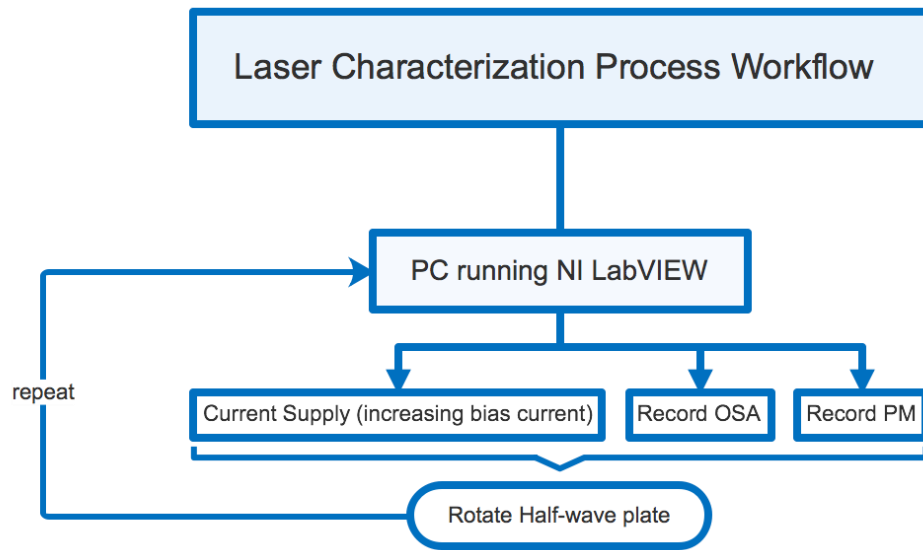


**Figure 3.2 Experimental setup for laser characterization in fiber setup. PC: Polarization Controller, PBS: polarization beam splitter, OSA: optical spectrum analyzer, PM: power meter.**

Because of the nature of VCSELs, under free running, VCSELs normally lase at one linear polarization at the threshold current. The polarization direction at the threshold current in this thesis is defined as y-polarization, its orthogonal polarization direction will be the x-polarization.

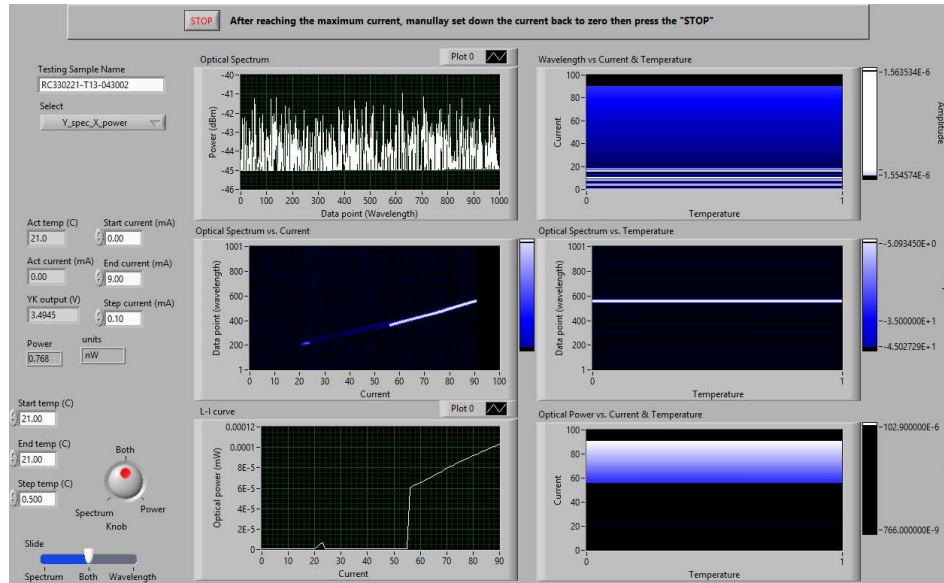
The LabVIEW workflow is illustrated in Figure 3.3. We first use polarization controller to control the polarization direction inside of fiber aligns the PBS direction, so that after the PBS, the laser at the threshold current have the maximum throughput to the OSA. Slowly increase the bias current with a step size of 0.1mA using LabVIEW to send the command to the current source, and then store the OSA and PM data to the computer for each step of bias current. Keep increasing the bias current until it reaches the designed maximum allowed bias current.

During this bias current increase process, the VCSEL we used may have one or more polarization switching points, at the switching bias current, the polarization direction will switch to its orthogonal polarization direction. For example, at the first polarization switching point, the polarization direction will switch to x-polarization, which the PBS will direct the most optical power to the PM instead of the OSA fiber path.



**Figure 3.3 Laser characterization workflow utilizing LabVIEW. OSA: Optical Spectrum Analyzer. PM: Power Meter.**

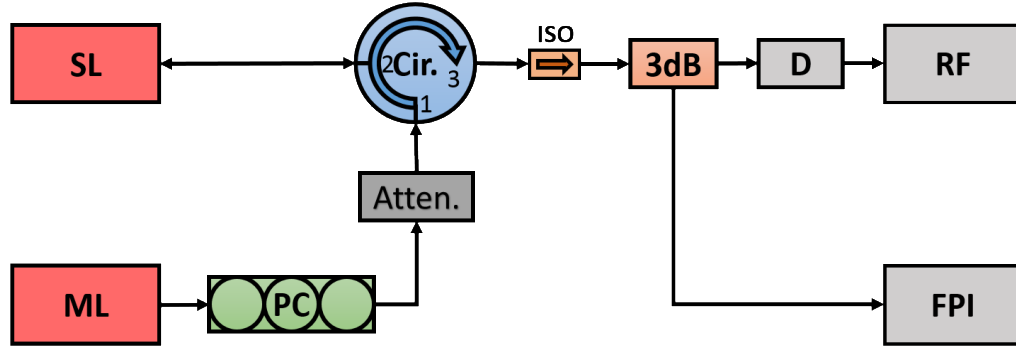
Figure 3.4 shows the front control panel of the laser characterize LabVIEW program. The left three graphs are the current optical spectrum captured by the OSA at current bias current, the lasing wavelength versus bias current and the L-I curve, from the top to bottom. Right three graphs are related to the temperature, which are disabled and ignored as we keep the temperature constant in our experiment.



**Figure 3.4 LabVIEW interface for the laser characterize experiment.**

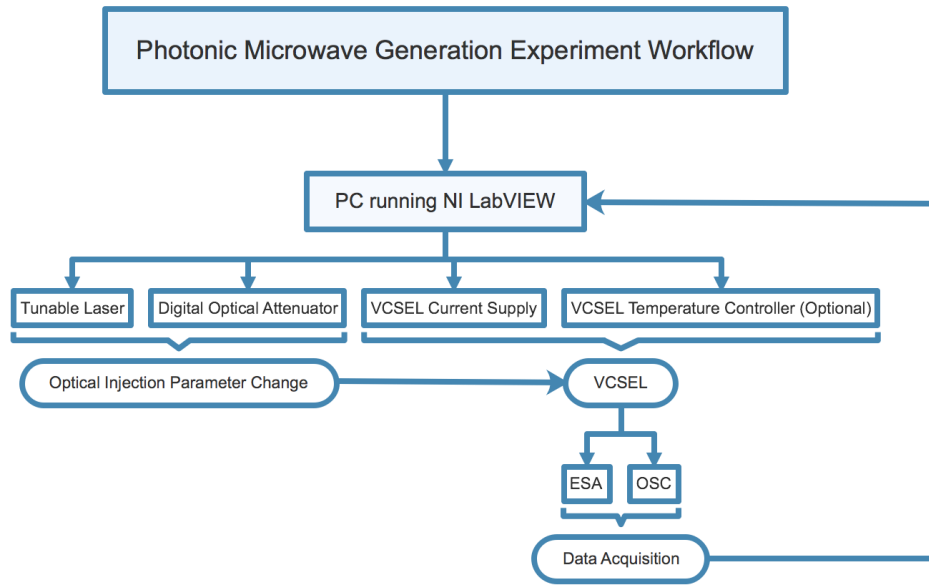
### 3.2.2 Experimental Setup for Photonic Microwave Generation

Figure 3.5 shows the setup using single-mode semiconductor laser in the master-slave configuration. The slave laser is a commercial VCSEL (RayCan RC33xxx1F) packaged with a fiber pigtail. It is biased 8.5mA and it is temperature-stabilized at 21°C. When free-running, the VCSEL emits around 0.5mW of power at an optical wavelength of 1529.92nm. The master laser (ML) is a tunable laser (TUNICS-BT 1550) that emits continuous wave light between 1560nm to 1640nm with a maximum output power of 10mW and 1MHz of linewidth.



**Figure 3.5 The experimental setup. ML: Master laser, SL: Slave laser, PC: polarization controller, Atten: digital attenuator Cir: Optical circulator. ISO: optical isolator, 3dB: 2 by 2 3dB fiber coupler, Dec: photodetector, RF: radio frequency spectrum analyzer. FPI: Fabry-Perot interferometer.**

The output of the master laser delivers through a polarization controller (PC), a digital fiber attenuator and an optical circulator, and inject into the slave laser (SL) VCSEL. The polarization controller is used to control the polarization of the injection beam to be parallel to the free-running VCSEL's lasing polarization direction. The injection power in the fiber pigtail is measure just before the injection beam enters the VCSEL and it is denoted as  $P_i$ , the frequency detuning  $f_i$  is calculated as the master laser's frequency minus the free-running lasing frequency. The injection parameter ( $f_i, P_i$ ) can be controlled by the master laser and digital attenuator. The emission of the slave laser split by an 50:50 fiber coupler into two paths. One path is detected by 12GHz bandwidth photo-detectors (New Focus 1554-B) and recorded by a 30GHz RF spectrum analyzer (Anritsu MS 2667C); another path was sent to a Fabry-Perot interferometer (FPI). The output beam from the FPI was detected by a detector and sent to an oscilloscope (Tektronix TDS7404) for monitoring the optical spectra of the SL. The finesse of the FPI is 150 and the free spectrum range of the FPI was set at 19.9GHz, which resulting in the resolution of the FPI up to 0.133GHz. In this experiment, no polarization-resolved VCSEL's output was measured, all fibers are fixed in the setup to minimize the polarization direction fluctuations inside the fiber. In the experiment, the bias current was fixed at 8.5mA, unless stated elsewhere.



**Figure 3.6 Automatic data acquisition workflow for photonic microwave generation utilizing LabVIEW. ESA: Electrical Spectrum Analyzer. OSC: Digital Oscilloscope.**

The mapping data collection is mostly done by utilizing the LabVIEW environment; the workflow is presented in Figure 3.6, the PC sends a command to set one injection frequency  $f_i$  first, then sweep the injection power  $P_i$  by sending control to the digital optical attenuator. The received data will be sent back to PC for analyze. When it finishes the  $P_i$  sweeping process, the PC will then send the next  $f_i$  to the tunable laser to start a new  $P_i$  sweeping process. The reason we chose optical attenuator to adjust the injection power is that the tunable laser we used changes its output power slightly with the change of its wavelength. This may have an impact on the experimental result.

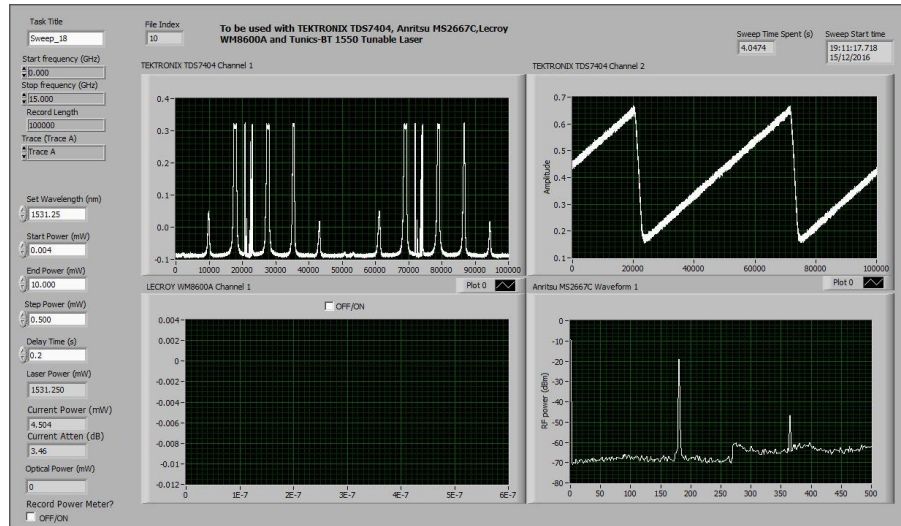


**Figure 3.7 LabVIEW interface for the photonic microwave generation experiment.**

The capturing interface for the microwave generation experiment is presented in Figure 3.7. In this figure, the top left panel is the optical spectrum captured from the FPI. The top right panel is Piezo driven voltage of the FPI. The bottom left panel is a channel input from a different oscilloscope (not used in this experiment). The bottom right panel is the VCSEL's power spectrum obtained from the RF analyzer.

## 3.3 Experimental Results

### 3.3.1 Characterization

Each individual VCSEL will have slightly different characterizations even they were produced on the same wafer. These differences include the threshold current difference, lasing wavelength difference at different bias current and temperature, lasing modes difference and so on. Therefore, the characterization process before the further experimental investigation is necessary. The VCSEL used in the experiment was a single transverse mode laser, the temperature of the VCSEL is fixed at 21°C. In order to obtain the lasing wavelength of this VCSEL under different bias current, in Figure 3.8, the bias current is increased from 0mA to 10mA with the step of 0.1mA. A half-



wave plate and a polarization beam splitter were used to exam its polarization switching. The blue line represents the optical power measured on Y-polarization, the yellow line represents the emission power on X-polarization. VCSEL first start lasing at one polarization (Y-polarization) near the threshold current. When the bias current was increased to  $3.1\text{mA}$ , the polarization switched to its orthogonal polarization (X-polarization). Further increases in the bias current to  $6.7\text{mA}$ , see the polarization switch back to Y-polarization and remained in this polarization until the bias current reached  $9.3\text{mA}$ . The frequency of Y-polarization is about  $5.1\text{GHz}$  higher than that of X-polarization at each polarization switching point. In Figure 3.8, adding up the optical power for x and y polarization state should match the total output power in theory, however, due to the extra added optical components for examining the individual polarization, measured optical power for each polarization is much less than the total output power.

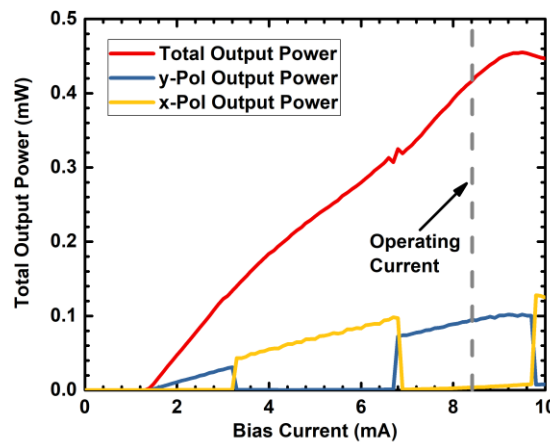


**Figure 3.8 Characterization of the VCSEL used in Chapter 3. Red line is representing the total optical power, blue line and yellow line represent the optical power of Y-polarisation and X-polarisation, respectively**

Similar to DFB lasers, the increase of the VCSEL's bias current will also increase the laser's lasing wavelength. The optical spectrum information at different bias current captured by the optical spectrum analyzer is presented in Figure 3.9. In Figure 3.9 the horizontal axis is the bias current and the vertical axis is the wavelength. The color bar stands for the optical power at the corresponding wavelength. From the figure we can observe that the VCSEL starts lasing at around bias current of  $1.3\text{mA}$ , we

can also clearly see the lasing wavelength switching at the bias currents of 3.1 mA, 6.7mA and 9.3 mA, which corresponds to the polarization switching. Fig. 3.9 also shows that the original polarization mode still lasing with a weak optical power after the polarization switching.

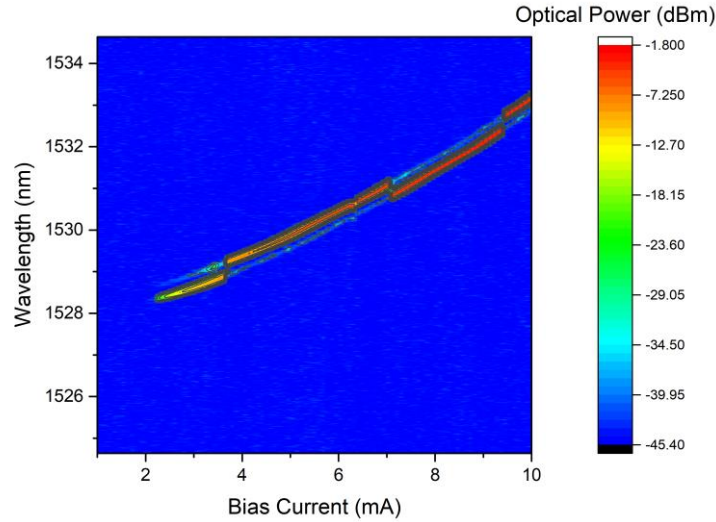


**Figure 3.9 Optical Spectrum Information at different bias current.**

### 3.3.2 Fundamental Frequency of the generated Photonic Microwave

In the experiment, the bias current of the VCSEL is fixed at 8.5mA, unless stated elsewhere. The injection power was varied from  $0.0007mW$  to  $1.86mW$  and the frequency detuning was varied from  $-14.37GHz$  to  $+13.32GHz$ . The injection power was measure at port 2 of the optical circulator and the output power of the free running VCSEL was found to be  $1.70mW$ . The actual injection powers in the VCSEL were smaller than the measurement due to coupling loss. However, the quantity analysis on the effect of the injection power on the frequency of the generated photonic microwave is out of the scope of this study, thus, the relative analysis is provided here. The frequency detuning  $f_i$  is defined as the  $f_{ML} - f_{SL}$  where the  $f_{ML}$  and  $f_{SL}$  are the frequencies of the master laser and the slave laser. Figure 3.10 shows the RF spectrum

of the VCSEL at several injection conditions under P1 oscillation. In Figure 3.10(a), the red color indicates the RF signal, and grey color is the noise floor, we can observe a noise floor increased rapidly at 8GHz and above. This is because the RF spectrum analyzer uses different harmonic orders of the mixer for different frequency ranges. For the 0 to 8.1GHz frequency range, the first harmonic order of the mixer has been used; for 8.0 to 15.3GHz frequency range, the second harmonic order of the mixer has been used, which resulting in a higher noise floor in this range. Figure 3.10(a) shows the spectrum of the VCSEL under injection condition  $(f_i, P_i) = (-2.9GHz, 0.37mW)$ , under this injection condition, the VCSEL is in P1 oscillation state with a fundamental frequency  $f_0$  of 5.87GHz. The optical spectrum of P1 oscillation in optical injection VCSEL contains a regenerative component at injection frequency  $f_i$  and sidebands equally separated by the fundamental frequency of photonic microwave  $f_0$  [136]. The beating between the regenerated mode and the second strongest sideband induces the second harmonic at  $2f_0$ , which has also been observed with power suppression of 20dB in comparison with that at the fundamental frequency. Under the same frequency detuning, increasing the injection power to 0.74mW, see the generated microwave frequency increase to 7.22GHz, as shown in Figure 3.10(b), which demonstrates that the injection power affects the fundamental frequency of the generated photonic microwave.

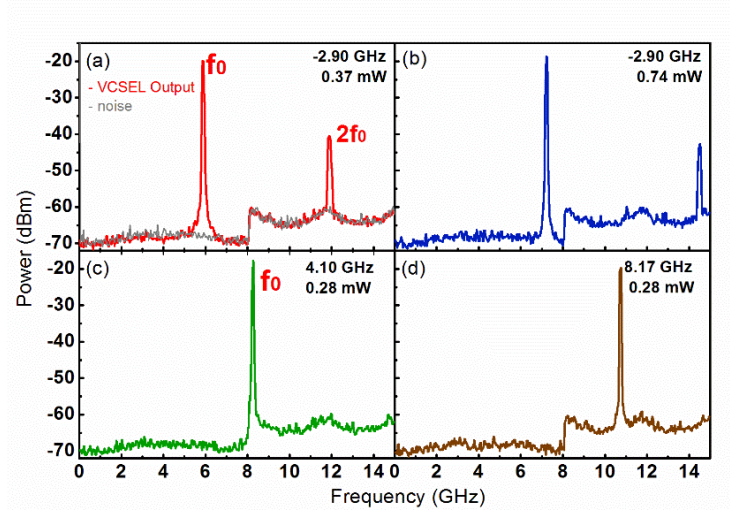


**Figure 3.10 Power spectra of the VCSEL output at injection condition ( $f_i, P_i$ ) of (a)  $(-2.9\text{GHz}, 0.37\text{mW})$ , (b)  $(-2.9\text{GHz}, 0.74\text{mW})$ , (c)  $(4.1\text{GHz}, 0.28\text{mW})$ , (d)  $(8.17\text{GHz}, 0.28\text{mW})$ .**

To observe the effect of frequency detuning on the fundamental frequency, we fixed the injection power and varied the frequency detuning. Figure 3.10(c)-(d) show the power spectra of the VCSEL with injection power of  $0.28\text{mW}$  and the frequency detuning of  $4.1\text{GHz}$  and  $8.17\text{GHz}$ , respectively. In Figure 3.10(c),  $8.26\text{GHz}$  of the fundamental frequency has been observed. At this operating parameters, we believe the second harmonic appeared at around  $16.5\text{GHz}$ , however, due to the detector bandwidth limitation, this second harmonic peak cannot be detected. Increasing the frequency detuning to  $8.17\text{GHz}$ , as shown in Figure 3.10(d), the fundamental frequency increased to  $10.74\text{GHz}$ , which also indicate the fundamental frequency related to the frequency detuning in this P1 region.

The generated microwave fundamental frequency,  $f_0$ , variation as a function of frequency detuning under two different injection power is plotted in Figure 3.11(a). The gap between the data lines are mostly injection locking (IL) with small P2 and chaos oscillation region. The VCSEL operated above Hopf bifurcation boundary for the curves at the right side of the gap and below saddle-node bifurcation boundary for the curves at the left side of the gap. When the injection power is small (black lines,

injection power of  $0.093mW$ ), the frequency shift rate of  $f_0$  is higher in the negative frequency detuning. Increasing the injection power to  $0.558mW$ , causes the injection locking to shift to a more negative frequency detuning region. The results also show that the frequency shift rate for the injection power of  $0.558mW$  is lower than that for the injection power of  $0.093mW$  for the detuning frequencies above the Hopf bifurcation boundary.

Figure 3.11(b) displays the fundamental frequency  $f_0$  as a function of the injection power with four fixed detuning frequencies. The results show that the frequencies  $f_0$  increase monotonically with the increasing injection power. For lower injection powers ( $< 0.5mW$ ), the frequency shift rates are varied for the different frequency detuning. The frequency shift rates decreases with increasing frequency detuning. For the higher injection powers ( $> 0.5mW$ ), the frequency shift rates are approximately constant for all detuning frequencies. This result is similar to the that reported in DFB laser based configurations [106].

The same physical mechanism in Ref.[106] can be used to explain the results. The fundamental microwave frequency is the result of the frequency beating between the injection beam and the cavity frequency. When the VCSEL is subjected to optical injection, the cavity frequency experiences a redshift due to the increase of the refractive index and the pulling effect. The competition between the red-shifting and pulling effect induces the frequency shift rate change under different injection power and detuning frequency conditions.

To further study the generated microwave frequency under different injection conditions, a map of the generated microwave frequency for various detuning frequencies and injection powers is presented in Figure 3.12; the two rainbow-color denoted areas that exhibit period one dynamics. Injection locking, period-two, and chaotic regions are embedded within the large grey area, which is not our focus in this section. In the upper right corner of the black color areas, the oscillation frequencies are found to be outside of the measurement range of the instrumentation. The results in Figure 3.12 indicate that the frequency detuning and the injection power significantly affect the frequency of photonic microwave. The frequency of photonic microwave

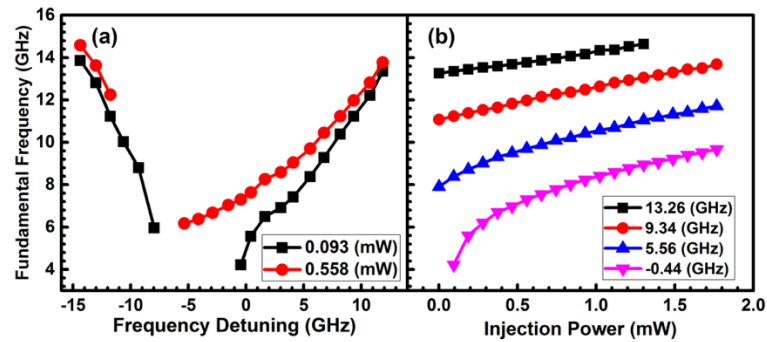


**Figure 3.11 Generated microwave frequency as function of (a) frequency detuning and (b) injection power.**

signal increases with the increase of injection power, the frequency detuning above the Hopf bifurcation boundary and the absolute frequency detuning below the saddle-node bifurcation boundary. The continuous tuning of the frequency from 4GHz to up to 15GHz (due to the instruments limitation) has been obtained.

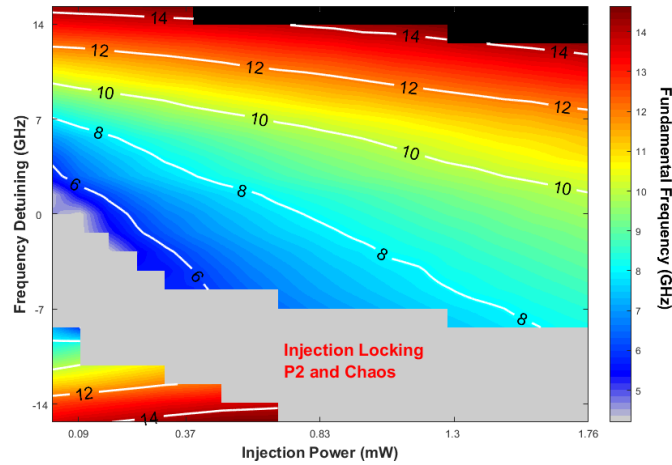


**Figure 3.12 Mapping of the fundamental frequency  $f_0$ .**

### 3.3.3 Microwave Power Measurement

At the photo-detector, the optical frequency components are converted into microwave signal. To utilize photonics generated microwave in RoF applications, it is essential to understand how the power of the generated microwave varies with injection power and frequency detuning. As shown in Figure 3.10(a)-(b), the fundamental frequency  $f_0$  and the second harmonic  $2f_0$  can be observed at the same time, the power at  $f_0$  and  $2f_0$  are denoted  $P_{f_0}$  and  $P_{2f_0}$  respectively. Figure 3.13 maps the power  $P_{f_0}$  at the fundamental frequency with the same injection conditions as those in Figure 3.12. Similarly, in Figure 3.13, the top right black area is out of our instrument detection range, the grey area is mainly the injection locking region and small P2 and Chaos regions. From the mapping, we can observe that the microwave power stays around  $-25\text{dBm}$  consistently over the whole frequency detuning range with P1 dynamics when injection power is below  $0.2\text{mW}$ . Above injection powers of  $0.2\text{mW}$ , the microwave  $P_{f_0}$  increases to a power of around  $-20\text{dBm}$  except in two areas (indicated with red color). The power in these two areas is approximate  $4\text{dB}$  higher than in the adjacent regions. These two areas have not been observed lasers in DFB [106] or quantum dot lasers [150]. In our co-author published theoretical study [158], we explained that these two maximum microwave powers appear because of the out-of-phase excitation with small amplitudes of both linear polarizations of the VCSEL for frequency detuning between the values at which the two maxima appear.

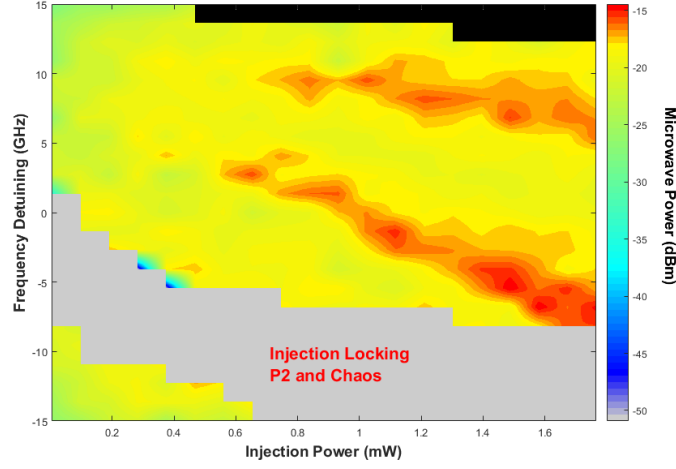


**Figure 3.13 Mapping of the fundamental microwave frequency power  $P_{f0}$ .**

In this experiment, we also characterize the second harmonic distortion (SHD) in the RF spectra of the generated microwave. The SHD in this section is defined as the ratio of the second harmonic power  $P_{2f0}$  to the power at the fundamental frequency  $P_{f0}$  [150]. The SHD of the optically injected VCSEL is presented in Figure 3.14. The frequency detuning range in this measurement is from  $-6GHz$  to  $4GHz$ , which is smaller than those measurements for the microwave frequency. The reason is that the second harmonic peak is out of the detection range of the detector for the higher frequency detuning. Figure 3.14(a) shows that the SHD fluctuates around  $-27dB$  for the injection power of  $0.093mW$ . No trend with the frequency detuning can be concluded. However, the SHD shows a tendency to decrease with the increasing frequency detuning within the measurement range for the injection powers of  $0.279mW$  and  $0.465mW$ . These results have some similarity with the results in quantum dot laser [150], where the SHD is less sensitive to frequency detuning for low injection power. For intermedium injection powers, the maximum SHD was observed in the intermediate frequency detuning range in QD laser [150], however, this phenomenon has not been seen in our experiment. Figure 3.14(b) shows the SHD as a function of the injection power with three different detuning frequencies. The results show that the SHDs changes irregularly with the increasing injection power. No simple



trend is observed. The weaker dependence of the SHD on the injection power seen in our experiment is similar to that reported in QD laser [150]. Lower amplitude fluctuations were observed at the most negative detuning frequency among these three detuning frequencies.

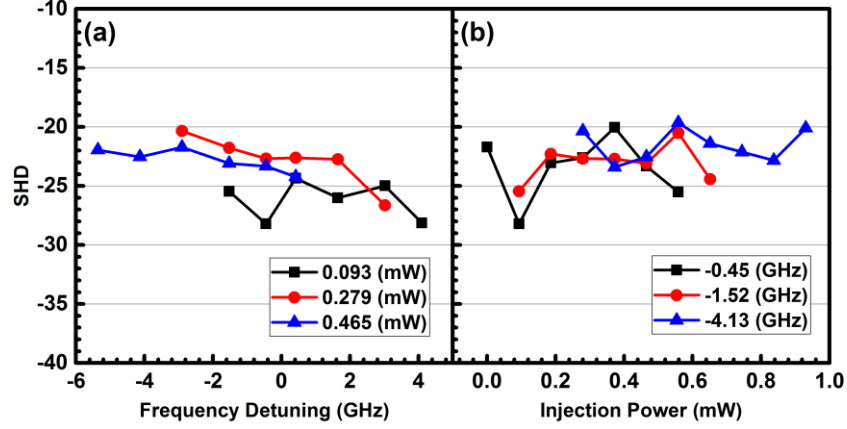


**Figure 3.14** Second harmonic distortion as a function of (a) the frequency detuning, (b) the injection power.

### 3.4 Simulation Model

Our theoretical analysis is based on the spin-flip model that describes the dynamical of the polarization modes of a single-transverse mode VCSEL. Generally, the dynamic of a VCSEL can be described by four variables in the rate equation; these variables are the complex electric field  $E$  on x polarization direction, complex electric field  $E$  on y-polarization direction, the total carrier density  $N$  and difference between the carrier densities with opposite spin value  $n$ .

$$\begin{aligned} \frac{dE_x}{dt} = & \kappa(1 + i\alpha)(NE_x - E_x + inE_y) \\ & - (\gamma_a + i\gamma_p)E_x + \eta_x E_{inj} e^{i2\pi(v_{inj} - \nu)t} + F_x \end{aligned} \quad (3.1)$$

$$\frac{dE_y}{dt} = \kappa(1 + i\alpha)(NE_y - E_y - inE_x) \quad (3.2)$$

$$+(\gamma_a + i\gamma_p)E_y + \eta_y E_{inj} e^{i2\pi(\nu_{inj} - \nu)t} + F_y$$

$$\frac{dN}{dt} = -\gamma_e N (1 + |E_x|^2 + |E_y|^2) + \mu\gamma_e - i\gamma_e n(E_y E_x^* - E_x E_y^*) \quad (3.3)$$

$$\frac{dn}{dt} = -\gamma_s n - \gamma_e n (|E_x|^2 + |E_y|^2) - \gamma_e N(E_y E_x^* - E_x E_y^*) \quad (3.4)$$

In the rate equations (3.1) (3.2) (3.3) (3.4) above, the subscripts  $x$  and  $y$  stand for the  $X$  and  $Y$  polarizations of the VCSEL, respectively.  $\alpha$  is the linewidth enhancement factor;  $\gamma_a$  is the linear dichroism;  $\gamma_p$  is the linear birefringence;  $\gamma_e$  is the decay rate of the total carrier population;  $n$  is the difference between the carrier densities with opposite spin values;  $k$  is the field decay rate;  $\gamma_s$  is the spin-flip rate;  $\eta_x$  and  $\eta_y$  are the injection strength into the  $X$ ,  $Y$  polarization direction;  $E_{inj}$  is the injection field amplitude.  $\nu$  is the central frequency of the free running VCSEL,  $\nu = (\nu_x + \nu_y)/2$ , where  $\nu_x$  and  $\nu_y$  are the frequency of the VCSEL's  $X$ ,  $Y$  polarization components.  $\nu_{inj}$  is the injection frequency;  $\mu$  is the normalized bias current.

In semiconductor laser operation, spontaneous emission is one of the intrinsic noise sources[159]. Spontaneous emission is different from other fluctuations such as the bias current and temperature; it is fundamentally induced in the laser. The spontaneous emission noise can be modeled by the Langevin noise force in the rate equations in [29], [160].  $F_x$  and  $F_y$  are the Langevin fluctuating noise on  $x$  polarization and  $y$  polarization, respectively. The term  $F_x$  and  $F_y$  are defined as:

$$F_x = \sqrt{\frac{\beta_{sp}}{2}} (\sqrt{N + n}\xi_1 + \sqrt{N - n}\xi_2) \quad (3.5)$$

$$F_y = -i \sqrt{\frac{\beta_{sp}}{2}} (\sqrt{N + n}\xi_1 - \sqrt{N - n}\xi_2) \quad (3.6)$$

$\xi_1$  and  $\xi_2$  are the independent Gaussian white noise sources with zero mean and unit variance,  $\beta_{sp}$  is the noise strength. In this chapter, we chose a small noise strength value to exclude the noise effect to the overall dynamics.

In this section, the typical VCSEL simulation parameters are used, they are listed in Table 3.1 unless stated otherwise.

**Table 3.1 Values used for simulation**

Parameter	Symbol	Value
linewidth enhancement factor	$\alpha$	3
linear dichroism	$\gamma_a$	$3ns^{-1}$
linear birefringence	$\gamma_p$	$94.3ns^{-1}$
decay rate of the total carrier population	$\gamma_e$	$0.67ns^{-1}$
spin-flip rate	$\gamma_s$	$140ns^{-1}$
field decay rate	$k$	$125ns^{-1}$
injection field amplitude	$E_{inj}$	1
noise strength	$\beta_{sp}$	$4e^{-4}$

The numerical integration has a time step of  $1ps$  and it is carried over a time span of  $300ns$ . Longer time span enables higher spectral resolution; however, these numbers are well enough to provide an accurate result for the purpose of this chapter.

## 3.5 Numerical Results

### 3.5.1 L-I curve

Figure 3.15 shows the L-I curve of the simulated VCSEL. We increased the bias current up to 10 times of the threshold current with the step size of 0.1 times. Under these parameters, the polarization switching did not occur, the VCSEL stayed emitting in y-polarization direction.

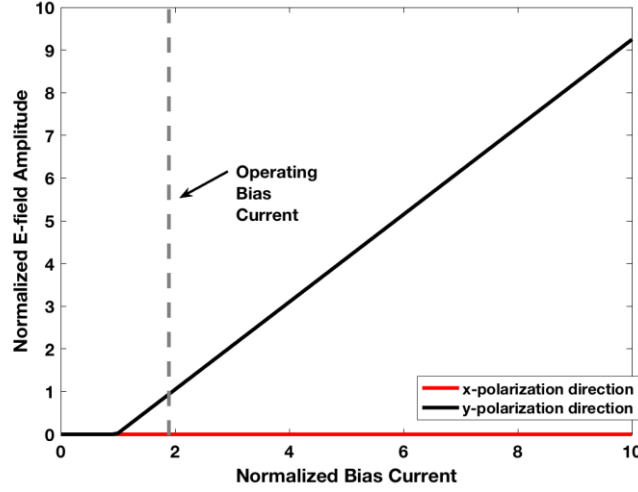


**Figure 3.15 Simulated L-I curve of the VCSEL using the parameter listed in Table 3.1.**

### 3.5.2 Dynamic state evolution

In this section, we consider parallel optical injection in which the direction of the linearly polarized optical injection coincides with that of the linear polarization (y) in which the free-running VCSEL emits, therefore,  $\eta_x = 0$ . The optical spectrum and power spectrum of the slave laser emission are obtained by applying the Fourier transformation on  $E_x(t) + E_y(t)$  and  $|E_x(t)|^2 + |E_y(t)|^2$  respectively. The optical spectrum directly corresponds to the slave laser emission light, whereas, the power spectrum corresponds to the microwave came out of the photodetector. The injection frequency detuning is kept at  $\nu_{inj} = 6GHz$ , and the injection strength on the y-polarization direction  $\eta_y$  is varied to drive the slave laser VCSEL into the different dynamic state. The evolution of the optical spectra, which are offset at the free running VCSEL's lasing frequency as shown in Figure 3.16 without added noise term. In Figure 3.16(a), the injection strength  $\eta_y = 70GHz$  is strong and it is able to pull the slave laser into the ML frequency. At this injection strength, the VCSEL is locked at  $\nu_{inj}$  stably. Decreasing the injection strength to  $\eta_y = 22GHz$  in Figure 3.16(b) puts the laser output above the Hopf bifurcation line (visible in Figure 3.18 indicated with white dash lines)

and enters the period one (P1) state. The optical spectrum consists of components that is separated from  $f_i$  in multiples of  $f_0$ . The major components are  $f_i$  and  $f_c$ , which  $f_c = f_i - f_0$ . The next strong components appeared at  $2f_0$  away from  $f_i$  location, the cavity frequency  $f_c$  is surrounded by two equally strong sidebands. This situation is referred to double sideband (DSB) P1 oscillation. This major optical component  $f_c$  start red-shifting to  $-1.96GHz$  position. Combining the red shift effect and the pulling effect from the injection, it causes VCSEL output in oscillation at a microwave frequency of  $f_0$  of  $7.96GHz$ . In Figure 3.16(c), the injection strength is reduced to  $\eta_y = 1.2GHz$ , the red shift reduced to  $-1.42GHz$ , at this situation the fundamental frequency also reduced to  $f_0 = 7.42GHz$ . In Figure 3.16(c), the microwave oscillation has a sideband rejection ratio (the ratio of side band power to the dominant frequency power) of  $25dB$ , therefore, the signal is approximately single sideband (SSB) in this state (commonly, sideband rejection ratio higher than  $20dB$  can be practically regarded as SSB). This SSB nature of the optical signal is highly desirable for minimizing the fiber dispersion-induced power penalty of the microwave signals in the transmission.

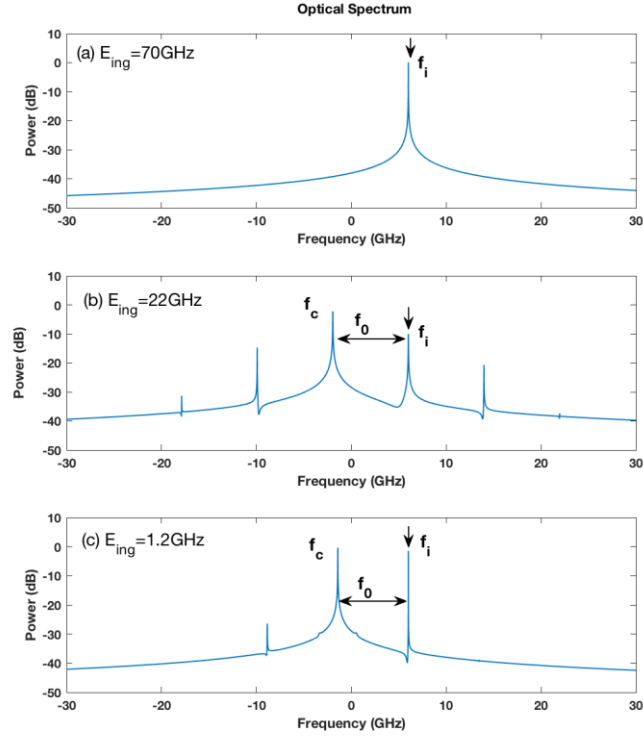


**Figure 3.16** Optical spectra with the frequency offset of the free-running slave laser frequency. The injection frequency detuning is kept constant at  $\nu_{\text{inj}} = 6 \text{ GHz}$  which is highlighted by the arrows. The injection strength  $\eta_y$  is varied to obtain different states: (a) stable locking; (b) DSB period-one; and (c) SSB period-one.

### 3.5.3 Bifurcation in VCSEL Subject to Parallel Injection

In this section, we investigate one of the bifurcation scenarios that are most representative of different dynamic states. In Figure 3.17, the extrema of the intensities are plotted versus the injection strength  $\eta_y$ , while the frequency detuning is fixed at  $\nu_{\text{inj}} = 6 \text{ GHz}$ . The extrema are obtained by extracting the maxima and minima of the intensity times series. The bifurcation diagram is very helpful to visualize the transitions between the different dynamical states of the optically injected VCSEL. By having just 2 extremes, the zone#1 and zone#3 are recognized as a period-one dynamical state, the

zone#2 corresponds to the injection strength from  $11.5\text{GHz}$  to  $15.2\text{GHz}$ , in this zone the P2 oscillation, chaotic oscillations, quasi-periodic and other complex dynamical states are visible. Finally, in zone#4 the VCSEL enters the stable injection locking state, which there is no extreme found in the time series.

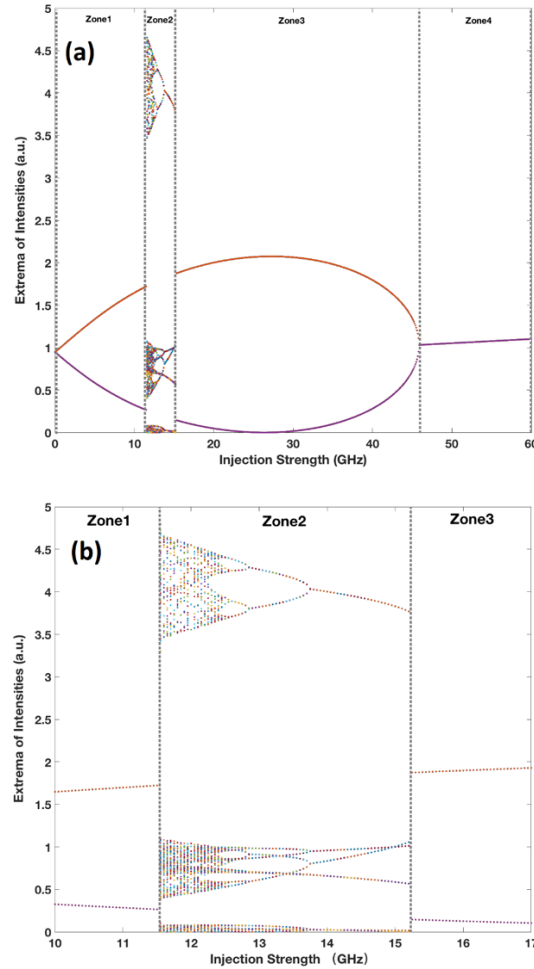


**Figure 3.17 (a) Bifurcation diagram of the intensity extrema versus the injection strength. (b) The same diagram zoomed in at Zone#2.**

### 3.5.4 Dynamical States Mapping of the Parallel Optical Injection VCSEL

Figure 3.18 is a mapping of observed dynamics based on the interpretation of the optical spectra and the bifurcation diagrams above. Large light purple shade is representing the P1 dynamical state. The red region is the chaotic oscillation state, which only occupies a small region. Surrounding the chaos region is the P2 and other more complexed dynamical states. The large deep blue region is the region for stable injection locking. White dash lines are the boundary between the P1 state and the injection locking state, which is also named Hopf bifurcation boundary.

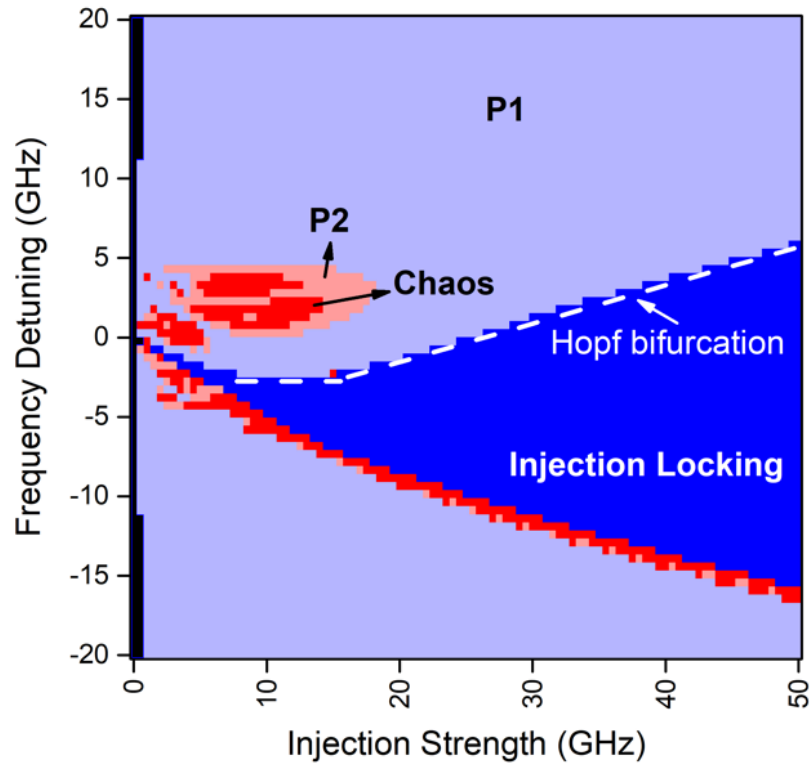


**Figure 3.18 Non-linear dynamical states mapping of optically injected VCSEL under varied injection conditions.**

In the line-shaped black area at the left part of the mapping, the VCSEL output is very close to free running state due to the weak injection strength in this region. These dynamical states have been demonstrated for a variety of applications. The simple stable locking state has been researched for bandwidth enhancement and noise suppression for DFB lasers[113], [161]. The complex state of chaos has been widely investigated in



secure communication, chaotic lidar and random bit generator [47], [52], [57], [92], [162]. Finally the P1 dynamical state has been intensively demonstrated for tunable photonic microwave generation and radio-over-fiber communications for DFB lasers [106], [147], [151], [163], [164] and for VCSELs [141], [146], [165]–[168].

### 3.5.5 Microwave Frequency

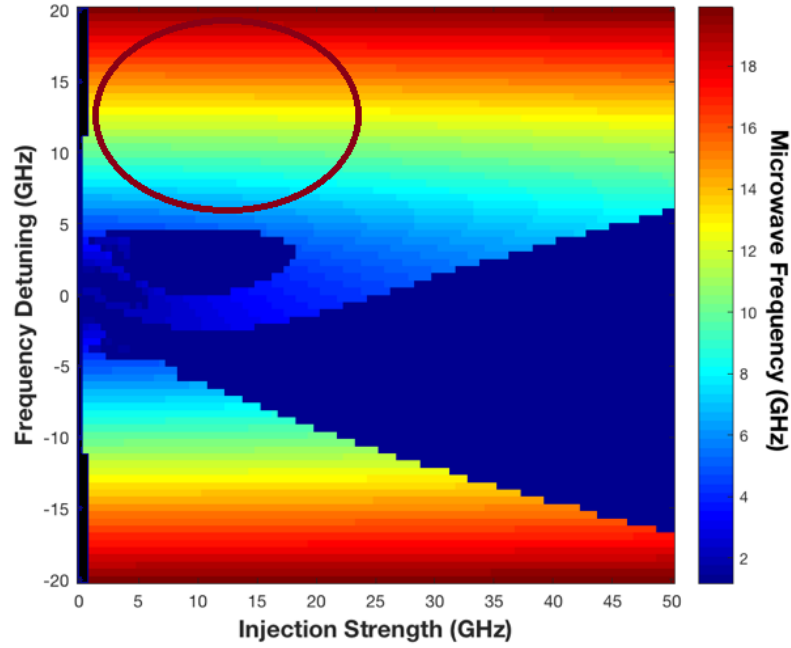


**Figure 3.19 Mapping of the fundamental frequency.**

A map of the generated microwave frequency  $f_0$  under different injection conditions is presented in Figure 3.19. The rainbow color (except the dark blue part) areas indicate that the VCSEL is exhibiting period one dynamics. The  $\eta_y$  is increased by a step of 1GHz, and the frequency detuning is increased by every 0.5GHz. From the mapping, it is shown that the microwave frequency is continuously tuned up to more than 20GHz by adjusting the frequency detuning. When  $\eta_y$  is near zero, the slave laser is undisturbed free running optical frequency, observable with the area at the very left side, there is no microwave frequency generated in this area possibly due to the extremely weak injection strength. In low injection regime, the microwave frequency is roughly equal to  $\nu_{inj}$ . In contrast, the P1 frequency has little change with respect to

the injection power in this regime (circled with brown color), the microwave frequency is nearly constant at fixed frequency detuning, this regime is helpful to stabilize the microwave frequency against power fluctuations of the master laser and the VCSEL. The P1 frequency is qualitatively similar to the experimental study we did in [169], however, in another experimental study we investigated in [168], the microwave frequency appears more sensitive to the injection strength. This is most likely due to the reason that VCSEL internal parameter linear dichroism are different for these two VCSELs. More detailed study of how these two different situations occur will be theoretically studied in the section 3.5.7 (page 68).

### 3.5.6 Microwave Power

The optical frequency components in Figure 3.16 is calculated by adding up the  $|E_x(t)|^2 + |E_y(t)|^2$ . It is significant to understand how the generated microwave power varies with the injection parameters. In this result, the power loss due to the fiber length is ignored. In Figure 3.20, in the circled area, the microwave has high output power, this behavior is very similar to those in DFB lasers[58]. This is a bit different compared to our experimental result (Section 3.3.3 page:54). The difference may be due to the excitation of both linear polarization of the VCSEL in the experiment. In this result, only one polarization is excited by the optical injection.

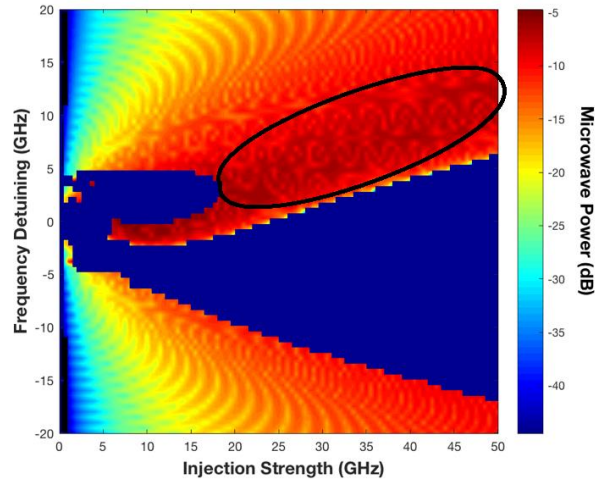


**Figure 3.20 Mapping of the normalized microwave power.**

The powers at the fundamental  $f_0$  and the second harmonic  $2f_0$  is visible in Figure 3.21. In Figure 3.21, the injection condition is set to  $(\eta_y, v_{inj}) = (10GHz, +6GHz)$ , the power in  $dB$  at  $f_0$  and  $2f_0$  are denoted as  $P_{f_0}$  and  $P_{2f_0}$ , respectively. In the power spectra, the second order harmonics can be characterized by the second harmonic distortion (SHD). High SHD can introduce high power penalty over the long distance transmission. The SHD is defined as the ration of the second harmonic power  $P_{2f_0}$  to the fundamental frequency power  $P_{f_0}$ . The power spectrum in Figure 3.21 has the SHD of  $(P_{2f_0} - P_{f_0}) = -16.04dB$ .

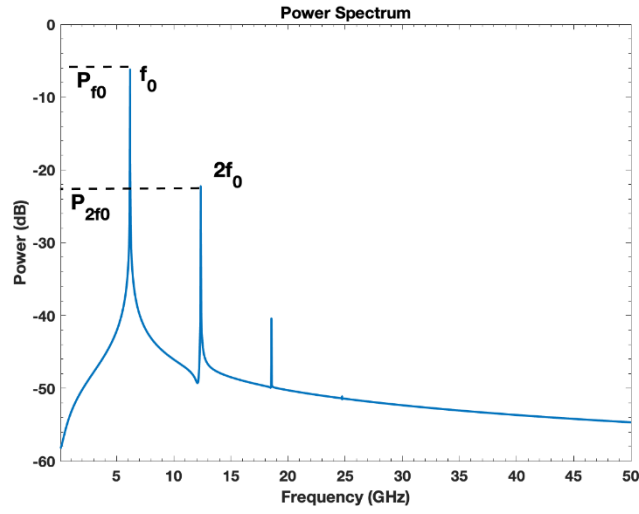


**Figure 3.21** the power spectrum under the injection condition of  $(\eta_y, \nu_{inj}) = (10GHz, +6GHz)$ .

The SHD of the optically injected VCSEL is mapped in Figure 3.22. It is shown that the SHD of the microwave signal is around  $-10dB$  when the injection condition is near the P2 and Chaos region. In the rest of the regions, the SHD is mostly less than  $-20dB$  when the injection condition is away from P2 regions. Increasing the frequency detuning over  $5GHz$ , reduces the SHD value down to less than  $-30dB$ . This simulation result is qualitatively in good agreement with our experimental observation.

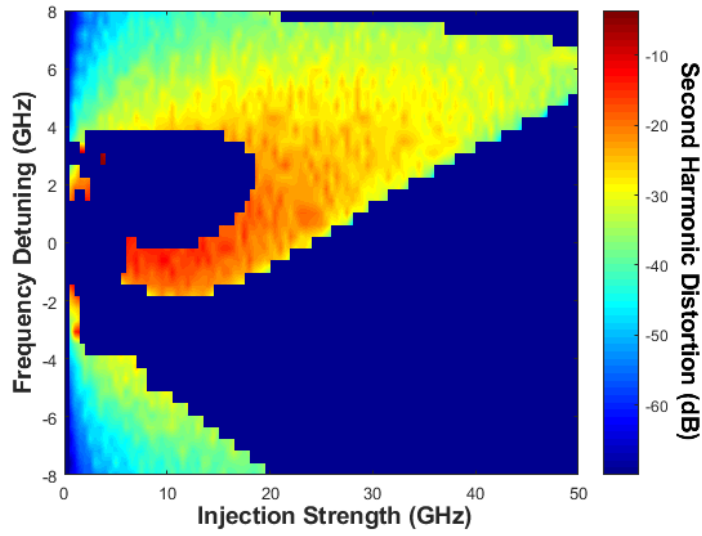


**Figure 3.22 SHD mapping of the electrical signal.**

### 3.5.7 Effect of Linear Dichroism on Microwave Frequency and Power

In this section, we performed simulation on how the linear dichroism  $\gamma_a$  affects the frequency and power of the fundamental microwave. The parameter  $\gamma_a$  is linked to the difference between the threshold gains in the two polarizations between VCSEL's two polarization modes. Positive  $\gamma_a$  means that the threshold current of Y-polarization is lower than that of X-polarization, and vice versa. Figure 3.23(a) shows the plot of the fundamental frequency versus linear dichroism with the injection condition being  $(\eta_y, \nu_{inj}) = (20GHz, +6GHz)$  and all other parameters are kept constant. The plot shows that the fundamental frequency increase almost linearly with the value of the linear dichroism. The Figure 3.23(b) shows the normalized microwave power variation with the change of the linear dichroism. Generally speaking, the microwave power varies within 1.8dB, relatively low compare to the effect of other parameters. This variation is possibly caused by the high noises level we added in the simulation.

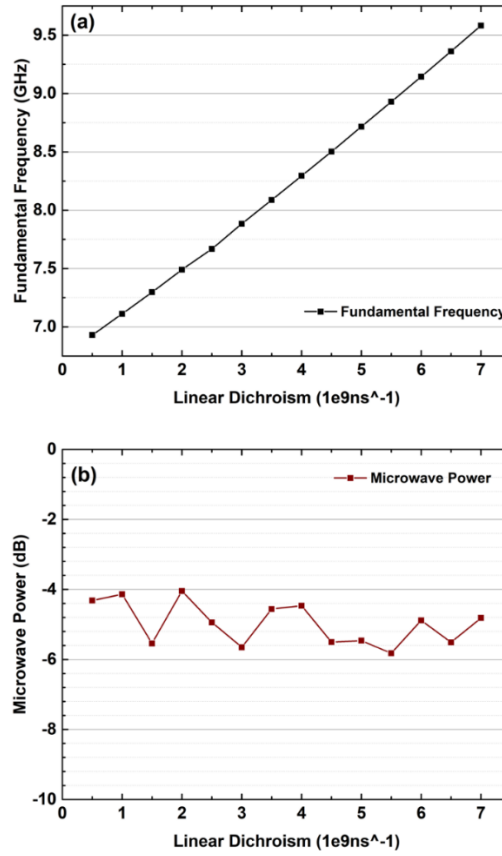


**Figure 3.23 Fundamental frequency(a) and microwave power versus the linear dichroism.**

Figure 3.24 shows the fundamental frequency and microwave power change with the injection strength at different linear dichroism. In Figure 3.24(a), frequency detuning is kept constant at  $\nu_{inj} = +6GHz$ , for the low  $\gamma_a = 0.5ns^{-1}$ , at lower injection strength the fundamental frequency increases slower compare to the higher injection strength situation. This effect is more prominent pronounce in  $\gamma_a = 7.0ns^{-1}$  curve. At lower injection strength, the increase rate of the fundamental frequency with  $\gamma_a = 7.0ns^{-1}$  is less compare to  $\gamma_a = 0.5ns^{-1}$  and  $\gamma_a = 4.0ns^{-1}$ , at the higher injection strength, the slope of the curve is also less compare to the  $\gamma_a = 0.5ns^{-1}$  situation. The laser entered injection locking state at injection strength of  $\eta_y = 50GHz$  and  $\eta_y = 60GHz$  for  $\gamma_a = 0.5ns^{-1}$ , and  $\gamma_a = 7.0ns^{-1}$  respectively, which also

indicate that the at lower  $\gamma_a$  value the slave laser is easier locked to the master laser compare to the higher  $\gamma_a$  with the same amount of injection strength. To summarize the Figure 3.24(a), if the application requires to generate higher microwave frequency with lower injection frequency detuning, it is preferred to choose the VCSEL with higher  $\gamma_a$  value because it can achieve higher fundamental frequency under the same injection condition. However, for a higher  $\gamma_a$  VCSELs, the fundamental frequency is less sensitive to the injection strength.

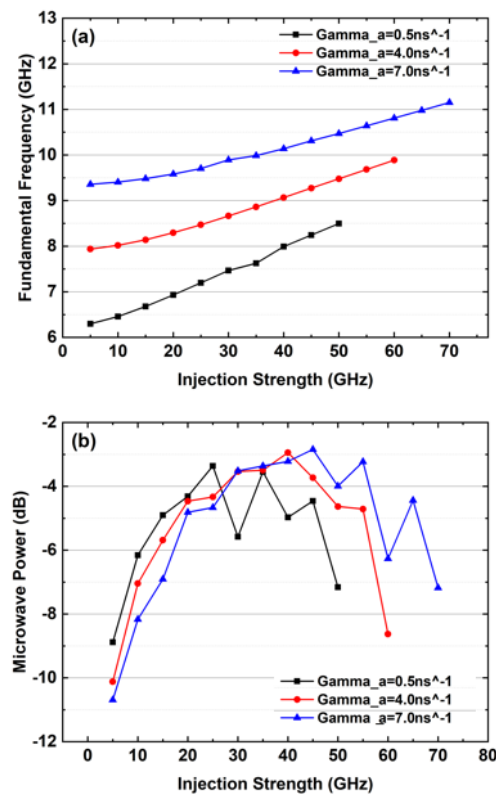


**Figure 3.24(a) fundamental frequency increasing with the increase of the injection strength at three different linear dichroism ( $\gamma_a$ ). (b) Microwave power versus the increasing injection strength.**

In Figure 3.24(b) the microwave power variation with the injection strength at different linear dichroism. All three curves show a relatively high value around the injection strength  $\eta_y$  of 25GHz to 40GHz range, this means the microwave power

trend is not affected by the linear dichroisms much. In all three situations, the microwave power drops before the laser enters the injection locking state.

### 3.5.8 Effect of Linear Birefringence on Microwave Frequency and Power

The parameter linear birefringence  $\gamma_p$  describes the optical frequency separation between the x-polarization and the y-polarization modes. Figure 3.25 is showing the fundamental frequency and microwave power versus the linear birefringence under the same injection condition of  $(\eta_y, \nu_{inj}) = (20GHz, +6GHz)$  with all other parameters kept constant. From Figure 3.25 we can observe that the fundamental frequency does not vary with the linear birefringence, and a small variation of microwave power can be observed with increase of the linear birefringence.

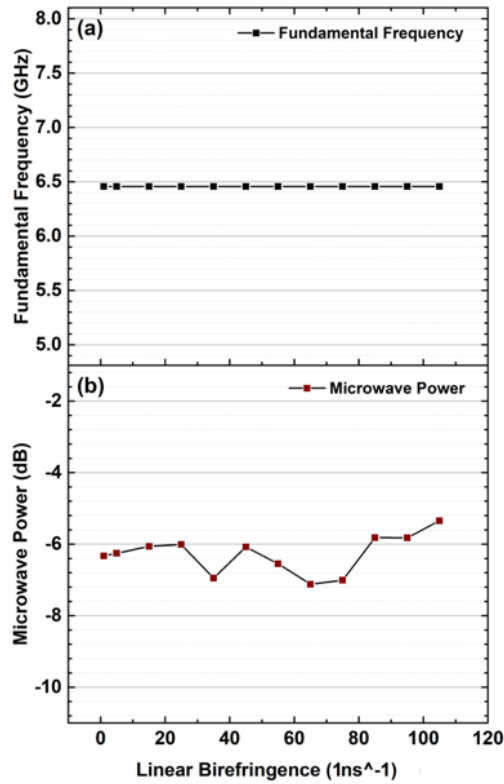


**Figure 3.25 Fundamental frequency(a) and microwave power versus the linear dichroism.**



### 3.6 Chapter Summary

In this chapter, photonic microwave generation based on P1 dynamics of a VCSEL subject to parallel injection has been studied experimentally and theoretically. For the experimental result, a continuous tuning of the microwave frequency from 4GHz to up to an instrumentation limited 15GHz was observed. Further increases the microwave frequency are possible by increasing the injection power or the frequency detuning. We have demonstrated that the frequency of the generated microwave increases with increasing frequency detuning above the Hopf bifurcation boundary and increasing injection power. The frequency detuning has little influence on the power of the generated microwave except two small areas. On the other hand, the SHD decreases with increasing frequency detuning for higher injection power. The injection power has some effect on the power of the generated microwave signal, however, it has very limited effect on the SHD. The numerical result quantitatively backed up the experimental study.

# 4 Stabilization on VCSEL Based Photonic Microwave Generation

## 4.1 Chapter Introduction

In the previous chapter, the experimental result and numerical simulation of the photonic microwave generation utilizing VCSEL's P1 oscillation dynamic have been presented. This chapter will focus on minimizing the phase noise and reducing the generated microwave linewidth. Optical feedback is a simple and low-cost method to achieve linewidth reduction. It has been theoretically and experimentally proved in DFB lasers [58], [157], [170]. Dual feedback loops have also been used to reduce the linewidth of the generated photonic microwave in two-mode VCSEL [171]. In this chapter, we study the effect of both single optical feedback and double optical feedback on the linewidth of the generated photonic microwave based P1 oscillation in a single-mode VCSEL. We also study the effect of the feedback phase on the side-peaks suppression.

## 4.2 Experimental Setup and Data Acquisition

The schematic of the experimental setup is shown in Figure 4.1. The experiment was set up in free-space to overcome the uncertainty of injection and feedback polarization directions. A commercial single mode VCSEL (RayCan RC33xxx1-T) was used as the slave laser (SL). The VCSEL was driven by a low noise current source (Yokogawa GS200 DC Voltage/Current source), and its temperature was controlled to 21°C.

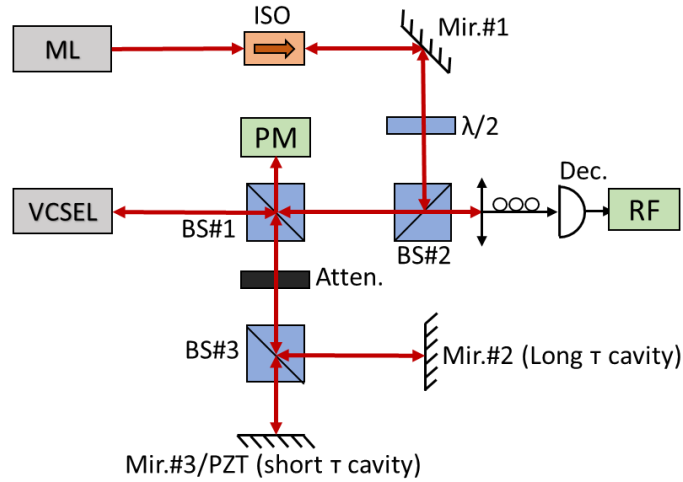


**Figure 4.1 The experimental setup. ML: Master laser, ISO: Optical isolator, Mir.: Mirror,  $\lambda/2$ : Half-wave plate, BS: Beam splitter, Atten: Optical attenuator, PM: Power meter, Dec: Photodetector, RF: Radio frequency spectrum analyzer, PZT: Piezo stage.**

A tunable laser (Agilent 81682A installed on Agilent 8164A) was used as the master laser (ML). The maximum output power of the tunable laser is 10mW power and its linewidth is 1MHz. The output of the ML passes-through an optical isolator to prevent the optical injection from the VCSEL and the optical feedback from the optical components. The polarization of the optical injection beam from the ML was adjusted by a half-wave plate ( $\lambda/2$ ) to ensure the polarization of the injection beam is parallel to the free running VCSEL's polarization direction. The injection power was controlled by the ML's output power. The optical injection power  $P_{inj}$  was measured just before the injection beam enters the VCSEL. It is noted that the actual injection power that VCSEL receives was less than the measurement due to the coupling loss. The tuning of the frequency detuning  $\Delta f = f_{ML} - f_{SL}$  was achieved by changing the frequency of the ML.  $f_{ML}$  and  $f_{SL}$  are the frequencies of the free-running ML and the free-running VCSEL, respectively. Optical feedback cavities were created by mirror#2 (Mir.#2) and mirror#3 (Mir.#3), which are referred to as cavity 1 and 2, respectively. To study the linewidth of the generated photonic microwave with respect to the feedback phase, mirror#3 was mounted on a piezo stage (PZT, PI-P752.1C1) to finely tune the cavity

length. The feedback round trip times in the cavities formed by mirror#2 and 3 are  $7.3ns$  ( $\tau_L$ ) and  $5.1ns$  ( $\tau_s$ ), respectively. The feedback powers from both feedback cavities were the same and were adjusted by an optical attenuator (Atten.) and monitored by a power meter (PM). The output of the VCSEL was detected by a  $12GHz$  bandwidth photodetector (New Focus 1554-B) and recorded by a  $30GHz$  RF spectrum analyzer (Anritsu MS2667C). The frequency resolution of the RF spectrum analyzer's is set at  $10kHz$  and the sweep time is 50 milliseconds unless stated otherwise.

## 4.3 Experimental Result

The focus of this section is the effect of optical feedback on the linewidth and stabilization of photonic microwave generated from the VCSEL's P1 dynamics. The P1 dynamics have previously been shown to exist over large injection parameters [168]. Two cases of optical feedback are studied. The first case is single feedback, which means that only optical feedback from one feedback cavity is allowed and the feedback from the other feedback cavity is blocked. The second case is double feedback, the feedback from both cavities 1 and 2 are re-entered into the VCSEL.

### 4.3.1 Characterization

At the temperature of  $22.01^\circ C$ , the threshold current of the VCSEL was  $2.1mA$ . Near the threshold current, the VCSEL operated in one linear polarization (Y-polarization). When the bias current was increased to  $2.4mA$ , the polarization direction switched to its orthogonal polarization direction (X-polarization). Further increases in the bias current to  $5.7mA$  resulted in the polarization direction switching back to the Y-polarization. The polarization remains in the Y-polarization state within the remaining operating current range. The VCSEL was operated at  $8mA$  (Y-polarization) through the experiment, unless stated otherwise. At this bias current, the VCSEL's lasing wavelength was  $1559.15nm$  and its output power was  $1.87mW$ .

### 4.3.2 Single Feedback

#### Single Feedback and Linewidth of the Microwave

When the injection parameters are set at  $(\Delta f, P_{inj}) = (12.8 \text{ GHz}, 0.703 \text{ mW})$ , as shown in Figure 4.2(a), the VCSEL exhibits P1 dynamics and the fundamental frequency  $f_0$  is  $13.34 \text{ GHz}$ . The full width at half maximum (FWHM) linewidth of the generated photonic microwave was measured and found to be  $4.62 \text{ MHz}$ . When the optical feedback from one cavity was introduced into the VCSEL (cavity 2 was blocked) and the feedback power adjusted to  $8 \mu\text{W}$ , the power spectrum shown in Figure 4.2(b) was obtained. Figure 4.2(b) indicates that the linewidth has been reduced to  $1.13 \text{ MHz}$ , however, many residual side peaks are observed and the spacing between side peaks is  $141 \text{ MHz}$ , which is very close to the reciprocal of the feedback delay time ( $7.3 \text{ ns}$ ) of  $137 \text{ MHz}$ . If cavity 1 is now blocked and instead  $8 \mu\text{W}$  of feedback power introduced from cavity 2, the power spectrum of the VCSEL is modified as shown in Figure 4.2(c). The spectrum is similar to Figure 4.2(b), with multiple side peaks uniformly spaced at  $198 \text{ MHz}$ , which is near to  $1/\tau_s = 196 \text{ MHz}$ . Different injection conditions were also examined and similar results observed. This phenomenon is the same as that in the simulation results [58] and the experimental results of [157] for DFB lasers.

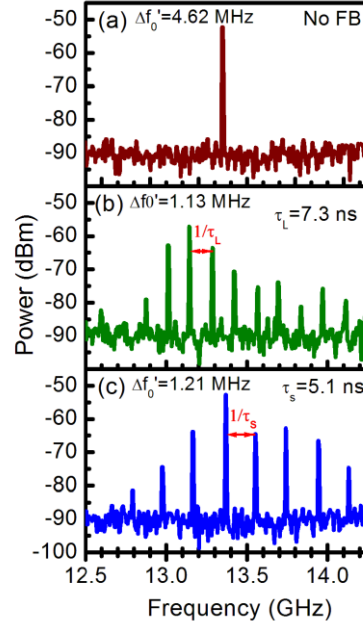


**Figure 4.2 Power spectra of the VCSEL. (a) without optical feedback, (b) with optical feedback from cavity 1, (c) with optical feedback from cavity 2.**

### Feedback Phase and Side Peaks Suppression

In this study, we also investigate the dynamics of the VCSEL with respect to the feedback phase. The feedback phase from cavity 2 is controlled by tuning the PZT stage distance. We fix the injection parameters  $(\Delta f, P_{inj}) = (10.43 \text{ GHz}, 0.703 \text{ mW})$  and feedback power  $P_{fb} = 8 \mu\text{W}$ . Figure 4.3(a) is one of the representative power spectra of the VCSEL when PZT stage distance is set between  $2120\text{nm}$  to  $2740\text{nm}$ . The obtained signal exhibits multiple side peaks, the same phenomena as described in Figure 4.3(b) and (c). We refer it as side peaks (SP) phase condition. When we move the PZT distance to the range of  $1890\text{nm}$  to  $2120\text{nm}$ , a very stable microwave signal is obtained, as shown in Figure 4.3(b), all the side peaks are suddenly suppressed, we refer this condition as side peaks suppression (SPS) phase condition. Continued increase of the mirror's distance move the system back into the SP phase condition for the PTZ distance of  $1380\text{nm}$  to  $1890\text{nm}$ , as shown in Figure 4.3(c). The summarized different signal states are presented in Figure 4.3(d). The wine color and blue color represent the SP phase condition and SPS phase condition,

respectively. From analyzing Figure 4.3(d), it is found that side peaks are periodically suppressed when the external cavity length is increased. The period for the side peaks suppression is approximate to  $750\text{nm}$ , which is about half of the lasing wavelength of the VCSEL, which corresponds to a  $2\pi$  feedback phase change.

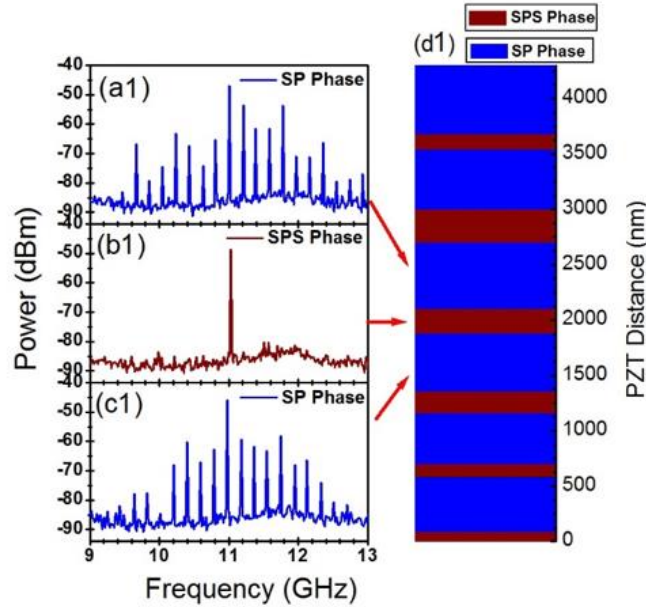


**Figure 4.3 (a1-c1) Power spectra of the VCSEL under injection condition of  $(\Delta f, P_{inj}) = (10.43\text{ GHz}, 0.703\text{ mW})$  with different PZT distance, (d1) SPS phase condition and SP phase condition states as a function of the PZT moving distance.**

In Figure 4.4, we changed the injection condition to  $(\Delta f, P_{inj}) = (10.73\text{ GHz}, 0.689\text{ mW})$ , the power spectra behavior of the SP phase and SPS phase condition remains similar in Figure 4.4 (a2-c2), the position of SP and SPS phase condition as function of PZT distance in Figure 4.4(d2) are different compare to the one in Figure 4.4(d1). which indicates that the SP and SPS conditions are not only dependent on the feedback phase, but also dependent on the injection parameters.

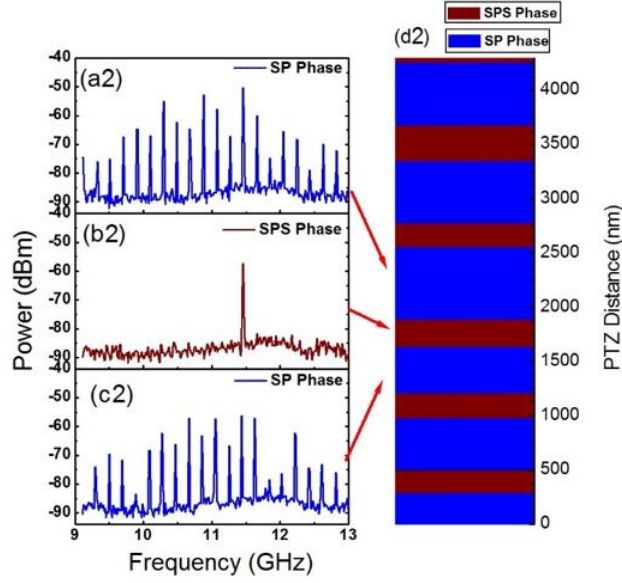


**Figure 4.4 (a2-c2) Power spectra of the VCSEL under injection condition of  $(\Delta f, P_{inj}) = (10.73 \text{ GHz}, 0.689 \text{ mW})$  with different PZT distance, (d2) SPS phase condition and SP phase condition states as a function of the PZT moving distance.**

### 4.3.3 Double feedback

In this section, we study whether the side peaks under the single feedback with SP phase condition can be suppressed by adding the second feedback, just like those in DFB lasers [58], [157]. Figure 4.5 shows that the power spectra of the optically injected VCSEL subject to optical feedback. The injection parameters  $(\Delta f, P_{inj})$  are  $(11.42 \text{ GHz}, 0.685 \text{ mW})$ . When the VCSEL is subject to single feedback from cavity 2 with the feedback power of  $8 \mu\text{W}$  and the PZT distance is tuned to SP phase condition position, there are many side peaks around the fundamental frequency, as shown in Figure 4.5(a). When optical feedback from cavity 1 is introduced and feedback power from each cavity set at  $4 \mu\text{W}$ , the side peaks are suppressed in Figure 4.5(b). The results indicate that the second feedback suppresses the side peaks.



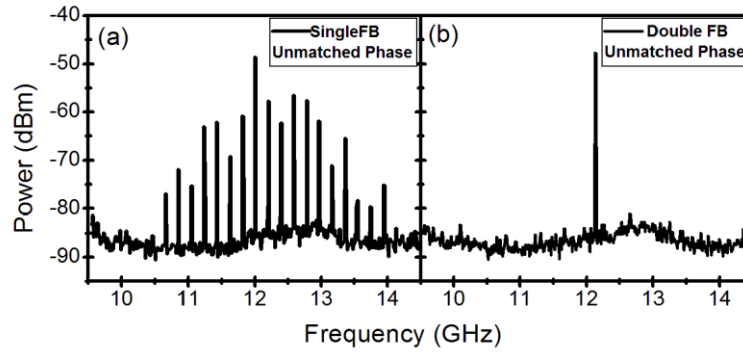


**Figure 4.5 Power spectra of the VCSEL with (a) single feedback, (b) double feedback.**

#### **Feedback strength and linewidth of microwave**

The linewidth reduction through dual-cavity feedback with the different feedback power has also been investigated. Figure 4.6 shows the power spectrum of the VCSEL under the injection parameters of  $(\Delta f, P_{inj}) = (12.8 \text{ GHz}, 0.772 \text{ mW})$  with different feedback conditions. Figure 4.6(a) is for the power spectrum of the VCSEL with optical injection, but without optical feedback. The result indicates that the VCSEL operates in P1 dynamics with the fundamental frequency  $f_0 = 13.5 \text{ GHz}$ . The microwave FWHM linewidth ( $\Delta f_0'$ ) was found to be  $3.6 \text{ MHz}$ . The linewidth reduction of the microwave signal has been seen when the combined optical feedback power from two cavities was set at  $3 \mu\text{W}$ , as shown in Figure 4.6(b). The linewidth was reduced to  $2.40 \text{ MHz}$  and the fundamental frequency also increases slightly to  $f_0 = 13.7 \text{ GHz}$ . In Figure 4.6(c), when the total feedback power increases to  $6 \mu\text{W}$ , a further linewidth reduction of  $\Delta f_0' = 1.62 \text{ MHz}$  can be achieved. Further increases in the feedback power to  $9 \mu\text{W}$ , narrow the linewidth to  $0.49 \text{ MHz}$ , which is about one tenth of the linewidth without optical feedback. Increasing the feedback power beyond  $9 \mu\text{W}$  causes instability in the microwave generation, with multiple, random spaced power peaks appearing in RF spectrum, which evidentially lead to the appearance of chaos dynamics.

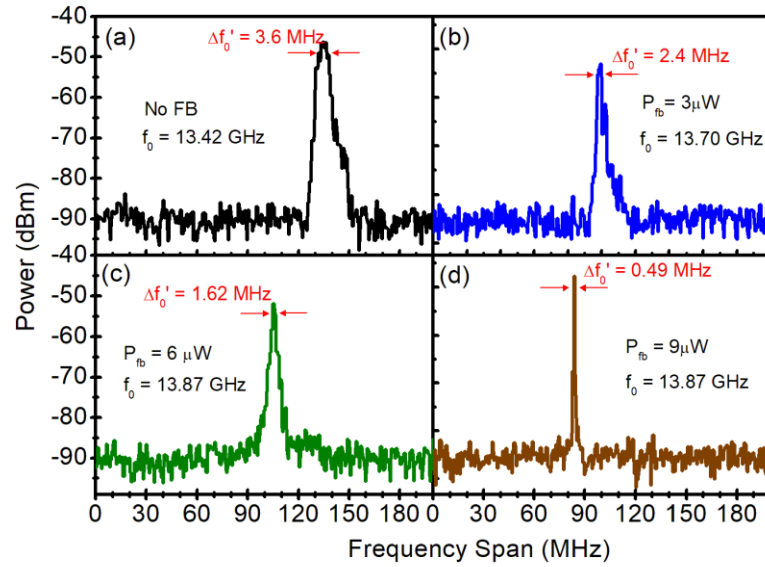


**Figure 4.6 Power spectra of the VCSEL. (a) Without optical feedback, (b-d) with double feedback and the total feedback power is (b)  $3\mu W$ , (c)  $6\mu W$ , (d)  $9\mu W$ .**

The relationship between the microwave FWHM linewidth and feedback strength is summarized in Figure 4.7(a). The graph shows an almost inversed linear relationship between the linewidth and the feedback power. Figure 4.7(b) shows the fundamental microwave frequency as a function of the feedback power. There is frequency shift of about  $300MHz$  in the fundamental frequencies after applying the feedback. This is due to the increase of the carrier density, which reduce the cavity resonant frequency [172].

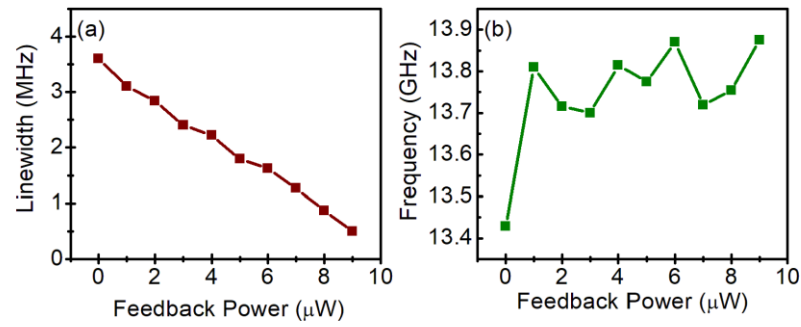


**Figure 4.7 (a) Linewidth and (b) fundamental frequency of the generated microwave as a function of the feedback power.**

### Feedback Strength and Stability of the Microwave

Readers may have noticed that the microwave fundamental frequencies do not always appear at the center of the frequency span in Figure 4.6, this is caused by fluctuation in the fundamental frequency. Practically, the fundamental frequency can randomly appear in the frequency range even at fixed injection parameters during the experiment. This behavior is highly correlated with the noise of the bias current, performance of the temperature controller and the accuracy of the injection tunable laser or the slight change of the injection coupling efficiency caused by the optical table vibrations during the experiment.

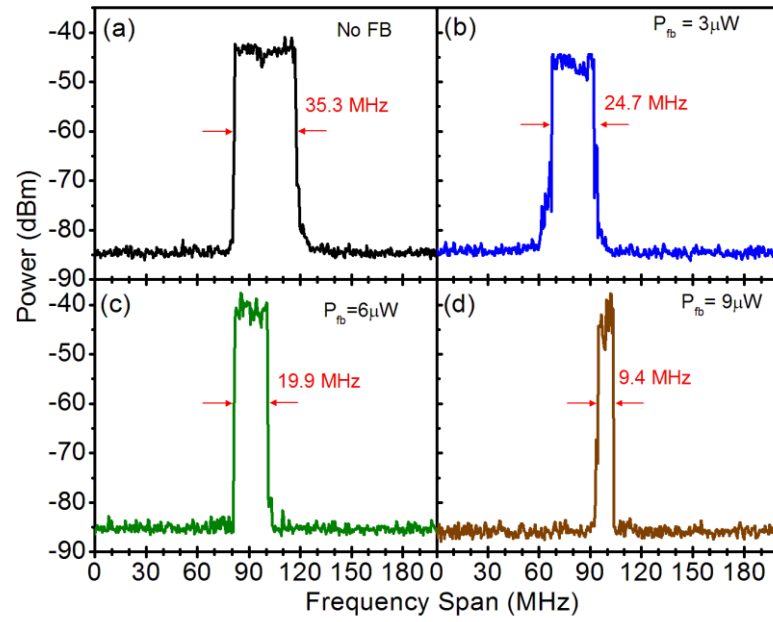


**Figure 4.8** Power spectra of the VCSEL when the sweep time of the RF spectrum analyzer is set at 30 seconds. (a) Without feedback, (b-d) with double feedback and the total feedback powers are (b)  $3\mu W$ , (c)  $6\mu W$ , (d)  $9\mu W$ .

However, in this experiment we have noticed that adding dual-cavity optical feedback also helps to improve the stability of the microwave fundamental frequency. To demonstrate this effect, the sweep time of the RF Spectrum analyzer is set to be 30 seconds, so the RF analyzer will capture multiple peaks during this timeframe and display them on a single image. The results can be found in Figure 4.8. With no feedback enabled, the location of the  $f_0$  appears within  $35.3MHz$  range. When the VCSEL is subject to optical feedback from both cavities with the total feedback power of  $3\mu W$ , the range of  $f_0$  reduces to  $24.7MHz$ . Increasing the feedback power to  $6\mu W$ , and  $f_0$  is captured within a  $19.9MHz$  range. Further increases in the feedback power to the maximum allowed feedback power of  $9\mu W$ , before unstable signal occurs, and the  $f_0$  range is reduced to  $9.4MHz$ . The results show a significant reduction in the range of  $f_0$  appearing with double feedback compared to that without optical feedback, which indicates that double feedback can increase the stability of the photonic microwave generated based on P1 dynamics.

### Feedback Phase and Stability of the Microwave

As described above sections, the side peaks suppression in the single feedback case is sensitive to the optical feedback phase. Adding a second feedback can suppress the side peaks for the SP phase condition. In this section, we will examine whether SPS phase condition feedback in one feedback cavity has the same beneficial effect of linewidth reduction and stability as under double feedback.

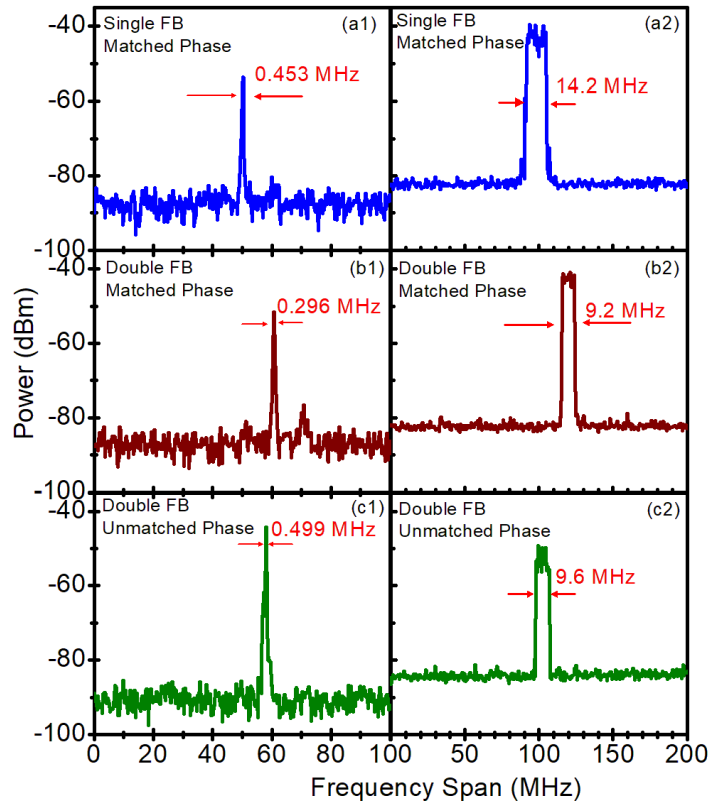


**Figure 4.9** The power spectra of the VCSEL with the different feedback configurations. The left and right columns are for the sweep time of the RF spectrum analyzer of 50 millisecond and 30 seconds, respectively. (a1), (a2) single feedback with SPS phase condition, (b1), (b2) double feedback with SPS phase condition, (c1), (c2) double feedback with SP phase condition.

Figure 4.9 illustrates the power spectra of VCSEL when the injection parameters and feedback power are  $(\Delta f, P_{inj}) = (11.42 \text{ GHz}, 0.685 \text{ mW})$  and  $8 \mu\text{W}$ , respectively. The left and right columns are for a sweep time of 50 millisecond and 30

seconds in the RF spectrum analyzer, respectively. Figure 4.9(a1) and (a2) are obtained when the VCSEL is subject to SPS phase condition single feedback. Fig. 8(a1) shows a linewidth of  $0.453\text{MHz}$ . When the sweep time of the RF spectrum analyzer is increased to 30 second, the power spectrum of the VCSEL is recorded and plotted in Figure 4.9(a2). The result indicates that the fluctuation range of the fundamental frequency  $f_0$  is about  $14.2\text{MHz}$ . When the second feedback is introduced, we keep the total feedback power to  $8\mu\text{W}$ . We can see that the linewidth has reduced to  $0.296\text{MHz}$  for 50 ms sweep time, as shown in Figure 4.9(b1), and the fluctuation range of the fundamental frequency  $f_0$  has also decrease to  $9.2\text{MHz}$ , as indicated in Figure 4.9(b2). When the PZT is adjusted to make the feedback phase from cavity 2 with SP phase condition, the power spectra of the VCSEL from the short sweep time in Figure 4.9(c1) and long sweep time in Figure 4.9(c2), indicates that the fluctuation range of the fundamental frequency is very close to the double feedback cavity situation seen with the phase match, but has increased slightly to  $9.6\text{MHz}$ . However, the linewidth measured using the  $50\text{ms}$  sweep time has increased dramatically to  $0.499\text{MHz}$ . The results in Figure 4.9 demonstrate that the second feedback can be used to reduce the linewidth and improve the stability of the generated microwave. Careful adjustment of the feedback phase can further decrease the linewidth.

## 4.4 Numerical Study

### 4.4.1 Simulation Model

The photonic microwave generated via P1 dynamic from optical feedback has been numerically simulated using the spin-flip model that is similar to that in Chapter 3, but added the feedback terms:

$$\begin{aligned}
 \frac{dE_x}{dt} = & \kappa(1 + i\alpha)(NE_x - E_x + inE_y) \\
 & -(\gamma_a + i\gamma_p)E_x + \eta_x E_{inj} e^{i2\pi(\nu_{inj} - \nu)t} \\
 & + \xi_{f1} E_x(t - \tau_1) e^{-i(2\pi\nu\tau_1 + \phi_1)} \\
 & + \xi_{f2} E_x(t - \tau_2) e^{-i(2\pi\nu\tau_2 + \phi_2)} + F_x
 \end{aligned} \tag{4.1}$$

$$\begin{aligned}
\frac{dE_y}{dt} = & \kappa(1 + i\alpha)(NE_y - E_y - inE_x) \\
& + (\gamma_a + i\gamma_p)E_y + \eta_y E_{inj} e^{i2\pi(v_{inj}-v)t} \\
& + \xi_{f1} E_y(t - \tau_1) e^{-i(2\pi v\tau_1 + \varphi_1)} \\
& + \xi_{f2} E_y(t - \tau_2) e^{-i(2\pi v\tau_2 + \varphi_2)} + F_y
\end{aligned} \tag{4.2}$$

$$\begin{aligned}
\frac{dN}{dt} = & -\gamma_e N (1 + |E_x|^2 + |E_y|^2) + \gamma_e \mu \\
& - i\gamma_e n(E_y E_x^* - E_x E_y^*)
\end{aligned} \tag{4.3}$$

$$\begin{aligned}
\frac{dn}{dt} = & -\gamma_s n - \gamma_e n (|E_x|^2 + |E_y|^2) \\
& - \gamma_e N(E_y E_x^* - E_x E_y^*)
\end{aligned} \tag{4.4}$$

The two feedback loops are specified by the optical feedback parameters  $(\xi_{f1}, \tau_1)$  and  $(\xi_{f2}, \tau_2)$ , where the  $\xi_{f1}, \xi_{f2}$  the feedback strength for the feedback loop 1 and feedback loop 2, respectively.  $\tau_1$  and  $\tau_2$  are the feedback delay times for the feedback loop 1 and feedback loop 2, respectively. In the feedback terms in equations (4.1) and (4.2), we also add a phase  $\varphi_1$  and  $\varphi_2$  in conjunction with phase change due to time delay  $\tau_1$  and  $\tau_2$  to study the feedback phase effect. The phase  $\varphi$  takes 10 equally spaced points within the range of  $2\pi$ . The injection parameter is specified by the  $(\eta, v_{inj})$ , the definition is same to the Section 3.4 above. In the simulation, the VCSEL operates in the P1 oscillation dynamic state, the slave laser VCSEL, injection, and feedback are assumed to have aligned polarization. The typical VCSEL simulation parameters are used, they are listed in Table 4.1 unless stated otherwise.

**Table 4.1 Values used for simulation**

Parameter	Symbol	Value
linewidth enhancement factor	$\alpha$	3
linear dichroism	$\gamma_a$	$3ns^{-1}$
linear birefringence	$\gamma_p$	$94.3ns^{-1}$
decay rate of the total carrier population	$\gamma_e$	$0.67ns^{-1}$
spin-flip rate	$\gamma_s$	$140ns^{-1}$
field decay rate	$k$	$125ns^{-1}$
injection field amplitude	$E_{inj}$	1
noise strength	$\beta_{sp}$	$4e^{13}$

The numerical integration has a time step of  $1ps$  and it is carried over a time span of  $10\mu s$ , resulting the simulated power spectra having  $100kHz$  resolution.

#### 4.4.2 Single Feedback

##### Feedback Strength

We observed the linewidth reduction experimentally in Section 4.3.2. In this section, we performed a numerical study on how the single optical feedback is affecting the linewidth. Figure 4.10 displays the power spectra of the VCSELS with the above parameters when the injection condition is kept constant at  $(\eta_y, v_{inj}) = (20GHz, +10GHz)$  and the feedback round trip time is set to  $\tau = 5.1ns$  to be in consistent with the experimental setup. With these parameters, the VCSEL operates at P1 dynamic. Figure 4.10(a) is for the case when the VCSEL is subject to optical injection only. The linewidth is calculated to be  $\Delta f_0' = 30.6MHz$ . Introducing one feedback with feedback strength of  $\xi_f = 0.6GHz$ , as shown in Figure 4.10(b), we observe a significant linewidth reduction, the linewidth is measured as  $\Delta f_0' = 2.73MHz$ , less than one tenth of the linewidth in Figure 4.10(a). At the same time, multiple evenly spaced side peaks appeared, we denoted the power ratio between the peak power at the fundamental frequency and the highest side peak power as the main/side peaks ratio (MSPR). Low MSPR is considered as more unstable compare to the high MSPR situation. MSPR in Figure 4.10(b) is calculated to be  $17.77dB$ . Increasing the feedback strength to  $1.4GHz$  in Figure 4.10(c), we see a further linewidth



reduction of  $\Delta f_0' = 1.43\text{MHz}$ , however, the MSPR is decreased to  $\text{MSPR} = 12.74\text{dB}$ . Increasing the feedback strength to  $2.0\text{GHz}$  in Figure 4.10(d), we observe the linewidth to be  $\Delta f_0' = 1.47\text{MHz}$  with a very low MSPR of  $7.41\text{dB}$ .

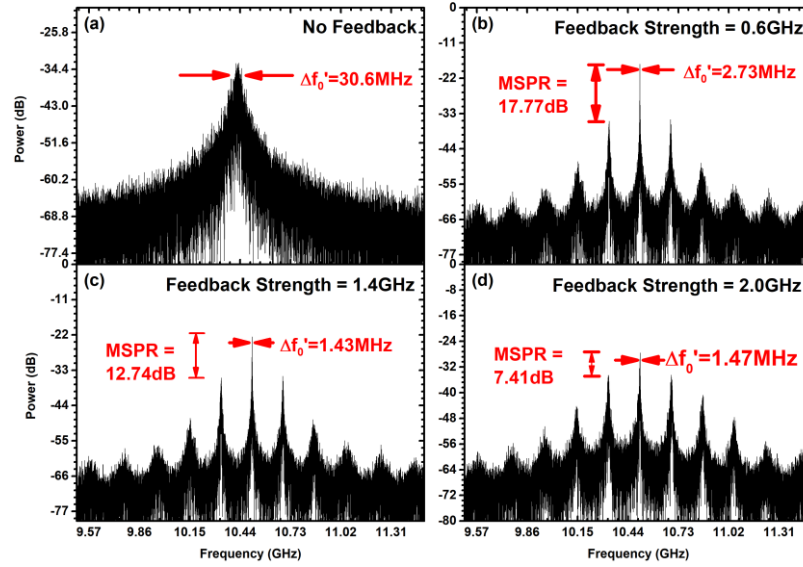


**Figure 4.10** Power spectra under feedback strength of (a) zero, (b)  $0.6\text{GHz}$ , (c)  $1.4\text{GHz}$  and (d)  $2.0\text{GHz}$ .

Figure 4.11, presents a detailed investigation on the influences of feedback strength on the characteristic of P1 microwaves in single feedback setup scenario. Black line and red line representing the linewidth changing and MSPR changing with feedback strength, respectively.

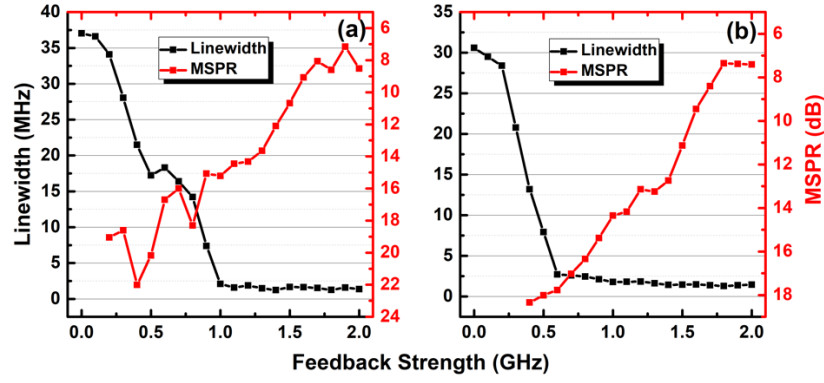


**Figure 4.11 Linewidth and MSPR versus feedback strength. (a) Under the injection condition of  $(\eta_y, \nu_{inj}) = (25\text{GHz}, +6\text{GHz})$ , (b)  $(\eta_y, \nu_{inj}) = (20\text{GHz}, +10\text{GHz})$**

Figure 4.11(a) shows that under the injection condition of  $(\eta_y, \nu_{inj}) = (25\text{GHz}, +6\text{GHz})$ , the linewidth decreases with increasing feedback strength until the feedback strength reaches around  $1.0\text{GHz}$ . Further increasing the feedback strength has little effect on linewidth reduction until the VCSEL start operating in other dynamics. The MSPR however, providing evidence of decreasing with the increase of the feedback strength. Figure 4.11(b) displayed that under the injection condition of  $(\eta_y, \nu_{inj}) = (20\text{GHz}, +10\text{GHz})$ , the linewidth reduction reaches stable at around  $0.6\text{GHz}$  of feedback strength, while the MSPR trend to follow the same regular pattern. Compare this simulation results with our experimental results, the simulation shows that the linewidth remains same after the feedback strength increases to a certain value, however, the experimental results demonstrate that the P1 microwave will be destroyed with further increasing the feedback power after the P1 microwave reaches its minimal linewidth. The exact reason of such disagreement is unknown. Further investigation is needed.

### Feedback Phase

The results above are for the in-phase situation ( $\varphi = 0$ ), we now introduce the phase variation into our simulation as we have found the phase of the optical feedback can also impact the behavior of the P1 microwave in the experiment.

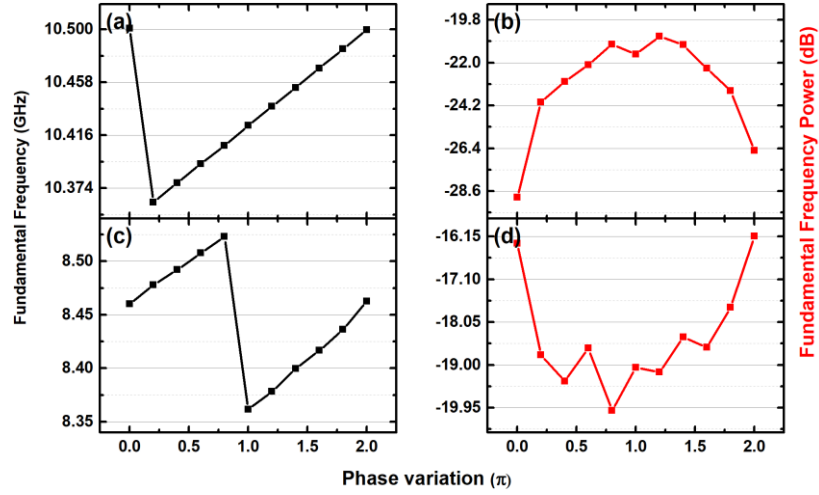


**Figure 4.12 Fundamental frequency and its power as a function of the feedback phase.. The injection parameters of  $(\eta_y, \nu_{inj}) =$  (a) and (b) (20GHz, +10GHz), (c) and (d) (23GHz, +8GHz).**

Figure 4.12(a) and (c) show the fundamental frequency change with the phase variation. The fundamental frequency under injection condition of  $(\eta_y, \nu_{inj}) = (20\text{GHz}, +10\text{GHz})$  in Figure 4.12(a) starts at 10.5GHz when the feedback is in phase. When phase change to  $0.2\pi$ , the microwave frequency drop to 10.362GHz. Further increase the feedback phase, the fundamental frequency increasing proportionally with phase variation until it reaches its original fundamental frequency of 10.5GHz when the feedback is in phase again (phase variation =  $2\pi$ ). Change the injection condition to  $(\eta_y, \nu_{inj}) = (23\text{GHz}, +8\text{GHz})$  in Figure 4.12(c), the fundamental frequency first increases with the increasing feedback phase and then it drops suddenly when the feedback phase increase from  $0.8\pi$  to  $1\pi$ . Further increase the feedback phase, the

fundamental frequency increases with the increasing feedback phase again. Figure 4.12 (b) and (d) display the fundamental frequency power changing with the phase variation. The fundamental frequency power varies in range of  $7.6\text{dB}$  and  $3.8\text{dB}$  for each of the example injection condition situation. We have found that in general, the power fluctuation is less when injection strength is higher.

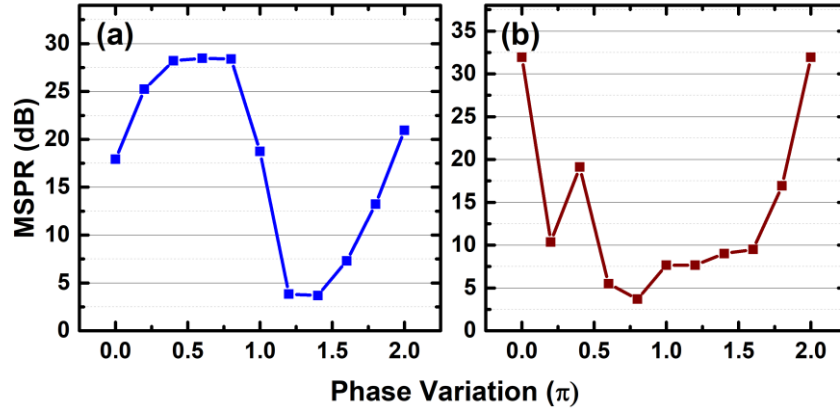


**Figure 4.13 MSPR versus the feedback phase . Under the injection condition of  $(\eta_y, \nu_{inj}) = (20\text{GHz}, +10\text{GHz})$  for (a) and  $(\eta_y, \nu_{inj}) = (23\text{GHz}, +8\text{GHz})$  for (b).**

Figure 4.13(a) and (b) are the MSPR as a function of the feedback phase with fixed injection condition. Figure 4.13(a) shows that the MSPR varies by approximately 25 dB over a feedback phase range of  $2\pi$  with a maximum of approximately 28 dB and a minimum of approximately 3 dB. However, for the injection parameters of (23 GHz, +8GHz), as shown in Figure 4.13(b), the MSPR varies by approximately 29 dB over a feedback phase range of  $2\pi$  with a maximum of approximately 32 dB and a minimum of approximately 3 dB. In addition, the patterns of variation in Figures 4.13(a) and (b) are significantly different, which indicates that the characteristics of the generated microwave depend not only on the feedback phase but also on the injection parameters. We have tested the P1 microwave under multiple injection conditions, the pattern of the P1 microwave power and MSPR with the change of feedback phase has not been found.

#### 4.4.3 Double feedback

The single feedback setup decreased the microwave linewidth as we discovered both in the experimental study and numerical study, to further improve the P1 microwave quality, a second optical feedback path is added in the experiment. In order to verify and extend such study, we now numerically simulate the generated P1 microwave under double optical feedback setup.

##### Linewidth Reduction

In this section, the injection condition is set to be  $(\eta_y, \nu_{inj}) = (20GHz, +10GHz)$  and the VCSEL is in P1 dynamic. The feedback delay times  $(\tau_1, \tau_2)$  are set to be  $(5.1ns, 7.3ns)$  for feedback#1 and feedback#2, respectively. We refer the short and long delay time feedback paths as short-cavity, and long-cavity respectively. To isolate the effect of the feedback strength to the P1 microwave linewidth in double feedback setup, the phase variations for each feedback path are set to be 0 at the beginning, assuming the both feedbacks are in-phase to the laser's output. We numerically studied the feedback strengths from 0 to  $0.8GHz$  for each feedback path.

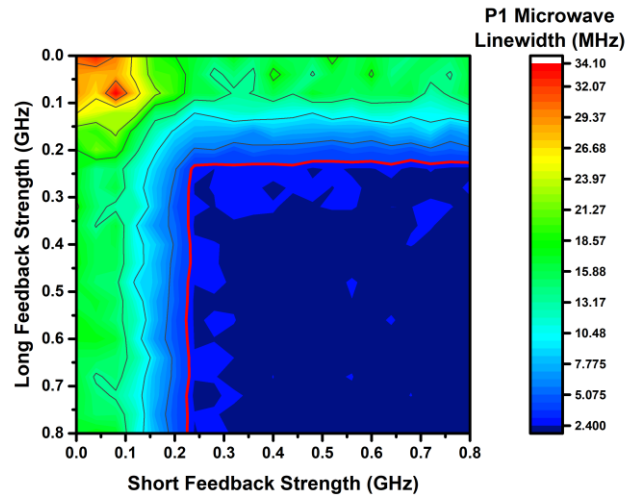


**Figure 4.14** Map of the P1 microwave linewidth under injection condition of  $(\eta_y, \nu_{inj}) = (20GHz, +10GHz)$  and with double optical feedback.

Figure 4.14 is the map of the P1 microwave linewidth. The x, y axis is the feedback strength for the short-cavity feedback-and the long cavity feedback in step of  $0.1\text{GHz}$ . The linewidth of the P1 microwave varies from  $32\text{MHz}$  to  $1\text{MHz}$ . The low linewidth reduction is occupied in the top left corner area, which the both feedbacks are at its low feedback strength. The large dark blue area enclosed by the red line represents the linewidth that is smaller than  $3.2\text{MHz}$ , it occurs when the combined total feedback strength is over  $0.5\text{GHz}$ . We denote this enclosed area as the good linewidth area. Interestingly, the effect of the total feedback strength on the linewidth reduction qualitatively agrees with the single feedback setup situation, in other words, the linewidth reduction in our setups is mostly related to the total feedback strength the laser received, regardless of single or double feedback setup.

### Side Peaks Suppression

The previous section only discussed the microwave quality by its linewidth, however, , the side peaks of the P1 microwave are often observed in the power spectra of both experimental and numerical results. In this section, a second feedback is added in order to suppress the side peaks. In the simulation, the same injection parameters  $(\eta_y, \nu_{inj})$  of  $(20\text{GHz}, +10\text{GHz})$  used in Figure 4.13(a) are adopted and the experimental feedback delay times of  $(5.1\text{ ns}, 7.3\text{ ns})$  are applied as the delay times of the short feedback cavity and the long feedback cavity..

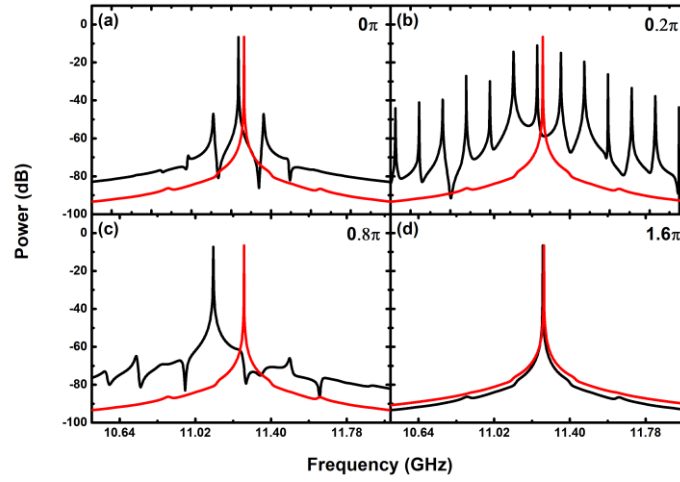


**Figure 4.15 Numerical simulation of RF spectra of the VCSEL with single feedback (black curve) and double feedback (red curve). Feedback phase  $\varphi$  from the short cavity (a)  $0\pi$ ; (b)  $0.2\pi$ ; (c)  $0.8\pi$ ; (d)  $1.6\pi$ .**

In Figure 4.15, the black curves represent only the short-cavity feedback were enabled with  $1.2\text{GHz}$  feedback strength, while the red curves are representing the both short and long cavity feedback were enabled with each feedback strength being  $0.6\text{GHz}$ , to keep the total feedback strength to be the same. Figure 4.15(a) shows the power spectra of the VCSEL with in-phase optical feedback. Under the short-cavity feedback only condition, MSPR of  $41.57\text{dB}$  is obtained. After a second long-cavity feedback is added, the side peaks are totally disappeared. While adding the second feedback, the microwave frequency increases slightly by  $23\text{MHz}$ . The side peaks are most prominent at  $0.2\pi$  phase variation under a single short-cavity feedback enabled condition, as shown in Figure 4.15(b). Similarly, the side peaks are suppressed with a small microwave frequency shift of  $18\text{MHz}$ . In Figure 4.15(c) a very good side peak suppression can be observed under phase variation being  $0.8\pi$  with a single feedback. A larger microwave frequency shift of  $160\text{MHz}$  is presented for double feedback. Moving to  $1.6\pi$  phase variation in Figure 4.15(d), no side peak appears in both single and double feedback configurations.

The above Figure 4.15 only showed the results that the both short and long feedbacks are in equal feedback strength. To extend the study of the second feedback interacting with the P1 microwave, we investigate the cases that the both feedback strengths are not equal. In Figure 4.16, the black curve representing only the short-cavity feedback enabled situation, while the red curves are for both feedbacks enabled case. The short-cavity feedback strengths are fixed at 0.6GHz. The phase variation for it is fixed at  $0.2\pi$  to represent the “worst” multiple side peaks incidence.

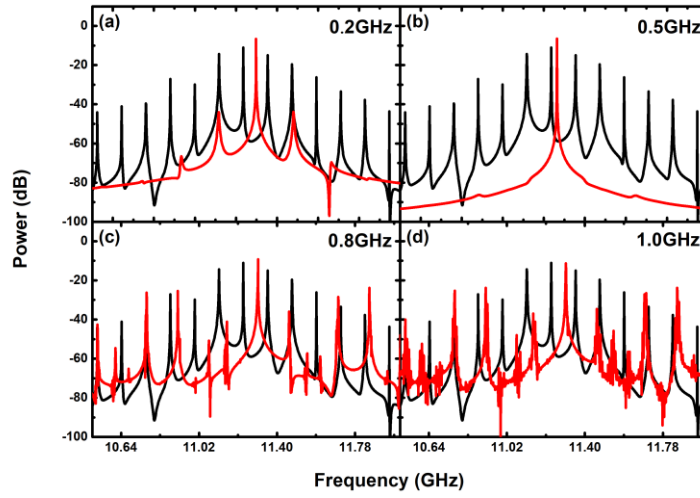


**Figure 4.16 Numerical simulation of RF spectra of the VCSEL with the single feedback (black curve) and the double feedback (red curve). The long cavity feedback strength equals to (a) 0.2GHz, (b)0.5GHz, (c) 0.8GHz and (d) 1.0GHz, while maintaining the short feedback strength at 0.6GHz.**

Figure 4.16 shows the numerical results of the RF spectra of the VCSEL with the single feedback (black curve) and the double feedback (red curve). When the long cavity feedback strength is set at 0.2 GHz, the MSPR has improved significantly, as shown in Figure 4.16(a). When the second feedback strength increases to 0.5GHz, the side peaks have been totally suppressed. Further increase the second feedback strength to 0.8GHz, the side peaks do not be eliminated, but the dynamics of the VCSEL being driven out P1 dynamic. Figure 4.16(d) shows that the VCSEL operates at more unstable dynamic when the second feedback strength is increased to 1.0 GHz. It is clear that only Figure 4.16(b) have a good MSPR suppression. For all other situations, adding the second long-feedback cannot guarantee a good suppression. In examples of Figure



4.16(c) and (d), extra unevenly spaced side peaks are raised, and the P1 microwave is further destabilized. The effects of the two feedback strengths on the P1 microwave side peaks are summarized in Figure 4.17.

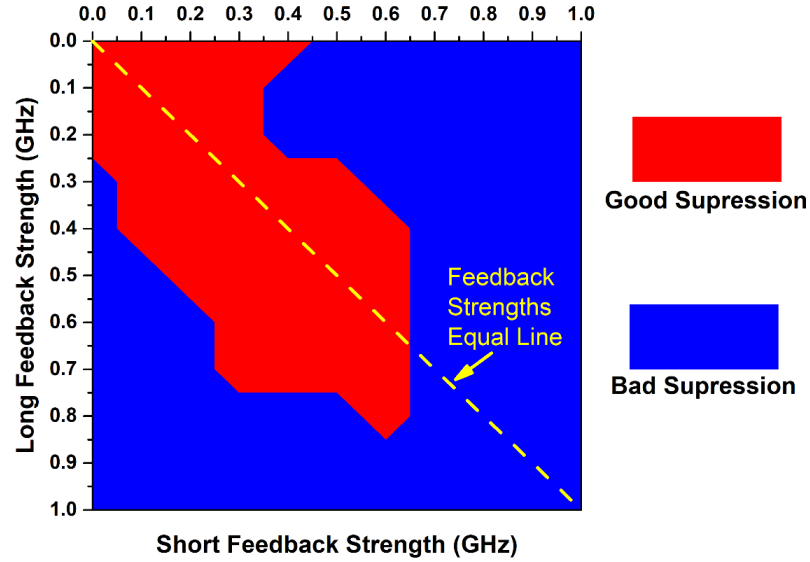


**Figure 4.17 Mapping of the side peak suppression behaviors.**

For the convenience purpose, we refer that over  $50\text{dB}$  suppression on MSPR as good suppression, lower than  $50\text{dB}$  of MSPR suppression as bad suppression. In Figure 4.17, both short and long feedback strength is varied from 0 to  $1.0\text{GHz}$  with a step of  $0.1\text{GHz}$ . The short cavity feedback's phase variation is fixed at  $0.2\pi$  while the long feedback is kept in-phase. From the map, we can observe that the good suppression area is in general expanding along the "line" that the both feedback strengths are equal but not infinitely extended. Rather than suppress the side peaks, high feedback strengths can drive the dynamic of the VCSEL out of P1 dynamic. This result agrees with our experimental observation..

### Double Feedback Discussion

To have an insight into how the linewidth reduction and side peak suppression by the double optical feedback technique, we plot the previous Figure 4.14 and Figure 4.17 together and created Figure 4.18. We also converted the linewidth reduction to log scale to better observe the linewidth reduction affected by the optical feedback. In Figure 4.18 the color bar is defined as:

$$\text{Linewidth Reduction} = 10 * \log_{10}\left(\frac{\text{Original Linewidth}}{\text{Current Linewidth}}\right) \quad (4.5)$$

Where the original linewidth being  $30.6\text{MHz}$  when no feedback strength added.

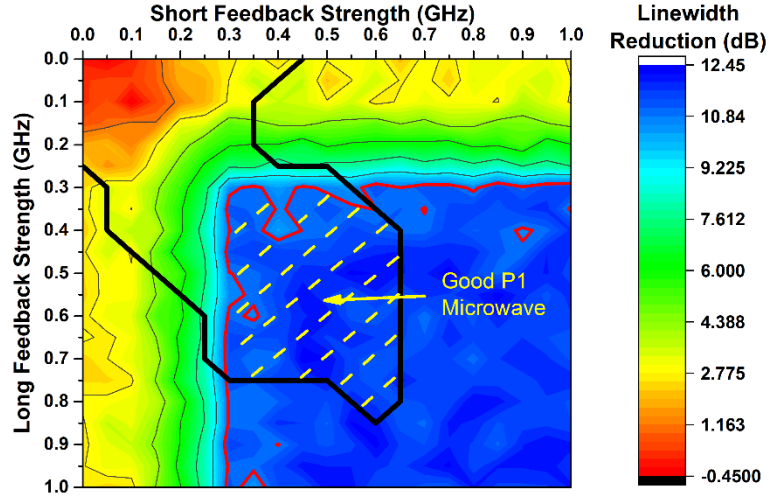


**Figure 4.18 Mapping of the “good” P1 microwave by double optical feedback setup.**

In Figure 4.18, the area of the over  $10\text{dB}$  linewidth reduction is enclosed by the red line, the good side peaks suppression area is enclosed by the black line. The overlapping area is marked as “Good P1 Microwave” and covered by the yellow dash line. From this overlapping area, we can see that only a relatively small subset of the mapp can be considered as the double feedback setup improves the quality of the generated P1 microwave by reducing the microwave linewidth at same time reduce its MSPR.

## 4.5 Chapter Summary

In this chapter, we have studied the effect of optical feedback effect on the linewidth and stability of the generated photonic microwave based on P1 dynamics in an optically injected single-mode VCSEL. The results show that both single feedback and double feedback can reduce the linewidth. However, the feedback phase in the single feedback configuration must be carefully adjusted to suppress the side peaks. The linewidth in the double feedback configuration can, with optimal feedback phase, be reduced to less than one-tenth of linewidth without the optical feedback. We also investigate the stability of photonic microwave, which is quantified by measuring the microwave frequency range using a long sweep time of the radio frequency spectrum analyzer. The results indicate that optical feedback techniques can also improve the stability of the generated microwave.

Numerical simulation confirms that the linewidth reduction is mostly depended on the total feedback strength the VCSEL received. However, increasing the feedback strength does not infinitely reduce the linewidth, in contrast, very high feedback strength may reduce the quality of the P1 microwave or even drive the VCSEL into more complex dynamics. The rationale of adding the second feedback is to improve the P1 microwave's quality by suppressing its side peaks caused by laser's external cavity modes. A map of the P1 microwave quality affected by double optical feedback is also created, which provides a guidance for setting the feedback strength for improving P1 microwave quality through optical feedback techniques..

# 5 Effect of Bias Current on Complexity and Time Delay Signature of Chaos

## 5.1 Chapter Introduction

Optical chaos has many potential applications as we have introduced in the Literature Review chapter. One of the key laser's parameters, the bias current, affects the behavior of the optical chaos drastically. Examination of the effect of the bias current on bandwidth, TD signature and complexity of chaos have been reported in some papers. However, to the best of our knowledge, the influence of bias current on the relationship between complexity and TD signature has not been experimentally investigated in detail. In this chapter, we experimentally and theoretically research the effect of bias current on the complexity and TD signature with the different feedback strengths in semiconductor lasers subject to polarization preserved optical feedback. In addition, we have found 'abnormal' complexity behaviors of chaos with the changing bias current, the different vertical resolution in data acquisition are attributed to this 'abnormal' behaviors. We proposed a method to minimize such effect before we discuss the experimental results.

## 5.2 Experimental Setup and Data Acquisition

Two experimental setups are used in this investigation. The first experiment was carried out in a free-space setup, as shown in Figure 5.1(a). A single mode Fabry-Perot laser (APL 860-40) with lasing wavelength around  $860nm$  was used in the experiment. The laser was driven by an ultra-low noise current source and its temperature was controlled to an accuracy of  $0.01\text{ Celsius}$ . At the operating temperature, the threshold current is  $37.3mA$ . The laser was subject to the optical feedback from mirror M1. The feedback power was controllable with a natural density filter (ND1). The feedback round trip time was about  $5.6ns$ . An optical isolator (ISO) was used to prevent any unwanted feedback from the detection path. The output of the

laser was detected by  $12\text{GHz}$  photodetectors and recorded by a  $4\text{GHz}$  digital oscilloscope and a  $30\text{GHz}$  bandwidth RF spectrum analyzer. The sampling rate of the oscilloscope was set at  $10\text{GS/s}$  and  $1000000$  samples were recorded for each time trace, therefore the duration of each time trace was  $100\mu\text{s}$ .

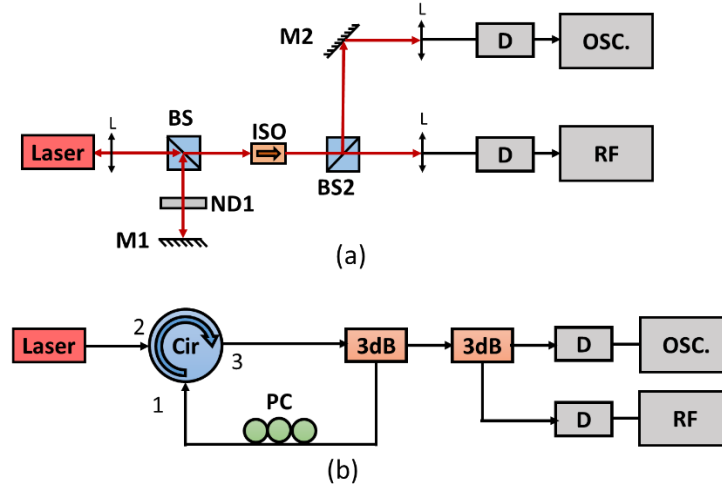


**Figure 5.1 (a) Free space experimental setup, (b) all-fiber experimental setup.**

**L: Lens; BS: beam splitter; M- mirror; ND: neutral density filter; ISO: optical isolator; D: detector; OSC: oscilloscope; RF: radio frequency spectrum analyzer; Cir: optical circulator; 3dB: 3dB optical coupler; PC: polarization controller. Red lines represent the laser beam travel in free space. Black lines represent the laser beams travel in the optical fiber.**

The second experiment was performed in an all-fiber setup, as shown in Figure 5.1(b). A single-mode Fabry-Perot laser from Eblana Photonics with lasing wavelength around  $1.55\mu\text{m}$  was used in the experiment. At the operating temperature, the threshold current is  $14.7\text{mA}$ . The laser was subject to optical feedback from the fiber loop. The polarization controller in the fiber loop was used to ensure polarization preserved optical feedback. The feedback round-trip time is about  $42.6\text{ns}$ . The detection method for the output of the laser was the same as that in the free space experiment. In this chapter, the feedback ratio is defined as the ratio of the optical feedback power to the laser's free-running output power. The optical feedback power is measured just before it is fed back into the laser.

### 5.3 Digital Acquisition Methods Discussion

As we discussed in Section 2.2.2 (page 27), the complexity of chaos is one of the important parameters for assessing the suitability of chaos for its applications. The method of choice as a quantifier to measure the relative complexity is the permutation entropy (PE) due to its advantages such as, easy implementation, faster computation and being robust to noise. These advantages make PE particularly attractive on analyzing experimental chaotic data. However, the value of PE can be affected by many factors, for example, the selection of subset dimension in the calculation, the sample rate, delay time and the total number of points in the time series [77], [100], [173]–[175]. The minimum required sampling rate to capture all the information of the fast chaotic dynamics decreases when the embedding dimension increases [175]. A brief description of the effect of the acquisition conditions on random bit generation has also been reported [176], [177]. Using the value of PE at the delayed time equal to the external cavity round trip time to quantify the complexity of chaos agrees with the definition of weak or strong chaos [100]. In this Section, we discuss the effect of the digital acquisition on quantifying the complexity of chaos using the value of PE at the feedback delay time. In the experiment, ‘abnormal’ variations of complexity with the bias current are observed. We use both experimental and numerical methods to analyze this ‘abnormal’ phenomenon. We also provide a method to minimize this ‘abnormal’ condition.

#### 5.3.1 Experimental method

To demonstrate the effect of the digital acquisition on the complexity of chaos, we have used the all-fiber experimental setup in Figure 5.1(b). Figure 5.2(a) shows the time traces of chaos generated in the laser diode. The red line is the noise floor from the stable operation laser. The output of the laser shows large amplitude fluctuation, which indicates that the laser was operating in a chaotic region. The normalized  $PE(H(P))$  as a function of embedding delay time was calculated and displayed in Figure 5.2(b). The details of the normalized PE definition can be found in Section 2.2.2. The length of the ordinal pattern in this paper was chosen as 4. It is obvious that there are troughs around the feedback round trip time ( $\tau_{ext}$ ) of 42.6 ns and its subharmonics. As indicated in the introduction, this trough value at the feedback round time can be used

to measure the complexity of chaos [44], [100], and we adopt it to characterize the complexity of chaos. It is noted that the trough may not be located exactly at  $\tau_{ext}$  [100]. If a measured trough value is in the range of interval of  $(\tau_{ext} - \tau_{ext} \times r_1, \tau_{ext} + \tau_{ext} \times r_1)$ , it will be considered as the trough at  $\tau_{ext}$ . According to the experimental data, 2% is selected as the value of  $r_1$ .

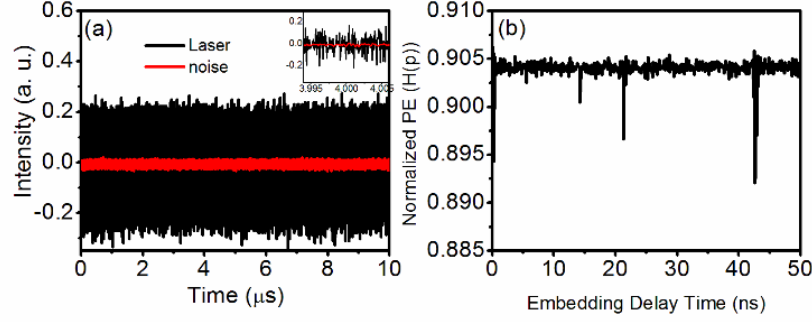


**Figure 5.2 (a) The time trace of the laser output and (b) the normalized PE as a function of embedding delay time. The inset in (a) is the time series in a shorter time interval.**

Figure 5.3 shows the complexity of chaotic signals as a function of the laser bias current. For bias currents above  $23\text{mA}$ , the complexity is almost constant and varies smoothly. However, at lower bias currents, there are two ‘abnormal’ areas, where the complexity drops abruptly when the bias current increases both from  $17.5\text{mA}$  to  $18\text{mA}$  and from  $20.5\text{mA}$  to  $21\text{mA}$ , respectively. In order to investigate these ‘abnormal’ phenomena, the data acquisition condition was checked carefully. We found that the fluctuation amplitude increases with the increasing bias current. At the ‘abnormal’ regions, the vertical scale of the oscilloscope was increased to prevent high amplitudes from being saturated.

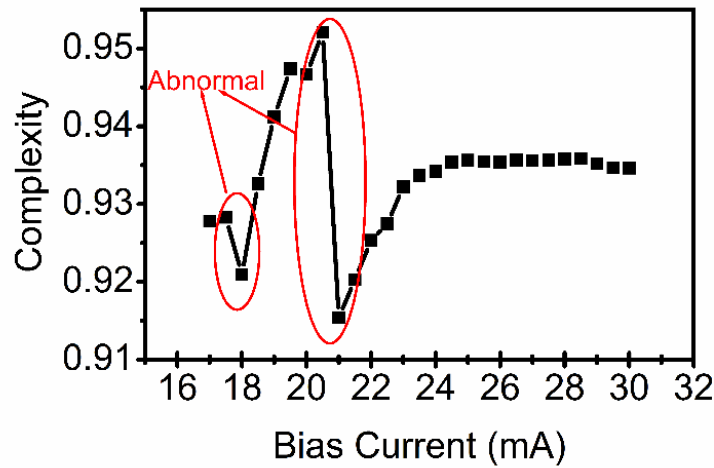


**Figure 5.3** The complexity of the chaotic signal as a function of bias current.

In order to prevent the change of the vertical scale of the oscilloscope, two approaches were adopted to record the data. Firstly, the output of the laser was coupled into the detector without changing the attenuation and the vertical scale of the oscilloscope. The vertical scale was set in such a way that the maximum fluctuation amplitude would not exceed the scale of the oscilloscope. The complexity of chaos with the increasing bias current was calculated, and the result is shown in Figure 5.4(a). The result shows that the complexity of chaos is almost monotonically increasing with increasing bias current. The sudden drop of complexity has not been observed. In the second method of data acquisition, the vertical scale of the oscilloscope was kept unchanged, but the amplitude of the signal was adjusted by an optical attenuator to ensure the amplitude of the signal can use the full-8-bit vertical resolution range of the oscilloscope. Under this data acquisition condition, the results obtained are illustrated in Figure 5.4(b). We can see the complexity increases with the increasing bias current for lower bias currents ( $< 22mA$ ). When the bias current is above  $22mA$ , the complexity shows saturation, and the bias current has little effect on the complexity. The two ‘abnormal’ variations of the complexity have also disappeared.



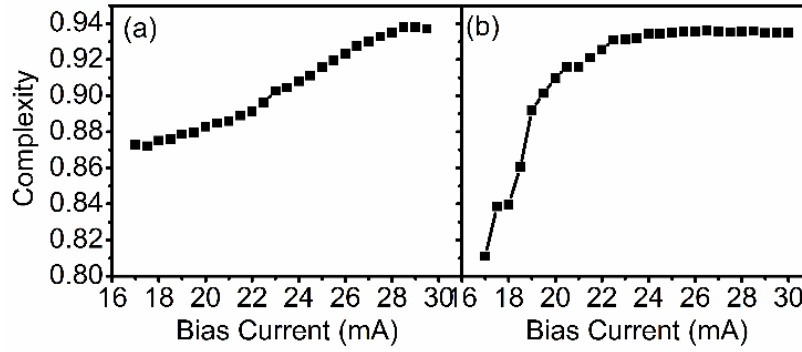


**Figure 5.4 The complexity of the chaotic signal as a function of bias current under a fixed vertical scale of the oscilloscope. (a) No optical attenuator before the detector, (b) with optical attenuator before the detector.**

### 5.3.2 Simulation Method

From the above results, we can see that three different results were obtained when the three different data acquisition methods were used. In order to identify which results are the true characteristics of chaos, chaos generated in semiconductor lasers with optical feedback have been numerically simulated using the Lang Kobayashi laser equations[78], as shown in Equation (5.1) and Equation (5.2) below.

$$\frac{dE}{dt} = \frac{1}{2}(1 + i\alpha) \left[ G - \frac{1}{\tau_p} \right] E(t) + \kappa E(t - \tau_{ext}) e^{-i\omega\tau_{ext}} \quad (5.1)$$

$$\frac{dN}{dt} = \frac{I}{eV} - \frac{N(t)}{\tau_N} - G|E(t)|^2 \quad (5.2)$$

In the rate equations,  $E(t)$  is the complex electric field,  $N(t)$  is the carrier density.  $\alpha$  is the line-width enhanced factor,  $\kappa$  is the feedback strength,  $\tau_p$  is the photon lifetime,  $\tau_N$  is the carrier lifetime,  $\tau_{ext}$  is the external cavity round-trip time,  $\omega$  is the angular frequency of the laser,  $V$  is the volume of the active region,  $e$  is the electron charge and  $I$  is the laser bias current. The optical gain  $G$  is given by Equation (5.3):

$$G = g_0(N - N_0) \frac{1}{1 + \epsilon|E(t)|^2} \quad (5.3)$$

where  $g_0$  is the differential gain,  $\epsilon$  is the gain saturation factor, and  $N_0$  is the carrier density at transparency.

In the simulation, the following parameter values are chosen:  $\alpha = 3$ ,  $\tau_p = 2ps$ ,  $\tau_N = 2ns$ ,  $\omega = 1.216 \times 10^{15} rad/s$  (which correspond to a lasing wavelength of  $1.55\mu m$ ),  $V = 1.225 \times 10^3 m^3$ ,  $g_0 = 5.0 \times 10^{-12} m^3 s^{-1}$ ,  $\epsilon = 5 \times 10^{-23}$  and  $N_0 = 1.4 \times 10^{24} m^{-3}$ . The laser's threshold current of  $14.7mA$  is obtained from the above parameters, which is the same as the threshold current of the laser we used in the experiment. According to the relationship between feedback ratio measured in the experiment and the feedback strength in the simulation [178],  $\kappa = 40ns^{-1}$  is selected to represent the feedback ratio in the experiment. At this feedback strength, the time series is similar to that in Figure 5.2(a), where the laser operates at chaotic dynamics. In the simulation,  $1ns$  is taken for  $\tau_{ext}$  to save the simulation time. The relaxation oscillation frequencies of the laser for all the operating bias currents are above  $3GHz$ , so  $1ns$  feedback round trip time is considered as long-cavity feedback case [179]. Our recent work has shown that the feedback round trip time has little effect on the trend of complexity for long cavity feedback [180]. The complexity of the laser chaotic output has been analyzed using the time series calculated from the above rate equations with a temporal resolution of  $\Delta t$  of  $10ps$  and the result is shown in Figure 5.5. The curve clearly shows that the complexity increases in line with the bias current for bias currents below  $23mA$ . When the bias currents are above  $23mA$ , slight variation of the complexity with the bias current have been displayed with no trend towards one way or another. This result is qualitative in good agreement with the experimental result showed in Figure 5.4(b).

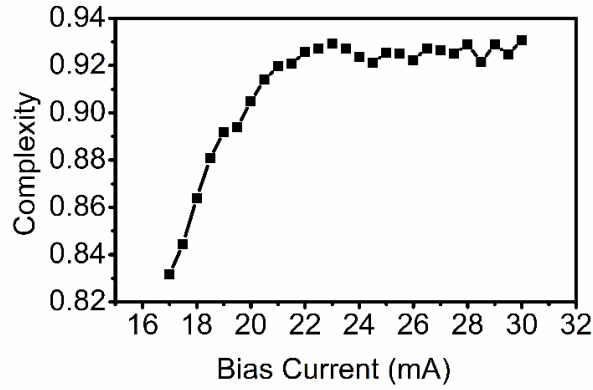


**Figure 5.5 Numerical simulation of the complexity as a function of bias current.**

Effect of the vertical resolution of the oscilloscope on the value of the complexity is further analysed. A time series calculated from the rate equations with the bias current of  $25\text{mA}$  was used. Figure 5.6(a) shows the complexity obtained from this time series. The result shows that the value of the complexity is close to 1 for most of the embedding delay time except at the feedback round trip time of  $1\text{ns}$  and its sub-harmonics. When the data is recorded in an oscilloscope in the experiment, the analogue chaotic signal is converted into a digital signal. Currently, the common vertical resolution of the oscilloscope is 8-bit. If the amplitude of chaos signal covers the full 8-bit range of the oscilloscope, the chaotic signal will be digitized to 255 ( $2^8 - 1$ ) levels between the maximum and minimum amplitude. In Figure 5.6(b), we calculate the complexity from the same time series used in Figure 5.6(a), but the data has been digitized to 255 levels. It is noted that the variation trend of the normalized PE with the embedding delay time is the same as that in Figure 5.6(a), but all its values have been reduced by 3%. In the experiment, the vertical-scale may need to be changed to avoid the amplitude of the chaotic signal being saturated. Here we can consider a simple case, where the maximum amplitude is about to exceed the full 8-bit range of the oscilloscope and the vertical scale of the oscilloscope is increased by a factor of 2. In such a case, the values between the maximum and minimum can be digitized to 127 ( $2^7 - 1$ ) levels. Figure 5.6(c) shows the calculation result, where the same time series in Figure 5.6(a) is digitized to 127 levels instead of 255 levels. We can see a similar trend of the

normalized PE as a function of embedding delay time achieved, but with the absolute values further reduced by another 3%. This result explains why the complexity decreases dramatically at the bias currents between  $18mA$  and  $21mA$  when the vertical scale of the oscilloscope is increased in the experiment.

Figure 5.6(d), the amplitude of the time series used in Figure 5.6(a) is reduced to its half value, but this time series is still digitized to 255 levels. This is similar to the case that the vertical scale of the oscilloscope is adjusted to guarantee the signal takes up the full 8-bit range but without surpassing it when an optical attenuator is used to reduce the signal power. The complexity of this time series is calculated. We can see that the result is the same as that in Figure 5.6(b). This indicates that the absolute power would not influence the normalized PE value, but the data's digitization will affect its results. The reason for this phenomenon is that PE is a method based on the relative amplitude of time series value, not the absolute value.

Two minima separated by half inverse the relaxation oscillation frequency ( $1/(2f_{RO})$ ) near  $\tau_{ext}$  [175], [177] are not obvious in Figure 5.6 and Figure 5.2(b). It may due to lower bandwidth (4GHz) oscilloscope for Figure 5.2(b). Lower bandwidth oscilloscope causes the loss of the dynamics at frequencies close to  $f_{RO}$ . For the simulation results in Figure 5.6, lower length of the ordinal pattern for PE calculation may be attribute to less significant of the signature of  $f_{RO}$ . It is interesting to see that the signature of  $f_{RO}$  near  $\tau_{ext}$  becomes clearer for less digitized levels, as indicated by an arrow in Figure 5.6(c). This phenomenon is outside the scope of this thesis and will be investigated in the future study. Figure 5.6 also shows that the maximum normalised PE value (the “flat” value) decreases with decreased digitisation levels, whereas the trough depth of the normalized PE at  $\tau_{ext}$  increases at the same time.

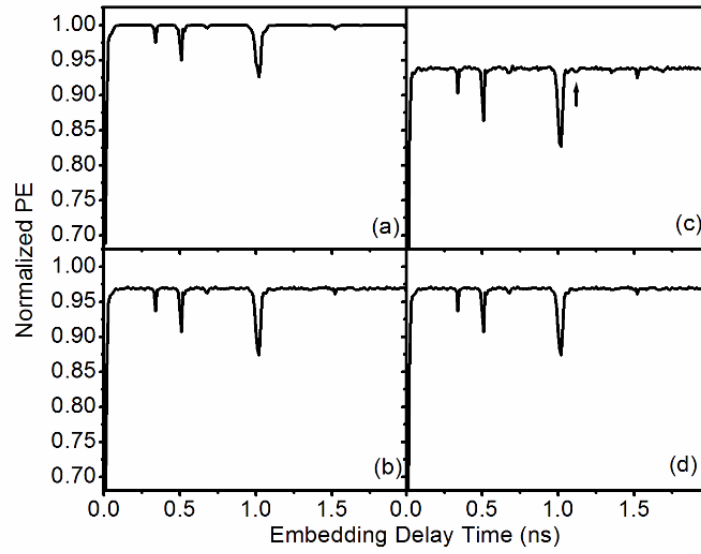


**Figure 5.6** The normalized PE calculated from (a) the time series calculated from the rate equations; (b) the time series being digitized to 255 levels; (c) the time series being digitized to 127 levels; (d) the time series whose amplitude has been reduced by half and digitized to 255 levels.

To better show the effect of digital acquisition on the normalized PE, the normalized PE at  $\tau_{ext}$ , the average normalized PE and the trough depth at  $\tau_{ext}$  of the time series used in Figure 5.6(a) as a function of digitized levels are plotted in Figure 5.7. This is analogous to the scenario that the same time series is being recorded by an oscilloscope using a different vertical scale. The average PE is the average value of the normalized PE for the embedding delay time between  $1.2ns$  and  $1.4ns$ , which corresponds to the maximum normalized PE value (the “flat” value). The trough depth at  $\tau_{ext}$  is defined as the difference between the average normalized PE and the normalized PE at  $\tau_{ext}$ . The result exhibits that both the normalized PE at  $\tau_{ext}$ , and the average normalized PE increase monotonically with increased digitized levels, but the increase rate for the normalized PE at  $\tau_{ext}$  is slightly faster than that of the average normalized PE, therefore the trough depth at  $\tau_{ext}$  decreases with the increased digitized levels. The results in Figure 5.7 prove that the data acquisition should cover the full vertical resolution of the oscilloscope to reduce the degradation of the complexity of

chaos signal, as recommended in [78], [177]. For the comparison of complexity of chaos using PE, all data should use the same digitized levels.

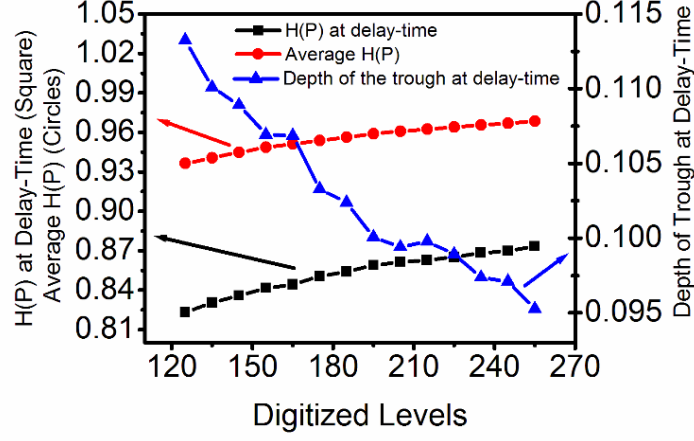


**Figure 5.7 Numerical simulation effect of the digitized levels on the average normalized PE (circles), the normalized PE at  $\tau_{ext}$  (squares) and the depth of the trough at  $\tau_{ext}$  (triangles) as a function of digitized levels.**

## 5.4 Experimental Result

Now we have minimized the unwanted effect of digital acquisition on complexity of chaos by the methods presented above, we will begin to discuss the effect of bias current on complexity and time delay signature of Chaos. Figure 5.8 shows the time traces, power spectra, autocorrelation functions and permutation entropy of the output of the laser subject to  $-10.2$  dB optical feedback at the bias current of  $50$  mA,  $60$  mA and  $70$  mA in the free-space experimental setup. The time series in Figure 5.8(a1), (a2) and (a3) show the fluctuations of the output amplitudes, which indicates that the laser is in chaos dynamics. The second column in Figure 5.8 shows the power spectra of the laser output. The results demonstrate that the bandwidth of chaos increases with increasing bias current. This is easy to understand, since the bandwidth of chaos is dependent on the laser's relaxation oscillation (RO) frequency and the RO frequency is proportional to the square root of the difference between the bias current

and the threshold current. The third column of Figure 5.8 displays the AC coefficient as a function of the delay time. In the results, the AC coefficients has a peak at around  $5.6\text{ns}$ , which equals the feedback round trip time. The TD signature of chaos can be quantified by measuring the AC peak value at the feedback round trip time[43], [95], [181], [182]. Figure 5.8(c1) shows that the AC peak value is 0.74 for the bias current of  $50\text{mA}$ . When the bias current increases to  $60\text{mA}$ , the AC peak value decreases to 0.72. If the bias current is further increased to  $70\text{mA}$ , the AC peak value decreases to 0.65. The fourth column of Figure 5.8 represents the normalized  $PE$  ( $H(p)$ ) drawn against the embedding delay time. There are troughs at the feedback round trip time and its subharmonics for all three bias currents. The trough value at the feedback round time is adopted to be used to measure the complexity of chaos [32]. Figure 5.8(d1) shows a deep trough at  $5.6\text{ns}$ , where the value is 0.7. When the bias current increases to  $60\text{mA}$ , the depth of trough at delay time increases to 0.8. Further increasing the bias current to  $70\text{mA}$ , the depth of trough increases again to 0.86.

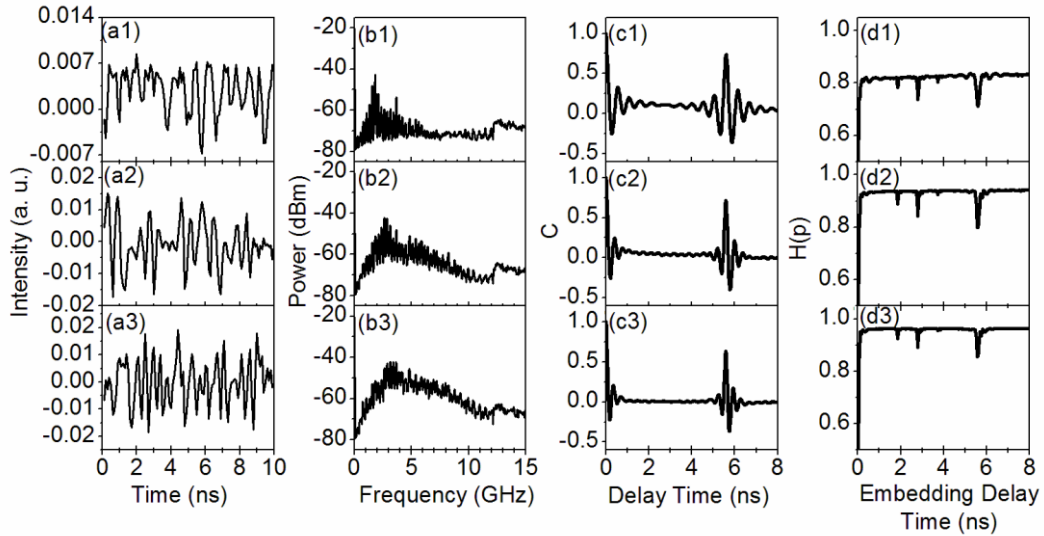


**Figure 5.8** The time traces (first column), RF power spectra (second column autocorrelation coefficient curves (third column) and permutation entropy curves (fourth column)) of the chaotic signal. The top, middle and bottom rows represent bias currents of  $50\text{mA}$ ,  $60\text{mA}$  and  $70\text{mA}$ , respectively.

The results in Figure 5.8 show that the values of bandwidth, TD signature and complexity of chaos with the same feedback ratio are sensitive to the bias current. The TD signature and complexity as a function of the normalized bias current with the same feedback strength used in Figure 5.8 are calculated and shown in Figure 5.9(a). The bias current has been normalized with the threshold current. In Figure 5.9(a), a minimum TD signature has been observed at the highest bias current being measured. The complexity almost linearly increases with increasing bias current. The TD signature and complexity show an inverse relationship for most normalized bias currents except the kink at the normalized bias current between 1.55 and 1.69. The inverse relationship between the TD signature and complexity is in good agreement with the simulation result [183].

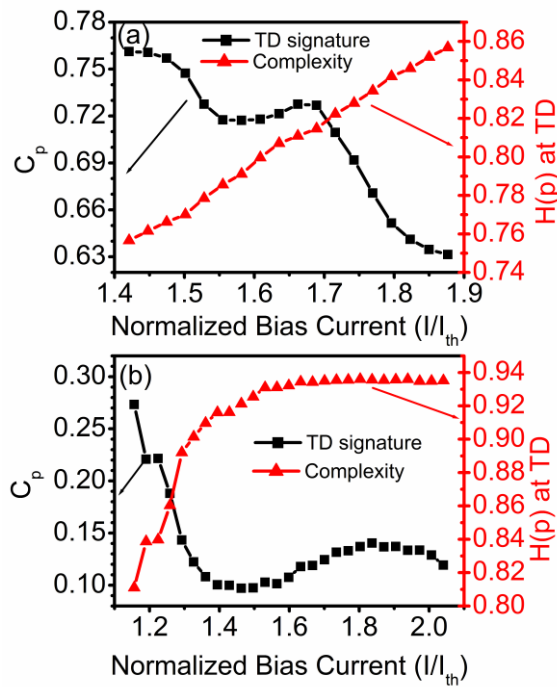


**Figure 5.9 The TD signature and complexity of chaos as a function of the normalized bias currents in (a) the free space experimental setup, (b) the all-fiber experimental setup.**



We have also performed the experiment in an all-fiber setup, as shown in Figure 5.1(b). When the feedback ratio was adjusted to about  $-14.3\text{dB}$ , the laser was in chaos dynamics. The TD and complexity of chaos with various bias currents were calculated and plotted in Figure 5.9(b). The results show that the TD signature decreases with increasing bias current at the very beginning. When the normalized bias current reaches 1.4, a minimum TD signature is obtained. If the bias current is further increased, the TD signature will increase again. For normalized bias currents between 1.8 and 1.9, the TD signatures do not change much with the local maximum TD signature obtained. When the normalized bias current is tuned to more than 1.9, the TD signature starts to drop again. The complexity of chaos, on the other hand, initially increases with bias current until the normalized bias current reaches 1.6. After that the complexity of chaos starts to saturate at 0.93. It is clear that the complexity has an inverse relationship with the TD signature for lower bias currents, however, the inverse relationship disappears after the normalized bias current reaches 1.4.

## 5.5 Simulation Result

In order to understand the difference between Figure 5.9(a) and (b), nonlinear dynamics of semiconductor lasers with optical feedback have been numerically simulated using the Lang Kobayashi laser equations [78], as shown in Equation **Error! Reference source not found.** and **Error! Reference source not found.**

MATLAB solver dde23 was used to numerically solve Equation 5.1) and **Error! Reference source not found.**5.2) with a temporal resolution of  $10\text{ps}$ . Typical semiconductor laser's parameters:  $\alpha = 3.0$ ,  $\tau_N = 2\text{ns}$ ,  $\tau_p = 2\text{ps}$ ,  $g_0 = 5 \times 10^{-12} \text{ m}^3 \text{ s}^{-1}$ ,  $N_0 = 1.5 \times 10^{24} \text{ m}^3$  and  $V = 2.9 \times 10^{-16} \text{ m}^3$  were chosen in the simulation. The laser's lasing wavelength was set at  $860\text{nm}$ , threshold current  $I_{th} = 37.3\text{mA}$  and  $\tau_{ext} = 5.6\text{ns}$ , which corresponds to our free-space experimental setup. The duration of the time series is  $1\mu\text{s}$ . When the feedback strength  $\kappa$  is set to  $60\text{ns}^{-1}$ , the laser operated at chaotic dynamics for the normalized bias current range from 1.05 to 2.0. The TD signature and complexity of chaos have been calculated and shown in Figure 5.10(a). The TD signature shows an almost linear decrease with increasing bias current until the normalized bias current reaches 1.9. Further increasing the bias current, the TD signature is almost unchanged. Figure 5.10(a) also shows that the

complexity increases monotonically with increasing bias current until the normalized bias current reaches 1.75. Further increasing the bias current, the complexity is almost unchanged. The results in Figure 5.10(a) show that the complexity is approximately in inverse relationship with the TD signature, which is qualitatively agreed with the experimental results in Figure 5.9(a). However, there is no kink for the TD signature in the simulation results. Also, the complexity does not linearly increase with increasing bias current. More investigation should be done to explore the fundamental difference between experimental and theoretical results.

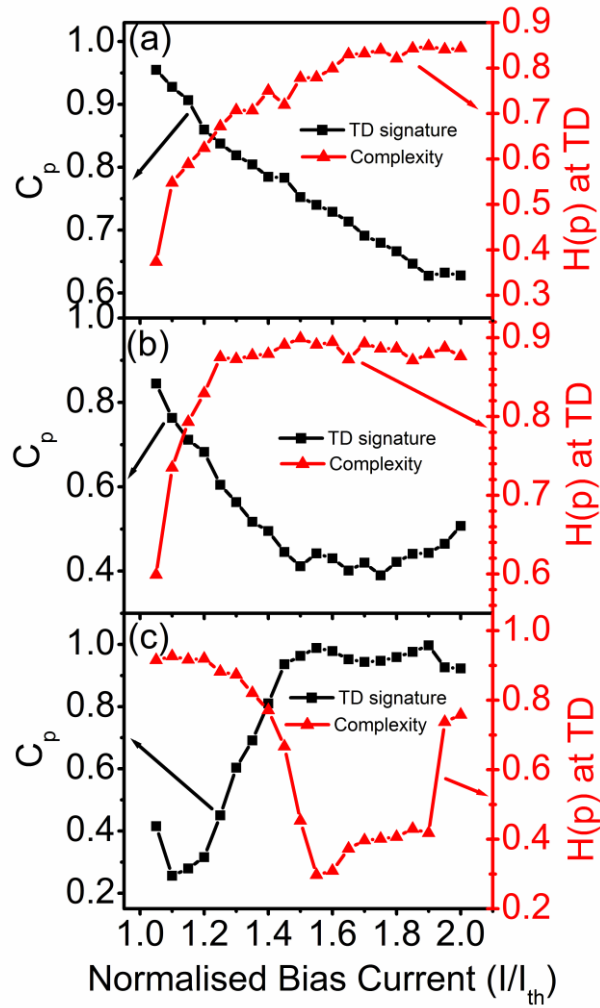


**Figure 5.10** Numerical results of the TD signature and complexity as a function of the normalized bias currents with a feedback strength of (a)  $60\text{ns}^{-1}$ , (b)  $30\text{ns}^{-1}$ , (c)  $9.32\text{ns}^{-1}$ .

When the feedback strength  $\kappa$  is reduced to  $30\text{ns}^{-1}$ , and the other parameters kept the same as those in Figure 5.10(a), the laser still operated at chaotic dynamics for the normalized bias current range from 1.05 to 2.0. Its TD signature and complexity as a function of the bias current are displayed in Figure 5.10(b). The trend of the curves are different from those in Figure 5.10(a). The TD signature decreases initially. When the normalized bias current reaches about 1.5, the TD signature starts to saturate. When the normalized bias current increases to more than 1.75, The TD signature begins to increase. On the other hand, complexity increases with increasing bias current for the

normalized bias current below 1.25. After that, the complexity shows saturation, and the bias current has little effect on the complexity. These results agree well with those in Figure 5.9(b) except that an extra dropping of TD signature at high bias current has been observed in the experiment.

When the feedback strength  $\kappa$  is further reduced to  $9.32ns^{-1}$ , the dependence of the TD signature and complexity on the bias current is illustrated in Figure 5.10(c). The curves are quite different compared with those in Figure 5.10(a) and (b). The TD signature decreases when the normalized bias current increases from 1.05 to 1.1. After that, the TD signature starts to increase quickly with increasing bias current until the normalized bias current reaches 1.45. After that, the bias current has much less effect on the TD signature. The variation of complexity is almost inverse to that of TD signature, but the change rates for the TD and complexity vary at different bias current regions. There is a sharp increase of complexity when the normalized bias current increases from 1.9 to 1.95. The reason for this sharp increase is due to very small fluctuation amplitude at the normalized bias current of 1.95, the laser is almost operated at steady-state.

During the experiments, we have used different wavelength lasers and different feedback round trip times to illustrate the effects. Here we have also introduced different wavelengths and feedback round trip times in the simulation. The results show that wavelength has little effect on the variation of the TD and complexity with the bias current. The feedback round trip time also has very little influence on the trend of the TD and complexity.

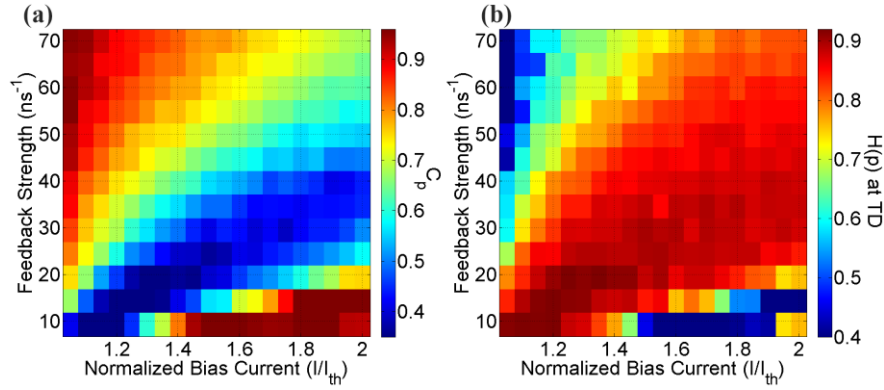


**Figure 5.11 Maps of (a) TD signature, (b) complexity of chaos with varying bias current and feedback strength.**

The maps of the TD signature and complexity with varying bias current and the feedback strength are presented in Figure 5.11. It can be seen in Figure 5.11(a) that lower TD signature has been achieved at lower bias current with lower feedback strength. With increasing feedback strength, the lowest TD signature shifts to higher bias current. Meanwhile, the lowest TD signature decreases with decreasing feedback strength. This map is somehow different from that in Ref. [176], where lower TD signature can be achieved over a much wider range of bias currents for higher feedback ratio. This difference may be due to polarization-rotated feedback in [176], while it is polarization preserved feedback in our study.

The trend of complexity in Figure 5.11(b) has some similarity with that of the TD signature in Figure 5.11(a). The highest complexity is obtained at a lower bias current and a lower feedback strength. For the feedback strength between  $15\text{ns}^{-1}$ , and  $25\text{ns}^{-1}$ , there is an optimum bias current, where the chaos is most complex. This result is similar to the simulation result in [183]. This optimum bias current moves to higher bias current with an increasing feedback strength. However, for the feedback strength between  $30\text{ns}^{-1}$ , and  $55\text{ns}^{-1}$ , there is a wider bias current region where the bias current has very little effect on the complexity compared to that on the TD signature.

## 5.6 Chapter Summary

The influence of bias current and the feedback strength on the complexity and time-delay signature of chaotic signals in semiconductor lasers with optical feedback has also been investigated experimentally and theoretically. The time-delay signature has an approximately inverse relationship to the complexity of chaos in the free space experimental setup. However, this inverse relationship disappears at the higher bias current in the all-fiber experimental setup. This disappearance is due to the decrease of feedback strength, as confirmed by the simulation results using the Lang Kobayashi laser equations. The numerical simulation results show that the TD signature has an inverse relationship to complexity for strong or low feedback strength. For intermediate feedback strength, an inverse relationship between TD signature and complexity only exists at lower bias currents, and the bias current has little effect on the complexity of chaos at higher bias currents. In the experiment, ‘abnormal’ variations of the complexity of chaos with bias current were observed. Such ‘abnormal’ variations are attributed to the change of data digitization resolution. The complexity increases with increased digitized levels. In order to reduce the degradation of the complexity of chaos signal, the data acquisition needs to cover the full vertical resolution of the oscilloscope. For the comparison of the complexity of chaos using PE, all data should be acquired using the same resolution of the digitization.

## 6 Conclusion

### 6.1 Summary

Photonic generation of stable microwave using the dynamics of an optically injected single-mode VCSEL is investigated. Firstly, continuously tunable photonic microwave generation based on P1 dynamics in an optically injected VCSEL is studied. The continuously tunable microwave frequency from  $4\text{GHz}$  to up to an instrumentation limited of  $15\text{GHz}$  was observed. The higher P1 microwave frequency can be obtained by further increasing the frequency detuning and injection power. The P1 microwave frequency increases with the increases of the frequency detuning and injection power. The influence of frequency detuning on the generated microwave power is varied, and it is depended on the excitation of both linear polarizations of the VCSEL. The second harmonic distortion (SHD) decreases with the frequency detuning for higher injection power. The injection power has little effect to the SHD. The simulation results verified the experimental result and provided the almost linear relationship between the linear dichroism and P1 microwave frequency. The linear birefringence of the VCSEL has no effect on the microwave frequency and has very little effect to the microwave power.

Secondly, the optical feedback effect on the linewidth and stability of the generated photonic microwave based on P1 dynamics in an optically injected single-mode VCSEL has been experimentally studied. Both single and double feedback configuration can reduce the linewidth of the generated P1 microwave. However, the single feedback setup can introduce the side peaks to the P1 microwave if the feedback phase is not adjusted carefully. The double feedback not only reduces the linewidth but also minimizes the side peaks. The numerical simulation results support the experimental linewidth reduction results. The simulation results indicate that both single and double feedback can reduce the linewidth and the linewidth reduction is mainly related to the total feedback strength. The second feedback can be used to suppress the side peaks. A map of P1 microwave quality affected by double optical feedback is also created, which will provide a guidance for setting the feedback strength for improving P1 microwave quality through optical feedback techniques.

In this thesis, effect of bias current on the relationship between complexity and TD signature of the chaotically oscillated semiconductor laser has also been theoretically and experimentally studied. The contribution of this thesis to the research area of laser's chaotical behavior is summarized as follows: The time-delay signature has an approximately inverse relationship to the complexity of chaos in the free space experimental setup. This behavior is not presented in the all-fiber setup at higher bias current situation. The numerical simulation results suggest that this difference may due to the different feedback strength. The numerical simulation results show that the TD signature has an inverse relationship to complexity for strong or low feedback strength. For intermediate feedback strength, an inverse relationship between TD signature and complexity only exists at lower bias currents, and the bias current has little effect on the complexity of chaos at higher bias currents.

## 6.2 Future Work

Building on this research, further investigation of the dynamical properties of semiconductor lasers can be conducted.

- In Chapter 3, the experimental result of microwave power mapping(Section 3.3.3 Page 54) showed two higher power areas. This is not always the case on other VCSELs we tested. It is pointed out that it is likely due to both polarizations excitation and it is depended on individual VCSEL internal parameters, more detailed reason can be investigated in future studies.
- In Chapter 4, compare to Chapter 3's numerical study, the numerical integration step and total calculation time span is significantly increased to provide linewidth and side peak studying result with higher accuracy. Generating each point on the mapping requires over 4 hours of calculation (calculated with MathLAB 2018a using 4<sup>th</sup> order Runge–Kutta method). Upon checking the P1 microwave under different injection conditions or other short-external cavity feedback delay time, the general behavior of the optical feedback affecting the P1 microwave remains same, due to the time constraint, detailed mapping of the feedback strength or phase variation affecting the P1 microwave quality is not provided and could be further generated in the future. The ratio of the feedback strength and injection strength affecting the VCSEL P1 oscillation state can be further studied.



- In Chapter 4, we have used optical feedbacks to reduce the microwave linewidth and improve its stability. However, during the experiment, the P1 frequency still drifts on the order of megahertz. This frequency drift is attributed to the environmental fluctuations such as bias current output purity, temperature variation, and optical table vibration. It can be improved by package the whole setup into a compact module to resist the environmental fluctuations.

## 7 Reference

- [1] G. P. Agrawal and N. K. Dutta, *Semiconductor Lasers*. Boston, MA: Springer US, 1995.
- [2] I. Hayashi, M. B. Panish, P. W. Foy, and S. Sumski, "JUNCTION LASERS WHICH OPERATE CONTINUOUSLY AT ROOM TEMPERATURE," *Appl. Phys. Lett.*, vol. 17, no. 3, pp. 109–111, Aug. 1970.
- [3] J. Ohtsubo, *Semiconductor Lasers*, vol. 111. Berlin, Heidelberg: Springer Berlin Heidelberg, 2013.
- [4] J. P. Toomey, D. M. Kane, A. Davidovic, and E. H. Huntington, "Hybrid electronic/optical synchronized chaos communication system," *Opt. Express*, vol. 17, no. 9, p. 7556, Apr. 2009.
- [5] K. E. Chlouverakis and M. J. Adams, "Optoelectronic realization of NOR logic gate using chaotic two-section lasers," *Electron. Lett.*, vol. 41, no. 6, pp. 359–360, 2005.
- [6] A. Wang, N. Wang, Y. Yang, B. Wang, M. Zhang, and Y. Wang, "Precise fault location in WDM-PON by utilizing wavelength tunable chaotic laser," *J. Light. Technol.*, vol. 30, no. 21, pp. 3420–3426, 2012.
- [7] L. Xia, D. Huang, J. Xu, and D. Liu, "Simultaneous and precise fault locating in WDM-PON by the generation of optical wideband chaos," *Opt. Lett.*, vol. 38, no. 19, p. 3762, Oct. 2013.
- [8] Z. N. Wang, M. Q. Fan, L. Zhang, H. Wu, D. V. Churkin, Y. Li, X. Y. Qian, and Y. J. Rao, "Long-range and high-precision correlation optical time-domain reflectometry utilizing an all-fiber chaotic source," *Opt. Express*, vol. 23, no. 12, p. 15514, Jun. 2015.
- [9] F.-Y. Lin and J.-M. Liu, "Chaotic lidar," *IEEE J. Sel. Top. quantum Electron.*, vol. 10, no. 5, pp. 991–997, 2004.

- [10] UchidaAtsushi, AmanoKazuya, InoueMasaki, HiranoKunihito, NaitoSunao, SomeyaHiroyuki, OowadaIsao, KurashigeTakayuki, ShikiMasaru, YoshimoriShigeru, YoshimuraKazuyuki, and DavisPeter, “Fast physical random bit generation with chaotic semiconductor lasers,” *Nat Phot.*, vol. 2, no. 12, pp. 728–732, Dec. 2008.
- [11] I. Kanter, Y. Aviad, I. Reidler, E. Cohen, and M. Rosenbluh, “An optical ultrafast random bit generator,” *Nat Phot.*, vol. 4, no. 1, pp. 58–61, Jan. 2010.
- [12] S. Wieczorek, B. Krauskopf, T. B. Simpson, and D. Lenstra, “The dynamical complexity of optically injected semiconductor lasers,” *Phys. Rep.*, vol. 416, no. 1–2, pp. 1–128, Sep. 2005.
- [13] J. Sacher, D. Baums, P. Panknin, W. Elsässer, and E. O. Göbel, “Intensity instabilities of semiconductor lasers under current modulation, external light injection, and delayed feedback,” *Phys. Rev. A*, vol. 45, no. 3, pp. 1893–1905, Feb. 1992.
- [14] E. K. Lau, Liang Jie Wong, and M. C. Wu, “Enhanced Modulation Characteristics of Optical Injection-Locked Lasers: A Tutorial,” *IEEE J. Sel. Top. Quantum Electron.*, vol. 15, no. 3, pp. 618–633, 2009.
- [15] J. P. Toomey, D. M. Kane, M. W. Lee, and K. A. Shore, “Nonlinear dynamics of semiconductor lasers with feedback and modulation,” *Opt. Express*, vol. 18, no. 16, p. 16955, Aug. 2010.
- [16] V. Annovazzi-Lodi, A. Scire, M. Sorel, and S. Donati, “Dynamic behavior and locking of a semiconductor laser subjected to external injection,” *IEEE J. Quantum Electron.*, vol. 34, no. 12, pp. 2350–2357, 1998.
- [17] T. . Simpson, “Mapping the nonlinear dynamics of a distributed feedback semiconductor laser subject to external optical injection,” *Opt. Commun.*, vol. 215, no. 1–3, pp. 135–151, Jan. 2003.
- [18] T. Perez, M. Radziunas, H.-J. Wunsche, C. R. Mirasso, and F. Henneberger, “Synchronization properties of two coupled multisection semiconductor lasers emitting chaotic light,” *IEEE Photonics Technol. Lett.*, vol. 18, no. 20, pp. 2135–

2137, Oct. 2006.

- [19] K. Schires, A. Hurtado, I. D. Henning, and M. J. Adams, "Polarization and Time-Resolved Dynamics of a 1550-nm VCSEL Subject to Orthogonally Polarized Optical Injection," *IEEE Photonics J.*, vol. 3, no. 3, pp. 555–563, Jun. 2011.
- [20] K. Schires, A. Hurtado, I. D. Henning, and M. J. Adams, "Comprehensive experimental analysis of nonlinear dynamics in an optically-injected semiconductor laser," *AIP Adv.*, vol. 1, no. 3, p. 032131, Sep. 2011.
- [21] J. BuesaAltes, I. Gatare, K. Panajotov, H. Thienpont, M. Sciamanna, J. B. Altés, I. Gatare, K. Panajotov, H. Thienpont, and M. Sciamanna, "Mapping of the dynamics induced by orthogonal optical injection in vertical-cavity surface-emitting lasers," *IEEE J. Quantum Electron.*, vol. 42, no. 2, pp. 198–207, Feb. 2006.
- [22] A. Hurtado, A. Quirce, A. Valle, L. Pesquera, and M. J. Adams, "Nonlinear dynamics induced by parallel and orthogonal optical injection in 1550 nm Vertical-Cavity Surface-Emitting Lasers (VCSELs)," *Opt. Express*, vol. 18, no. 9, p. 9423, Apr. 2010.
- [23] I. Gatare, M. Sciamanna, M. Nizette, H. Thienpont, and K. Panajotov, "Mapping of two-polarization-mode dynamics in vertical-cavity surface-emitting lasers with optical injection," *Phys. Rev. E*, vol. 80, no. 2, p. 026218, Aug. 2009.
- [24] A. Hurtado, D. Labukhin, I. D. Henning, and M. J. Adams, "Injection Locking Bandwidth in 1550-nm VCSELs Subject to Parallel and Orthogonal Optical Injection," *IEEE J. Sel. Top. Quantum Electron.*, vol. 15, no. 3, pp. 585–593, 2009.
- [25] L. Chrostowski, B. Faraji, W. Hofmann, M.-C. Amann, S. Wiczorek, and W. W. Chow, "40 GHz Bandwidth and 64 GHz Resonance Frequency in Injection-Locked 1.55  $\mu\text{m}$  VCSELs," *IEEE J. Sel. Top. Quantum Electron.*, vol. 13, no. 5, pp. 1200–1208, 2007.
- [26] A. Hurtado, I. D. Henning, and M. J. Adams, "Two-Wavelength Switching With a 1550 nm VCSEL Under Single Orthogonal Optical Injection," *IEEE J. Sel.*

*Top. Quantum Electron.*, vol. 14, no. 3, pp. 911–917, 2008.

- [27] K. H. Kim, S. H. Lee, and V. M. Deshmukh, “Dynamics of 1.55  $\mu\text{m}$  Wavelength Single-Mode Vertical-Cavity Surface-Emitting Laser Output under External Optical Injection,” *Adv. Opt. Technol.*, vol. 2012, pp. 1–10, Nov. 2012.
- [28] I. Gatare, J. Buesa, H. Thienpont, K. Panajotov, and M. Sciamanna, “Polarization Switching Bistability and Dynamics in Vertical-Cavity Surface-Emitting Laser under Orthogonal Optical Injection,” *Opt. Quantum Electron.*, vol. 38, no. 4–6, pp. 429–443, Mar. 2006.
- [29] Z. G. Pan, S. Jiang, M. Dagenais, R. A. Morgan, K. Kojima, M. T. Asom, R. E. Leibenguth, G. D. Guth, and M. W. Focht, “Optical injection induced polarization bistability in vertical-cavity surface-emitting lasers,” *Appl. Phys. Lett.*, vol. 63, no. 22, pp. 2999–3001, Nov. 1993.
- [30] J. Wang, M. K. Haldar, L. Li, and F. V. C. Mendis, “Enhancement of modulation bandwidth of laser diodes by injection locking,” *IEEE Photonics Technol. Lett.*, vol. 8, no. 1, pp. 34–36, Jan. 1996.
- [31] I. Petitbon, P. Gallion, G. Debarge, and C. Chabran, “Locking Bandwidth and Relaxation Oscillations of an Injection-Locked Semiconductor Laser,” *IEEE J. Quantum Electron.*, vol. 24, no. 2, pp. 148–154, Feb. 1988.
- [32] R. P. Braun, G. Grosskopf, D. Rohde, and F. Schmidt, “Low-phase-noise millimeter-wave generation at 64 GHz and data transmission using optical sideband injection locking,” *IEEE Photonics Technol. Lett.*, vol. 10, no. 5, pp. 728–730, May 1998.
- [33] F. Mogensen, H. Olesen, and G. Jacobsen, “Locking conditions and stability properties for a semiconductor laser with external light injection,” *IEEE J. Quantum Electron.*, vol. 21, no. 7, pp. 784–793, Jul. 1985.
- [34] R. Lang, “Injection Locking Properties of a Semiconductor Laser,” *IEEE J. Quantum Electron.*, vol. 18, no. 6, pp. 976–983, Jun. 1982.
- [35] D. Rontani, A. Locquet, M. Sciamanna, and D. S. Citrin, “Loss of time-delay

- signature in the chaotic output of a semiconductor laser with optical feedback,” *Opt. Lett.*, vol. 32, no. 20, pp. 2960–2, Oct. 2007.
- [36] D. Rontani, A. Locquet, M. Sciamanna, and D. S. Citrin, “Population pulsations and nondegenerate four-wave mixing in semiconductor lasers and amplifiers,” *Opt. Lett.*, vol. 32, no. 20, pp. 2960–2, Oct. 2007.
- [37] D. Rontani, A. Locquet, M. Sciamanna, and D. S. Citrin, “Degenerate four-wave mixing in semiconductor-doped glasses,” *Opt. Lett.*, vol. 32, no. 20, pp. 2960–2, Oct. 2007.
- [38] A. Yariv and D. M. Pepper, “Amplified reflection, phase conjugation, and oscillation in degenerate four-wave mixing,” *Opt. Lett.*, vol. 1, no. 1, p. 16, Jul. 1977.
- [39] G. P. Agrawal, “Effect of gain nonlinearities on period doubling and chaos in directly modulated semiconductor lasers,” *Appl. Phys. Lett.*, vol. 49, no. 16, pp. 1013–1015, Oct. 1986.
- [40] C. H. Lee, T. H. Yoon, and S. Y. Shin, “Period doubling and chaos in a directly modulated laser diode,” *Appl. Phys. Lett.*, vol. 46, no. 1, pp. 95–97, Jan. 1985.
- [41] T. B. Simpson, J. M. Liu, A. Gavrielides, V. Kovanis, and P. M. Alsing, “Period-doubling route to chaos in a semiconductor laser subject to optical injection,” *Appl. Phys. Lett.*, vol. 64, no. 26, pp. 3539–3541, Jun. 1994.
- [42] T. B. Simpson, J. M. Liu, A. Gavrielides, V. Kovanis, and P. M. Alsing, “Period-doubling cascades and chaos in a semiconductor laser with optical injection,” *Phys. Rev. A*, vol. 51, no. 5, pp. 4181–4185, May 1995.
- [43] J.-G. Wu, Z.-M. Wu, G.-Q. Xia, and G.-Y. Feng, “Evolution of time delay signature of chaos generated in a mutually delay-coupled semiconductor lasers system,” *Opt. Express*, vol. 20, no. 2, p. 1741, Jan. 2012.
- [44] D. Rontani, E. Mercier, D. Wolfersberger, and M. Sciamanna, “Enhanced complexity of optical chaos in a laser diode with phase-conjugate feedback,” *Opt. Lett.*, vol. 41, no. 20, p. 4637, Oct. 2016.

- [45] J. Mørk, J. Mark, and B. Tromborg, “Route to chaos and competition between relaxation oscillations for a semiconductor laser with optical feedback,” *Phys. Rev. Lett.*, vol. 65, no. 16, pp. 1999–2002, Oct. 1990.
- [46] T. Mukai and K. Otsuka, “New route to optical chaos: Successive-subharmonic-oscillation cascade in a semiconductor laser coupled to an external cavity,” *Phys. Rev. Lett.*, vol. 55, no. 17, pp. 1711–1714, Oct. 1985.
- [47] A. Argyris, D. Syvridis, L. Larger, V. Annovazzi-Lodi, P. Colet, I. Fischer, J. García-Ojalvo, C. R. Mirasso, L. Pesquera, and K. A. Shore, “Chaos-based communications at high bit rates using commercial fibre-optic links,” *Nature*, vol. 438, no. 7066, pp. 343–346, 2005.
- [48] S. Y. Xiang, W. Pan, A. J. Wen, N. Q. Li, L. Y. Zhang, L. Shang, and H. X. Zhang, “Conceal Time Delay Signature of Chaos in Semiconductor Lasers With Dual-Path Injection,” *IEEE Photonics Technol. Lett.*, vol. 25, no. 14, pp. 1398–1401, Jul. 2013.
- [49] Y. Takiguchi, K. Ohyagi, and J. Ohtsubo, “Bandwidth-enhanced chaos synchronization in strongly injection-locked semiconductor lasers with optical feedback,” *Opt. Lett.*, vol. 28, no. 5, pp. 319–321, 2003.
- [50] D. M. Kane, J. P. Toomey, M. W. Lee, and K. A. Shore, “Correlation dimension signature of wideband chaos synchronization of semiconductor lasers,” *Opt. Lett.*, vol. 31, no. 1, p. 20, Jan. 2006.
- [51] Y. Hong, M. W. Lee, J. Paul, P. S. Spencer, and K. A. Shore, “Enhanced chaos synchronization in unidirectionally coupled vertical-cavity surface-emitting semiconductor lasers with polarization-preserved injection,” *Opt. Lett.*, vol. 33, no. 6, pp. 587–589, 2008.
- [52] G. C. Dente, P. S. Durkin, K. A. Wilson, and C. E. Moeller, “Chaos in the coherence collapse of semiconductor lasers,” *IEEE J. Quantum Electron.*, vol. 24, pp. 2441–2447, 1988.
- [53] S. Donati and S.-K. Hwang, “Chaos and high-level dynamics in coupled lasers and their applications,” *Prog. Quantum Electron.*, vol. 36, no. 2–3, pp. 293–341,

Mar. 2012.

- [54] Y. Hong, P. S. Spencer, and K. A. Shore, “Wideband chaos with time-delay concealment in vertical-cavity surface-emitting lasers with optical feedback and injection,” *IEEE J. Quantum Electron.*, vol. 50, no. 4, pp. 236–242, 2014.
- [55] K. E. Callan, L. Illing, Z. Gao, D. J. Gauthier, and E. Scho, “Broadband Chaos Generated by an Optoelectronic Oscillator,” *Phys. Rev. Lett.*, vol. 104, no. March, p. 113901, 2010.
- [56] A. Quirce, A. Valle, H. Thienpont, and K. Panajotov, “Enhancement of chaos bandwidth in VCSELs induced by simultaneous orthogonal optical injection and optical feedback,” *IEEE J. Quantum Electron.*, vol. 52, no. 99, p. 2400609, 2016.
- [57] Y. Hong, P. S. Spencer, S. Bandyopadhyay, P. Rees, and K. A. Shore, “Polarisation-resolved chaos and instabilities in a vertical cavity surface emitting laser subject to optical injection,” *Opt. Commun.*, vol. 216, no. 1–3, pp. 185–189, 2003.
- [58] J.-P. Zhuang and S.-C. Chan, “Phase noise characteristics of microwave signals generated by semiconductor laser dynamics,” *Opt. Express*, vol. 23, no. 3, p. 2777, 2015.
- [59] Z. Zhu, D. Mühlbacher, M. Morana, M. Koppe, M. C. Scharber, D. Waller, G. Dennler, C. J. Brabec, V. Petrova-Koch, R. Hezel, and A. Goetzberger, *VCSELs*, vol. 166. Berlin, Heidelberg: Springer Berlin Heidelberg, 2013.
- [60] Z. G. Pan, S. Jiang, M. Dagenais, R. A. Morgan, K. Kojima, M. T. Asom, R. E. Leibenguth, G. D. Guth, and M. W. Focht, “Optical injection induced polarization bistability in vertical-cavity surface-emitting lasers,” *Appl. Phys. Lett.*, vol. 63, no. 22, pp. 2999–3001, Nov. 1993.
- [61] M. Tang, H. Minamide, Y. Wang, T. Notake, S. Ohno, and H. Ito, “Tunable terahertz-wave generation from DAST crystal pumped by a monolithic dual-wavelength fiber laser,” *Opt. Express*, vol. 19, no. 2, p. 779, Jan. 2011.
- [62] A. Quirce, A. Valle, and L. Pesquera, “Very Wide Hysteresis Cycles in 1550-nm



VCSELs Subject to Orthogonal Optical Injection,” *IEEE Photonics Technol. Lett.*, vol. 21, no. 17, pp. 1193–1195, Sep. 2009.

- [63] A. Valle, M. Gómez-Molina, and L. Pesquera, “Polarization bistability in 1550 nm wavelength single-mode vertical-cavity surface-emitting lasers subject to orthogonal optical injection,” *IEEE J. Sel. Top. Quantum Electron.*, vol. 14, no. 3, pp. 895–902, 2008.
- [64] A. Hurtado, I. D. Henning, and M. J. Adams, “Different forms of wavelength polarization switching and bistability in a 155  $\mu\text{m}$  vertical-cavity surface-emitting laser under orthogonally polarized optical injection,” *Opt. Lett.*, vol. 34, no. 3, p. 365, Feb. 2009.
- [65] A. Homayounfar and M. J. Adams, “Locking bandwidth and birefringence effects for polarized optical injection in vertical-cavity surface-emitting lasers,” *Opt. Commun.*, vol. 269, no. 1, pp. 119–127, Jan. 2007.
- [66] M. Sciamanna and K. Panajotov, “Route to polarization switching induced by optical injection in vertical-cavity surface-emitting lasers,” *Phys. Rev. A*, vol. 73, no. 2, p. 023811, Feb. 2006.
- [67] K. Panajotov, I. Gatare, A. Valle, H. Thienpont, and M. Sciamanna, “Polarization- and Transverse-Mode Dynamics in Optically Injected and Gain-Switched Vertical-Cavity Surface-Emitting Lasers,” *IEEE J. Quantum Electron.*, vol. 45, no. 11, pp. 1473–1481, Nov. 2009.
- [68] A. Hurtado, I. D. Henning, and M. J. Adams, “Differences in the injection locking bandwidth in 1550nm-VCSELs subject to parallel and orthogonal optical injection,” in *2008 IEEE 21st International Semiconductor Laser Conference*, 2008, pp. 87–88.
- [69] C. H. Chang, L. Chrostowski, and C. J. Chang-Hasnain, “Injection Locking of VCSELs,” in *IEEE Journal on Selected Topics in Quantum Electronics*, 2003, vol. 9, no. 5, pp. 1386–1393.
- [70] R. Tkach and A. Chraplyvy, “Regimes of feedback effects in 1.5- $\mu\text{m}$  distributed feedback lasers,” *J. Light. Technol.*, vol. 4, no. 11, pp. 1655–1661,

- 1986.
- [71] T. Erneux and P. Glorieux, *Laser dynamics*. Cambridge University Press, 2010.
  - [72] M. Sciamanna and K. A. Shore, “Physics and applications of laser diode chaos,” *Nat. Photonics*, vol. 9, no. 3, pp. 151–162, Mar. 2015.
  - [73] H. Haken, “Analogy between higher instabilities in fluids and lasers,” *Phys. Lett. A*, vol. 53, no. 1, pp. 77–78, May 1975.
  - [74] F. T. Arecchi, R. Meucci, G. Puccioni, and J. Tredicce, “Experimental evidence of subharmonic bifurcations, multistability, and turbulence in a Q-switched gas laser,” *Phys. Rev. Lett.*, vol. 49, no. 17, pp. 1217–1220, Oct. 1982.
  - [75] T. Midavaine, D. Dangoisse, and P. Glorieux, “Observation of Chaos in a Frequency-Modulated CO<sub>2</sub> Laser,” *Phys. Rev. Lett.*, vol. 55, no. 19, pp. 1989–1992, Nov. 1985.
  - [76] H. Haken, *Light*. Amsterdam ;;New York ;;Oxford: North-Holland Pub. Co., 1985.
  - [77] N. Li, L. Zunino, A. Locquet, B. Kim, D. Choi, W. Pan, and D. S. Citrin, “Multiscale Ordinal Symbolic Analysis of the Lang-Kobayashi Model for External-Cavity Semiconductor Lasers: A Test of Theory,” *IEEE J. Quantum Electron.*, vol. 51, no. 8, pp. 1–6, Aug. 2015.
  - [78] R. Lang and K. Kobayashi, “External Optical Feedback Effects on Semiconductor Injection Laser Properties,” *IEEE J. Quantum Electron.*, vol. 16, no. 3, pp. 347–355, Mar. 1980.
  - [79] M. Tachikawa, F.-L. Hong, K. Tanii, and T. Shimizu, “Deterministic Chaos in Passive  $Q$ -Switching Pulsation of a  $C_0O_2$  Laser with Saturab,” *Phys. Rev. Lett.*, vol. 60, no. 22, pp. 2266–2268, May 1988.
  - [80] F. Papoff, A. Fioretti, E. Arimondo, G. B. Mindlin, H. Solari, and R. Gilmore,

- “Structure of chaos in the laser with saturable absorber,” *Phys. Rev. Lett.*, vol. 68, no. 8, pp. 1128–1131, Feb. 1992.
- [81] S. Tang and J. M. Liu, “Chaotic pulsing and quasi-periodic route to chaos in a semiconductor laser with delayed opto-electronic feedback,” *IEEE J. Quantum Electron.*, vol. 37, no. 3, pp. 329–336, Mar. 2001.
- [82] J. G. Freire, R. Meucci, F. T. Arecchi, and J. A. C. Gallas, “Self-organization of pulsing and bursting in a CO<sub>2</sub> laser with opto-electronic feedback,” *Chaos An Interdiscip. J. Nonlinear Sci.*, vol. 25, no. 9, p. 097607, Sep. 2015.
- [83] A. Argyris, E. Grivas, M. Hamacher, A. Bogris, and D. Syvridis, “Chaos-on-a-chip secures data transmission in optical fiber links,” *Opt. Express*, vol. 18, no. 5, p. 5188, Mar. 2010.
- [84] C. Masoller, “Anticipation in the synchronization of chaotic semiconductor lasers with optical feedback,” *Phys. Rev. Lett.*, vol. 86, no. 13, pp. 2782–2785, 2001.
- [85] M. Sciamanna, I. Gatare, A. Locquet, and K. Panajotov, “Polarization synchronization in unidirectionally coupled vertical-cavity surface-emitting lasers with orthogonal optical injection,” *Phys. Rev. E*, vol. 75, no. 5, p. 56213, 2007.
- [86] Y. Hong, M. W. Lee, J. Paul, P. S. Spencer, and K. A. Shore, “GHz bandwidth message transmission using chaotic vertical-cavity surface-emitting lasers,” *J. Light. Technol.*, vol. 27, no. 22, 2009.
- [87] J.-G. Wu, Z.-M. Wu, G.-Q. Xia, T. Deng, X.-D. Lin, X. Tang, and G.-Y. Feng, “Isochronous Synchronization Between Chaotic Semiconductor Lasers Over 40-km Fiber Links,” *IEEE Photonics Technol. Lett.*, vol. 23, no. 24, pp. 1854–1856, Dec. 2011.
- [88] S. Y. Xiang, W. Pan, B. Luo, L. S. Yan, X. H. Zou, N. Jiang, N. Q. Li, and H. N. Zhu, “Message Encoding/Decoding Using Unpredictability-Enhanced Chaotic VCSELs,” *IEEE Photonics Technol. Lett.*, vol. 24, no. 15, pp. 1267–1269, Aug. 2012.

- [89] T. Erneux, A. Gavrielides, and M. Sciamanna, “Stable microwave oscillations due to external-cavity-mode beating in laser diodes subject to optical feedback,” *Phys. Rev. A*, vol. 66, no. 3, p. 033809, Sep. 2002.
- [90] A. Uchida, *Optical Communication with Chaotic Lasers*. Weinheim, Germany: Wiley-VCH Verlag GmbH & Co. KGaA, 2012.
- [91] D. Rontani, A. Locquet, M. Sciamanna, D. S. Citrin, and S. Ortin, “Time-delay identification in a chaotic semiconductor laser with optical feedback: A dynamical point of view,” *IEEE J. Quantum Electron.*, vol. 45, no. 7, pp. 879–891, Jul. 2009.
- [92] A. Wang, Y. Yang, B. Wang, B. Zhang, L. Li, and Y. Wang, “Generation of wideband chaos with suppressed time-delay signature by delayed self-interference,” *Opt. Express*, vol. 21, no. 7, p. 8701, Apr. 2013.
- [93] R. M. Nguimdo, P. Colet, L. Larger, and L. Pesquera, “Digital Key for Chaos Communication Performing Time Delay Concealment,” *Phys. Rev. Lett.*, vol. 107, no. 3, p. 34103, Jul. 2011.
- [94] C.-H. Cheng, Y.-C. Chen, and F.-Y. Lin, “Chaos time delay signature suppression and bandwidth enhancement by electrical heterodyning,” *Opt. Express*, vol. 23, no. 3, p. 2308, Feb. 2015.
- [95] Song-Sui Li and Sze-Chun Chan, “Chaotic Time-Delay Signature Suppression in a Semiconductor Laser With Frequency-Detuned Grating Feedback,” *IEEE J. Sel. Top. Quantum Electron.*, vol. 21, no. 6, pp. 541–552, Nov. 2015.
- [96] M. T. Rosenstein, J. J. Collins, and C. J. De Luca, “A practical method for calculating largest Lyapunov exponents from small data sets,” *Phys. D Nonlinear Phenom.*, vol. 65, no. 1–2, pp. 117–134, May 1993.
- [97] H. Kantz, “A robust method to estimate the maximal Lyapunov exponent of a time series,” *Phys. Lett. A*, vol. 185, no. 1, pp. 77–87, Jan. 1994.
- [98] P. Grassberger and I. Procaccia, “Measuring the strangeness of strange attractors,” *Phys. D Nonlinear Phenom.*, vol. 9, no. 1–2, pp. 189–208, Oct. 1983.

- [99] C. Bandt and B. Pompe, “Permutation Entropy: A Natural Complexity Measure for Time Series,” *Phys. Rev. Lett.*, vol. 88, no. 17, p. 174102, Apr. 2002.
- [100] J. P. Toomey and D. M. Kane, “Mapping the dynamic complexity of a semiconductor laser with optical feedback using permutation entropy,” *Opt. Express*, vol. 22, no. 2, p. 1713, Jan. 2014.
- [101] N. Li, W. Pan, A. Locquet, and D. S. Citrin, “Time-delay concealment and complexity enhancement of an external-cavity laser through optical injection,” *Opt. Lett.*, vol. 40, no. 19, pp. 4416–9, 2015.
- [102] S. Y. Xiang, W. Pan, B. Luo, L. S. Yan, X. H. Zou, N. Li, and H. N. Zhu, “Wideband Unpredictability-Enhanced Chaotic Semiconductor Lasers With Dual-Chaotic Optical Injections,” *IEEE J. Quantum Electron.*, vol. 48, no. 8, pp. 1069–1076, 2012.
- [103] R. Blumenthal, “Design of a Microwave-Frequency Light Modulator,” *Proc. IRE*, vol. 50, no. 4, pp. 452–456, Apr. 1962.
- [104] N. Dagli, “Wide-bandwidth lasers and modulators for RF photonics,” *IEEE Trans. Microw. Theory Tech.*, vol. 47, no. 7 PART 2, pp. 1151–1171, Jul. 1999.
- [105] S. C. Chan and J. M. Liu, “Tunable narrow-linewidth photonic microwave generation using semiconductor laser dynamics,” *IEEE J. Sel. Top. Quantum Electron.*, vol. 10, no. 5, pp. 1025–1032, 2004.
- [106] S.-C. Chan, S.-K. Hwang, and J.-M. Liu, “Period-one oscillation for photonic microwave transmission using an optically injected semiconductor laser,” *Opt. Express*, vol. 15, no. 22, pp. 14921–14935, 2007.
- [107] J. Capmany and D. Novak, “Microwave photonics combines two worlds,” *Nat. Photonics*, vol. 1, no. 6, pp. 319–330, Jun. 2007.
- [108] J. Yao, “Microwave photonics,” *Conf. Proc. - Int. Conf. Indium Phosphide Relat. Mater.*, vol. 27, no. 3, pp. 212–214, 2009.
- [109] Yu-Shan Juan and Fan-Yi Lin, “Photonic Generation of Broadly Tunable Microwave Signals Utilizing a Dual-Beam Optically Injected Semiconductor

- Laser,” *IEEE Photonics J.*, vol. 3, no. 4, pp. 644–650, Aug. 2011.
- [110] S. Wieczorek, W. W. Chow, L. Chrostowski, and C. J. Chang-Hasnain, “Improved Semiconductor-Laser Dynamics From Induced Population Pulsation,” *IEEE J. Quantum Electron.*, vol. 42, no. 6, pp. 552–562, Jun. 2006.
- [111] F. Grillot, Cheng Wang, N. A. Naderi, and J. Even, “Modulation Properties of Self-Injected Quantum-Dot Semiconductor Diode Lasers,” *IEEE J. Sel. Top. Quantum Electron.*, vol. 19, no. 4, pp. 1900812–1900812, Jul. 2013.
- [112] L. F. Lester, N. A. Naderi, F. Grillot, R. Raghunathan, and V. Kovanis, “Strong optical injection and the differential gain in a quantum dash laser,” *Opt. Express*, vol. 22, no. 6, p. 7222, Mar. 2014.
- [113] S. K. Hwang, J. M. Liu, and J. K. White, “35-GHz Intrinsic Bandwidth for Direct Modulation in 1.3- $\mu$ m Semiconductor Lasers Subject to Strong Injection Locking,” *IEEE Photonics Technol. Lett.*, vol. 16, no. 4, pp. 972–974, Apr. 2004.
- [114] H. Miyazawa, K. Noguchi, and O. Mitomi, “Millimeter-Wave Ti:LiNbO<sub>3</sub> Optical Modulators,” *J. Light. Technol. Vol. 16, Issue 4, pp. 615-*, vol. 16, no. 4, p. 615, Apr. 1998.
- [115] B. Bortnik, Y.-C. C. Hung, H. Tazawa, B.-J. J. Seo, J. Luo, A. K.-Y. Y. Jen, W. H. Steier, and H. R. Fetterman, “Electrooptic polymer ring resonator modulation up to 165 GHz,” *IEEE J. Sel. Top. Quantum Electron.*, vol. 13, no. 1, pp. 104–109, 2007.
- [116] Y. Enami, C. T. Deroose, D. Mathine, C. Loychik, C. Greenlee, R. A. Norwood, T. D. Kim, J. Luo, Y. Tian, A. K.-Y. Jen, and N. Peyghambarian, “Hybrid polymer/sol-gel waveguide modulators with exceptionally large electro-optic coefficients,” *Nat. Photonics*, vol. 1, no. 3, pp. 180–185, Mar. 2007.
- [117] T. Ido, S. Tanaka, M. Suzuki, M. Koizumi, H. Sano, and H. Inoue, “Ultra-high-speed multiple-quantum-well electro-absorption optical modulators with integrated waveguides,” *J. Light. Technol.*, vol. 14, no. 9, pp. 2026–2034, 1996.
- [118] R. J. Steed, L. Ponnampalam, M. J. Fice, C. C. Renaud, D. C. Rogers, D. G.

- Moodie, G. D. Maxwell, I. F. Lealman, M. J. Robertson, L. Pavlovic, L. Naglic, M. Vidmar, and A. J. Seeds, "Hybrid Integrated Optical Phase-Lock Loops for Photonic Terahertz Sources," *IEEE J. Sel. Top. Quantum Electron.*, vol. 17, no. 1, pp. 210–217, Jan. 2011.
- [119] A. C. Bordonalli, C. Walton, and A. J. Seeds, "High-performance phase locking of wide linewidth semiconductor lasers by combined use of optical injection locking and optical phase-lock loop," *J. Light. Technol.*, vol. 17, no. 2, pp. 328–342, 1999.
- [120] Y.-H. Hung and S.-K. Hwang, "Photonic microwave stabilization for period-one nonlinear dynamics of semiconductor lasers using optical modulation sideband injection locking," *Opt. Express*, vol. 23, no. 5, p. 6520, Mar. 2015.
- [121] K. Balakier, M. J. Fice, L. Ponnampalam, A. J. Seeds, and C. C. Renaud, "Monolithically Integrated Optical Phase Lock Loop for Microwave Photonics," *J. Light. Technol.*, vol. 32, no. 20, pp. 3893–3900, Oct. 2014.
- [122] X. Wang and G. Li, "Subcarrier frequency enhancement of two-section Fabry–Perot laser diodes using external optical injection," *Opt. Commun.*, vol. 171, no. 1–3, pp. 113–118, Nov. 1999.
- [123] J. B. Georges and K. Y. Lau, "Self-pulsating laser diodes as fast-tunable ( $\leq 1$  ns) FSK transmitters in subcarrier multiple-access networks," *IEEE Photonics Technol. Lett.*, vol. 5, no. 2, pp. 242–245, Feb. 1993.
- [124] X. Wang, G. Li, and C. S. Ih, "Microwave/millimeter-wave frequency subcarrier lightwave modulations based on self-sustained pulsation of laser diode," *J. Light. Technol.*, vol. 11, no. 2, pp. 309–315, 1993.
- [125] F. Li and A. S. Helmy, "Gigahertz to terahertz tunable all-optical single-sideband microwave generation via semiconductor optical amplifier gain engineering," *Opt. Lett.*, vol. 38, no. 22, p. 4542, Nov. 2013.
- [126] Y.-N. Tan, L. Jin, L. Cheng, Z. Quan, M. Li, and B.-O. Guan, "Multi-octave tunable RF signal generation based on a dual-polarization fiber grating laser," *Opt. Express*, vol. 20, no. 7, p. 6961, Mar. 2012.

- [127] X. S. Yao and L. Maleki, "Multiloop optoelectronic oscillator," *IEEE J. Quantum Electron.*, vol. 36, no. 1, pp. 79–84, Jan. 2000.
- [128] X. S. Yao and L. Maleki, "Optoelectronic microwave oscillator," *J. Opt. Soc. Am. B*, vol. 13, no. 8, p. 1725, Aug. 1996.
- [129] S. Pan and J. Yao, "Wideband and frequency-tunable microwave generation using an optoelectronic oscillator incorporating a Fabry–Perot laser diode with external optical injection," *Opt. Lett.*, vol. 35, no. 11, p. 1911, Jun. 2010.
- [130] J.-Y. Kim, J.-H. Jo, W.-Y. Choi, and H.-K. Sung, "Dual-Loop Dual-Modulation Optoelectronic Oscillators With Highly Suppressed Spurious Tones," *IEEE Photonics Technol. Lett.*, vol. 24, no. 8, pp. 706–708, Apr. 2012.
- [131] B. Romeira, J. Javaloyes, J. M. L. Figueiredo, C. N. Ironside, H. I. Cantu, and A. E. Kelly, "Delayed Feedback Dynamics of Liénard-Type Resonant Tunneling-Photo-Detector Optoelectronic Oscillators," *IEEE J. Quantum Electron.*, vol. 49, no. 1, pp. 31–42, Jan. 2013.
- [132] B. Romeira, K. Seunarine, C. N. Ironside, A. E. Kelly, and J. M. L. Figueiredo, "A Self-Synchronized Optoelectronic Oscillator Based on an RTD Photodetector and a Laser Diode," *IEEE Photonics Technol. Lett.*, vol. 23, no. 16, pp. 1148–1150, Aug. 2011.
- [133] M. G. Thompson, A. R. Rae, Mo Xia, R. V. Penty, and I. H. White, "InGaAs Quantum-Dot Mode-Locked Laser Diodes," *IEEE J. Sel. Top. Quantum Electron.*, vol. 15, no. 3, pp. 661–672, 2009.
- [134] R. Rosales, K. Merghem, A. Martinez, A. Akrouit, J.-P. Tournenc, A. Accard, F. Lelarge, and A. Ramdane, "InAs/InP Quantum-Dot Passively Mode-Locked Lasers for 1.55- $\mu$ m Applications," *IEEE J. Sel. Top. Quantum Electron.*, vol. 17, no. 5, pp. 1292–1301, Sep. 2011.
- [135] C.-Y. Lin, F. Grillot, Y. Li, R. Raghunathan, and L. F. Lester, "Characterization of timing jitter in a 5 GHz quantum dot passively mode-locked laser," *Opt. Express*, vol. 18, no. 21, p. 21932, Oct. 2010.



- [136] X.-Q. Qi and J.-M. Liu, “Photonic Microwave Applications of the Dynamics of Semiconductor Lasers,” *IEEE J. Sel. Top. Quantum Electron.*, vol. 17, no. 5, pp. 1198–1211, 2011.
- [137] M. C. Pochet, N. A. Naderi, V. Kovanis, and L. F. Lester, “Modeling the Dynamic Response of an Optically-Injected Nanostructure Diode Laser,” *IEEE J. Quantum Electron.*, vol. 47, no. 6, pp. 827–833, Jun. 2011.
- [138] M. Pochet, T. Locke, and N. G. Usechak, “Generation and Modulation of a Millimeter-Wave Subcarrier on an Optical Frequency Generated via Optical Injection,” *IEEE Photonics J.*, vol. 4, no. 5, pp. 1881–1891, Oct. 2012.
- [139] S.-C. Chan, “Analysis of an Optically Injected Semiconductor Laser for Microwave Generation,” *IEEE J. Quantum Electron.*, vol. 46, no. 3, pp. 421–428, Mar. 2010.
- [140] Y.-H. Hung, C.-H. Chu, and S.-K. Hwang, “Optical double-sideband modulation to single-sideband modulation conversion using period-one nonlinear dynamics of semiconductor lasers for radio-over-fiber links,” *Opt. Lett.*, vol. 38, no. 9, p. 1482, May 2013.
- [141] P. Perez, A. Quirce, A. Valle, A. Consoli, I. Noriega, L. Pesquera, and I. Esquivias, “Photonic generation of microwave signals using a single-mode VCSEL subject to dual-beam orthogonal optical injection,” *IEEE Photonics J.*, vol. 7, no. 1, p. 5500614, Feb. 2015.
- [142] T. B. Simpson, Jia-Ming Liu, M. AlMulla, N. G. Usechak, V. Kovanis, J. M. Liu, M. AlMulla, N. G. Usechak, and V. Kovanis, “Linewidth sharpening via polarization-rotated feedback in optically injected semiconductor laser oscillators,” *IEEE J. Sel. Top. Quantum Electron.*, vol. 19, no. 4, pp. 1500807–1500807, Jul. 2013.
- [143] H. Lin, D. W. Pierce, A. J. Basnet, A. Quirce, Y. Zhang, and A. Valle, “Two-frequency injection on a multimode vertical-cavity surface-emitting laser,” *Opt. Express*, vol. 19, no. 23, p. 22437, Nov. 2011.
- [144] T. B. Simpson, J.-M. M. Liu, M. AlMulla, N. G. Usechak, and V. Kovanis,

- “Limit-cycle dynamics with reduced sensitivity to perturbations,” *Phys. Rev. Lett.*, vol. 112, no. 2, p. 023901, Jan. 2014.
- [145] A. Hurtado, I. D. Henning, M. J. Adams, and L. F. Lester, “Generation of tunable millimeter-wave and THz signals with an optically injected quantum dot distributed feedback laser,” *IEEE Photonics J.*, vol. 5, no. 4, pp. 5900107–5900107, Aug. 2013.
- [146] A. Quirce and A. Valle, “High-frequency microwave signal generation using multi-transverse mode VCSELs subject to two-frequency optical injection,” *Opt. Express*, vol. 20, no. 12, pp. 13390–401, Jun. 2012.
- [147] Y.-H. Hung and S.-K. Hwang, “Photonic microwave amplification for radio-over-fiber links using period-one nonlinear dynamics of semiconductor lasers,” *Opt. Lett.*, vol. 38, no. 17, p. 3355, Sep. 2013.
- [148] Y.-H. Liao and F.-Y. Lin, “Dynamical characteristics and their applications of semiconductor lasers subject to both optical injection and optical feedback,” *Opt. Express*, vol. 21, no. 20, p. 23568, Oct. 2013.
- [149] S.-C. Chan, S.-K. Hwang, and J.-M. Liu, “Radio-over-fiber AM-to-FM upconversion using an optically injected semiconductor laser,” *Opt. Lett.*, vol. 31, no. 15, pp. 2254–2256, Aug. 2006.
- [150] C. Wang, R. Raghunathan, K. Schires, S.-C. Chan, L. F. Lester, and F. Grillot, “Optically injected InAs/GaAs quantum dot laser for tunable photonic microwave generation,” *Opt. Lett.*, vol. 41, no. 6, pp. 1153–1156, 2016.
- [151] C. Cui and S.-C. Chan, “Performance Analysis on Using Period-One Oscillation of Optically Injected Semiconductor Lasers for Radio-Over-Fiber Uplinks,” *IEEE J. Quantum Electron.*, vol. 48, no. 4, pp. 490–499, Apr. 2012.
- [152] C. Cui, X. Fu, and S.-C. Chan, “Double-locked semiconductor laser for radio-over-fiber uplink transmission,” *Opt. Lett.*, vol. 34, no. 24, pp. 3821–3823, Dec. 2009.
- [153] M. Zhang, T. Liu, A. Wang, J. Zhang, and Y. Wang, “All-optical clock frequency

divider using Fabry–Perot laser diode based on the dynamical period-one oscillation,” *Opt. Commun.*, vol. 284, no. 5, pp. 1289–1294, Mar. 2011.

- [154] Sze-Chun Chan and Jia-Ming Liu, “Microwave frequency division and multiplication using an optically injected semiconductor laser,” *IEEE J. Quantum Electron.*, vol. 41, no. 9, pp. 1142–1147, Sep. 2005.
- [155] C.-H. Cheng, C.-W. Lee, T.-W. Lin, and F.-Y. Lin, “Dual-frequency laser Doppler velocimeter for speckle noise reduction and coherence enhancement,” *Opt. Express*, vol. 20, no. 18, p. 20255, Aug. 2012.
- [156] T. B. Simpson and F. Doft, “Double-locked laser diode for microwave photonics applications,” *IEEE Photonics Technol. Lett.*, vol. 11, no. 11, pp. 1476–1478, Nov. 1999.
- [157] J.-P. Zhuang and S.-C. Chan, “Tunable photonic microwave generation using optically injected semiconductor laser dynamics with optical feedback stabilization,” *Opt. Lett.*, vol. 38, no. 3, p. 344, Feb. 2013.
- [158] A. Valle, A. Quirce, S. Ji, and Y. Hong, “Polarization effects on Photonic Microwave Generation in VCSELs under Optical Injection,” *IEEE Photonics Technol. Lett.*, vol. 1135, no. x, pp. 1–1, 2018.
- [159] L. Liu, *Photonic Devices*. Cambridge, 2009.
- [160] D. T. Cassidy, “Spontaneous-emission factor of semiconductor diode lasers,” *J. Opt. Soc. Am. B*, vol. 8, no. 4, p. 747, Apr. 1991.
- [161] J. M. Liu, H. F. Chen, X. J. Meng, and T. B. Simpson, “Modulation bandwidth, noise, and stability of a semiconductor laser subject to strong injection locking,” *IEEE Photonics Technol. Lett.*, vol. 9, no. 10, pp. 1325–1327, Oct. 1997.
- [162] J.-G. Wu, G.-Q. Xia, X. Tang, X.-D. Lin, T. Deng, L. Fan, and Z.-M. Wu, “Time delay signature concealment of optical feedback induced chaos in an external cavity semiconductor laser,” *Opt. Express*, vol. 18, no. 7, pp. 6661–6, 2010.
- [163] L.-C. Lin, S.-H. Liu, and F.-Y. Lin, “Stability of period-one (P1) oscillations generated by semiconductor lasers subject to optical injection or optical

- feedback,” *Opt. Express*, vol. 25, no. 21, p. 25523, Oct. 2017.
- [164] K.-H. Lo, S.-K. Hwang, and S. Donati, “Numerical study of ultrashort-optical-feedback-enhanced photonic microwave generation using optically injected semiconductor lasers at period-one nonlinear dynamics,” *Opt. Express*, vol. 25, no. 25, p. 31595, Dec. 2017.
- [165] R. Al-Seyab, K. Schires, N. Ali Khan, A. Hurtado, I. D. Henning, and M. J. Adams, “Dynamics of polarized optical injection in 1550-nm VCSELs: Theory and experiments,” *IEEE J. Sel. Top. Quantum Electron.*, vol. 17, no. 5, pp. 1242–1249, 2011.
- [166] A. Quirce, A. Valle, H. Lin, D. W. Pierce, and Y. Zhang, “Photonic generation of high-frequency microwave signals utilizing a multi-transverse-mode vertical-cavity surface-emitting laser subject to two-frequency orthogonal optical injection,” vol. 29, no. 12, pp. 3259–3270, 2012.
- [167] Songkun Ji, Yanhua Hong, and P. S. Spencer, “Optically injection vertical-cavity surface-emitting lasers for tunable photonic microwave generation,” in *2017 19th International Conference on Transparent Optical Networks (ICTON)*, 2017, pp. 1–3.
- [168] S. Ji, Y. Hong, P. S. Spencer, J. Benedikt, and I. Davies, “Broad tunable photonic microwave generation based on period-one dynamics of optical injection vertical-cavity surface-emitting lasers,” *Opt. Express*, vol. 25, no. 17, p. 19863, Aug. 2017.
- [169] S. Ji, C. Xue, A. Valle, P. S. Spencer, H. Li, and Y. Hong, “Stabilization of Photonic Microwave Generation in Vertical-Cavity Surface-Emitting Lasers With Optical Injection and Feedback,” *J. Light. Technol.*, vol. 36, no. 19, pp. 4347–4353, Oct. 2018.
- [170] K.-H. Lo, S.-K. Hwang, and S. Donati, “Optical feedback stabilization of photonic microwave generation using period-one nonlinear dynamics of semiconductor lasers,” *Opt. Express*, vol. 22, no. 15, p. 18648, Jul. 2014.
- [171] W. Z.-M. Guang-Qiong, Sun Bo, Wu Jia-Gui, Wang Shun-Tian, “Theoretical

and experimental investigation on the narrow-linewidth photonic microwave generation based on parallel polarized optically injected 1550 nm vertical-cavity surface-emitting laser,” *Acta Phys. Sin.*, vol. 65, no. 1, p. 014207, 2016.

- [172] A. Murakami, K. Kawashima, and K. Atsuki, “Cavity resonance shift and bandwidth enhancement in semiconductor lasers with strong light injection,” *IEEE J. Quantum Electron.*, vol. 39, no. 10, pp. 1196–1204, Oct. 2003.
- [173] H. Liu, B. Ren, Q. Zhao, and N. Li, “Characterizing the optical chaos in a special type of small networks of semiconductor lasers using permutation entropy,” *Opt. Commun.*, vol. 359, pp. 79–84, Jan. 2016.
- [174] C. Quintero-Quiroz, S. Pigolotti, M. C. Torrent, and C. Masoller, “Numerical and experimental study of the effects of noise on the permutation entropy,” *New J. Phys.*, vol. 17, no. 9, p. 93002, Sep. 2015.
- [175] M. C. Soriano, L. Zunino, O. A. Rosso, I. Fischer, and C. R. Mirasso, “Time scales of a chaotic semiconductor laser with optical feedback under the lens of a permutation information analysis,” *IEEE J. Quantum Electron.*, vol. 47, no. 2, pp. 252–261, Feb. 2011.
- [176] N. Oliver, M. C. Soriano, D. W. Sukow, and I. Fischer, “Dynamics of a semiconductor laser with polarization-rotated feedback and its utilization for random bit generation,” *Opt. Lett.*, vol. 36, no. 23, pp. 4632–4, 2011.
- [177] N. Oliver, M. C. Soriano, D. W. Sukow, and I. Fischer, “Fast Random Bit Generation Using a Chaotic Laser: Approaching the Information Theoretic Limit,” *IEEE J. Quantum Electron.*, vol. 49, no. 11, pp. 910–918, Nov. 2013.
- [178] Y. C. Chung and Y. H. Lee, “Spectral characteristics of vertical-cavity surface-emitting lasers with external optical feedback,” *IEEE Photonics Technol. Lett.*, vol. 3, no. 7, pp. 597–599, Jul. 1991.
- [179] T. Heil, I. Fischer, W. Elsässer, and A. Gavrielides, “Dynamics of Semiconductor Lasers Subject to Delayed Optical Feedback: The Short Cavity Regime,” *Phys. Rev. Lett.*, vol. 87, no. 24, p. 243901, Nov. 2001.

- [180] S. Ji and Y. Hong, “Effect of Bias Current on Complexity and Time Delay Signature of Chaos in Semiconductor Laser With Time-Delayed Optical Feedback,” *IEEE J. Sel. Top. Quantum Electron.*, vol. 23, no. 6, pp. 1–6, Nov. 2017.
- [181] N. Li, W. Pan, S. Xiang, L. Yan, B. Luo, X. Zou, L. Zhang, and P. Mu, “Photonic Generation of Wideband Time-Delay- Signature-Eliminated Chaotic Signals Utilizing an Optically Injected Semiconductor Laser,” *IEEE J. Quantum Electron*, vol. 48, no. 10, pp. 1339–1345, 2012.
- [182] Y. Hong, “Experimental study of time-delay signature of chaos in mutually coupled vertical-cavity surface-emitting lasers subject to polarization optical injection,” *Opt. Express*, vol. 21, no. 15, p. 17894, Jul. 2013.
- [183] K. Kanno, A. Uchida, and M. Bunsen, “Complexity and bandwidth enhancement in unidirectionally coupled semiconductor lasers with time-delayed optical feedback,” *Phys. Rev. E*, vol. 93, no. 3, p. 032206, Mar. 2016.

## 8 Appendices

### 8.1 List of Publications

- [1] S. Ji, C. Xue, A. Valle, P. S. Spencer, H. Li, and Y. Hong, “Stabilization of Photonic Microwave Generation in Vertical-Cavity Surface-Emitting Lasers With Optical Injection and Feedback,” *J. Light. Technol.*, vol. 36, no. 19, pp. 4347–4353, Oct. 2018.
- [2] S. Ji, Y. Hong, P. S. Spencer, J. Benedikt, and I. Davies, “Broad tunable photonic microwave generation based on period-one dynamics of optical injection vertical-cavity surface-emitting lasers,” *Opt. Express*, vol. 25, no. 17, p. 19863, Aug. 2017.
- [3] S. Ji and Y. Hong, “Effect of Bias Current on Complexity and Time Delay Signature of Chaos in Semiconductor Laser With Time-Delayed Optical Feedback,” *IEEE J. Sel. Top. Quantum Electron.*, vol. 23, no. 6, pp. 1–6, Nov. 2017.
- [4] C. Xue, S. Ji, A. Wang, N. Jiang, K. Qiu, and Y. Hong, “Narrow-linewidth single-frequency photonic microwave generation in optically injected semiconductor lasers with filtered optical feedback,” *Opt. Lett.*, vol. 43, no. 17, p. 4184, Sep. 2018.

- [5] A. Valle, A. Quirce, S. Ji, and Y. Hong, "Polarization effects on Photonic Microwave Generation in VCSELs under Optical Injection," *IEEE Photonics Technol. Lett.*, vol. 1135, no. x, pp. 1–1, 2018.
  
- [6] Y. Hong and S. Ji, "Effect of digital acquisition on the complexity of chaos," *Opt. Lett.*, vol. 42, no. 13, p. 2507, Jul. 2017.
  
- [7] C. Xue, S. Ji, Y. Hong, N. Jiang, H. Li, and K. Qiu, "Numerical investigation of photonic microwave generation in an optically injected semiconductor laser subject to filtered optical feedback," *Opt. Express*, accepted and in publication progress, 2018.



## 8.2 Conference Attendant / Paper Accepted

- International Symposium on Physics and Applications of Laser Dynamics (IS-PALD) 2018 in Hong Kong.  
Paper Title: “Numerical investigation of the characteristics of photonic microwave in a semiconductor laser with optical injection and filtered optical feedback”
- Semiconductor and Integrated Opto-Electronics (SIOE), 2018 in Cardiff, UK.  
Paper Title: “Complexity and Time Delay Signature of Chaos in Semiconductor Laser subject to optical feedback” and “Period-One Oscillation for Photonic Microwave Signal Generation in Optical Injected VCSELs”
- International Conference on Transparent Optical Networks (ICTON), 2017 in Girona, Spain.  
Paper Title: “Optically injection vertical- cavity surface-emitting lasers for tunable photonic microwave generation”
- European Semiconductor Laser Workshop (ESLW), 2017 in Gothenburg, Sweden.  
Paper Title: “Narrow linewidth photonic microwave using optical injection vertical-cavity surface-emitting lasers”
- Conference on Lasers and Electro-Optics/Europe and the European Quantum Electronics (CLEO), 2017 in Munich, Germany.  
Paper Title: “Broad Tunable Photonic Microwave Source Using a Single-Mode VCSEL Subject to Parallel Optical Injection”